

Copyright
by
Travis Eric Swanson
2015

The Dissertation Committee for Travis Eric Swanson Certifies that this is the approved version of the following dissertation:

Bedform interaction and preservation

Committee:

David Mohrig, Supervisor

Gary Kocurek, Co-Supervisor

Joel Johnson

Wonsuck Kim

Paola Passalacqua

Bedform interaction and preservation

by

Travis Eric Swanson, B.S. Geo. Sci.; M.S. Geo. Sci.

Dissertation

Presented to the Faculty of the Graduate School of

The University of Texas at Austin

in Partial Fulfillment

of the Requirements

for the Degree of

Doctor of Philosophy

The University of Texas at Austin

August 2015

Dedication

This work is dedicated to Elizabeth Rinehart.

Acknowledgements

The sincerest and deepest thanks are owed to David Mohrig for boundless optimism, support and creative steering during and beyond the entirety of this work. Gary Kocurek gave much needed conceptual guidance and grounding to this work. Caroline Hern, Matthew Wolinsky, John Martin, Ru Smith and Douglas Leyden of Royal Dutch Shell Oil Company have immensely helped support the numerical modeling components of this dissertation. Jim Buttles was instrumental in preparing ideas for field and laboratory studies. Jeremy Venditti generously shared his data and ideas. Bayani Cardenas gave support through my MS, providing an academic launching pad to pursue doctoral studies. Field collection of data was greatly assisted by many hands, including: Ben Cardenas, David Brown, Wayne Wagner, Mauricio Perillo, John Shaw, and Yao You. Processing of LiDAR surveys of White Sands National Monument was performed by Virginia Smith and Elizabeth Rinehart. This work was continuously supported by my fiancée Elizabeth Rinehart and parents Eric and Nancy Swanson. I have kindly been supported by my sister and brother-in-law Jenny and Robert Nathanson. The thoughtfulness of my future father and mother-in-law Terry and Olga Copeland has continually aided me. I thank office mates and all research group members past, present and future for acting as a very necessary filter and sounding board for all things scientific.

Bedform interaction and preservation

Travis Eric Swanson, Ph.D.

The University of Texas at Austin, 2015

Supervisor: David Mohrig

Co-Supervisor: Gary Kocurek

The shape and motion of bedforms are envisioned to arise as a consequence of a hierarchical cascade of interactions that occur within a bedform field. Interactions within the field are driven by conditions external to the bedform field, called boundary conditions. One such boundary condition is transport regime, the annual cycle of sediment transporting winds that drive uneven movement and deformation of bedforms. Paradoxically, uneven bedform movement results in geometric organization, as bedform crests align to wind regime. High resolution mapping of bedform crest movement reveals stochastic crest motion that acts to maintain the geometric organization of the bedform field. Stochastic motion of bedforms is driven by the interaction of bedform topography with sediment transporting flows. One such interaction occurs when oblique bedform crests create a wake containing trailing helical vortices. Each trailing helical vortex may preferentially route sediment to or away from a downstream bedform. This routing causes deformation or ablation of the downstream bedform. Either way, a section of the downstream bedform may deform to an oblique orientation. The oblique section may also trail a helical wake and further propagate stochastic bedform motion downstream. Bedform field boundary conditions provide an external influence on stochastic bedform motion. A numerical model of dynamic bedform topography is fueled by four sets of

boundary conditions: a unimodal and bimodal wind regime each investigated with and without the restriction of a linear bedform source area. The chosen boundary conditions are demonstrated to influence the shape and stochastic motion of bedforms within the field the rate at which the bedforms grow and mature. Fields of bedforms, driven by boundary conditions may leave a stratigraphic record of their stochastic motion. Given sufficient time, boundary conditions are transient. A numerical experiment is performed to investigate the preservation of signals from both stochastic dune motion and a transient boundary condition, the strengthening and weakening of sediment transport with time. The numerical experiment demonstrates that stochastic dune motion and transient boundary conditions influence the preservation of bedform topography in the resulting stratigraphic record.

Table of Contents

List of Tables	xi
List of Figures	xii
Chapter 1: Introduction	15
Chapter 2: Aeolian dune sediment flux variability over an annual cycle of wind.....	21
2.1 Introduction.....	21
2.1.1 Background: Kinematic modeling of dune crest motion	22
2.1.2 Field location: White Sands NM, N.M. USA	25
2.2 Methods.....	26
2.2.1 Kinematic modeling of dune crest motion.....	26
2.2.2 Algorithm for computing sediment flux vectors.....	26
2.2.3 Kinematic modeling of crest motion.....	27
2.2.4 Estimating crest motion from repeat LiDAR surveys.....	28
2.3 Results.....	30
2.3.1 Kinematic model results	30
2.3.2 LiDAR based results:.....	32
2.3.2.1 Brink height and lee surface dip direction	32
2.3.2.2 Motion and sediment flux calculated by brink nodes	33
2.3.2.3 Reaching average values.....	38
2.3.3 Error	39
2.4 Discussion	39
2.5 Conclusions.....	41
2.6 Acknowledgements.....	42
Chapter 3: Bedform spurs: a symptom of a trailing helical vortex wake	43
3.1 Introduction:.....	43
3.2 Methods:	47
3.3 Results:.....	51
3.3.1 The geometric configuration of spur-bearing bedforms	51

3.3.2 Observations of spur-bearing bedform behavior	53
3.3.2.1 Connecting trailing helical vortices to spurs.....	53
3.3.2.2 Connecting trailing vortices to bedform interactions.....	54
3.3.2.3 Growth of spur-bearing bedforms in a flume experiment	57
3.4. Discussion:	61
3.4.1 A conceptual model for the creation of bedform spurs:	62
3.4.2 The geometric configuration of trailing vortices:	65
3.4.3 Downstream crest deformation	68
3.4.4 The trailing helical vortex motor	71
3.5 Conclusions:.....	72
3.6 Acknowledgements:.....	74
Chapter 4: A surface model of aeolian dune topography	75
4.1 Introduction.....	75
4.2 Methods.....	76
4.2.1 An aeolian surface model.....	76
4.2.2 Grid and boundary conditions.....	81
4.2.3 Post-processing of aeolian surface model output.....	82
4.3 Application.....	83
4.3.1 Model input for applied cases	83
4.3.2 Model comparison to natural aeolian dune topography.....	86
4.3.3 Unimodal transport regime with fully periodic boundaries.....	89
4.3.4 Bimodal transport regime with fully periodic boundaries	92
4.3.5 Unimodal transport from a line source area.....	95
4.3.6 Bimodal transport from a line source area.....	98
4.3.7 Relative geomorphic aging	101
4.4 Conclusions.....	103
4.5 Acknowledgements:.....	104
Chapter 5: Self-organization, autogenic and allogenic signal preservation in aeolian cross-stratification.....	105
5.1 Introduction:.....	105

5.2 Methods:	106
5.2.1 Original 1D bedform surface model	106
5.2.2 1D bedform stratification model	107
5.2.3 Grid and boundary conditions	112
5.2.4 Post processing of model output: synthetic stratigraphy	112
5.3 Results:	113
5.3.1 Creation of synthetic cross-sections	113
5.3.2 Preservation potential	124
5.3.3 Morphometric analysis	125
5.3.4 Cumulative strata age distributions	130
5.4 Discussion	132
5.5 Conclusions	134
5.6 Acknowledgements	136
Chapter 6: Conclusions	137
Appendix A: Exponential-saturation and two term exponential fits	142
Appendix B: Supplemental material	143
Bibliography	144
Vita	149

List of Tables

Table 4.1:	Model parameters for all runs.....	85
Table 4.2:	Comparison of geomorphic “aging”.....	103
Table 5.1:	Values of parameters used in all simulations.....	111
Table 4.3:	Fit parameters.....	142

List of Figures

Figure 1.1: Conceptual diagram of a bedform system.	17
Figure 2.1: Kinematic models of bedform movement.....	23
Figure 2.2: Maps of field area.	25
Figure 2.3: Sketch of brink displacement calculation.	29
Figure 2.4: Wind rose and sediment transport vectors.	31
Figure 2.5: Kinematic model results.	32
Figure 2.6: Brink height and lee surface dip direction histograms.....	33
Figure 2.7: Map of dune topography and brink displacement.....	34
Figure 2.8: DEM-based sediment flux and brink movement.	36
Figure 2.9: Comparison of kinematic modeling with DEM derived estimates. ...	37
Figure 2.10: DEM derived dune observations as a function of window size.	38
Figure 3.1: Conceptual model of bedform spur.....	45
Figure 3.2: Image North Loup bedforms and crest traces	46
Figure 3.3: Field area.....	50
Figure 3.4: Measurements of spur bearing bedform topography	51
Figure 3.5: Spur width as a function of bedform height.....	52
Figure 3.6: Probability plot of the angle between spur and parent dune crest. ...	53
Figure 3.7: An oblique image of a spur extending from a ripple crest.....	54
Figure 3.8: Time lapse defect bedform interaction.	56
Figure 3.9: The transition between 2D and 3D bedforms	58
Figure 3.10: Deformation of 3D bedforms.....	60
Figure 3.11: A conceptual model of fluid circulation around a circular cylinder .	62
Figure 3.12: Trailing vortex formation.	64

Figure 3.13: Geometric model of trailing vortices.....	68
Figure 3.14: Sediment routing by trailing vortices.....	70
Figure 4.1: Diagram of model domain.....	81
Figure 4.2: Transport direction ECDFs.....	85
Figure 4.3: DEMS of modeled and natural aeolian bedforms.....	87
Figure 4.4: Roughness of modeled and natural dune topography.....	89
Figure 4.5: Unimodal aeolian bedform topography.....	91
Figure 4.6: Unimodal bedform metrics as a function of time.....	92
Figure 4.7: Bimodal aeolian bedform topography.....	94
Figure 4.8: Bimodal bedform metrics as a function of time.....	95
Figure 4.9: Unimodal aeolian bedform topography.....	97
Figure 4.10: Unimodal bedform metrics as a function of space.....	98
Figure 4.11: Bimodal aeolian bedform topography.....	100
Figure 4.12: Bimodal bedform metrics as a function of space.....	101
Figure 5.1: Conceptual hypothetical model scenario.....	107
Figure 5.2: Allogenic signals imposed on bedform topography.....	111
Figure 5.3: Model grid, element and boundary condition construction.....	112
Figure 5.4: Transient bedform shape.....	114
Figure 5.5: Self-organization of bedforms.....	115
Figure 5.6: Deep scour and group formation.....	117
Figure 5.7: “group”-sourced cosets.....	119
Figure 5.8: Stratigraphic section from simulation 1.....	120
Figure 5.9: Stratigraphic section from simulation 2.....	120
Figure 5.10: Stratigraphic section from simulation 3.....	121
Figure 5.11: Stratigraphic section from simulation 4.....	121

Figure 5.12: Stratigraphic section from simulation 5.....	122
Figure 5.13: Stratigraphic section from simulation 6.....	123
Figure 5.14: Comparison of bedform and surface count.....	125
Figure 5.15: Moments of bedform topography through time.....	127
Figure 5.16: Stochastic models of bedform preservation.....	130
Figure 5.17: Normalized age distribution of preserved strata.....	131

Chapter 1: Introduction

Bedforms are easily recognizable topographic features that grow, deform, move and decay on a bed of movable materials (Jackson et al., 2005). Bedforms arise from the fluid driven motion of bed materials. Processes that drive the motion and deformation of bedform surfaces also encode the shape and motion of bedforms into cross stratified deposits in aeolian and fluvial environments (Sorby, 1859). Interpreting the architecture of aeolian and fluvial cross stratification to reconstruct ancient environments requires knowledge of these processes that drive changes in bedform shape and motion. Although changes in bedform shape and motion are accomplished by the motion of individual particles, bedform shape and motion at the landform scale is often considered to be a consequence of self-organization, the emergent behavior of a complex system. Self-organization of bedforms is attributed to a hierarchical cascade of interactions that occur in the bedform system (Kocurek et al., 2010; Werner, 1995; Werner, 2003). An interaction is the particular way that fluid, granules, or bedforms affect each other within the bedform system. Interactions are most clearly demonstrated as a way that bedforms affect each other at the landform scale where bedforms collide, split, and merge, in regular, reproducible geometric configurations (Kocurek et al., 2010). While the motion of bedform crest terminations has been demonstrated to propagate interaction at the landform scale (Werner and Kocurek, 1997, 1999), quantitative, or even mechanistic descriptions of interactions in bedform systems are infrequently supplied.

Bedform systems are subject to boundary conditions (Eastwood et al., 2011; Ewing and Kocurek, 2010; Kocurek et al., 2010). In a departure from the formal mathematical definition, boundary conditions in the context of bedform systems are envisioned as any external condition

imposed on the bedform system that acts to initiate or constrain interaction. Therefore, boundary conditions are thought to both drive interactions and enforce limitations on the size, shape and motion of bedforms within the system. An intuitive example of a boundary condition limiting the behavior of bedforms would be the depth of flow in which a field fluvial bedforms can form. The influences of boundary conditions on bedforms within the field are often demonstrated with conceptual statements (Ewing and Kocurek, 2010; Kocurek et al., 2010) shown through empirical relationships (Ewing and Kocurek, 2010) and dynamic models of bedform topography (Eastwood et al., 2011; Ewing and Kocurek, 2010). Gaps in knowledge exist within the hierarchical cascade of interactions fueled by boundary conditions of bedform systems (Figs. 1.1a,b). However, a far larger gap is the connection that exists between the boundary conditions of a bedform system, its internal interactions, and the resulting rock record (Fig. 1.1). The aim of this dissertation is to detail four projects, targeted works that elucidate interactions within bedform systems (Fig. 1.1b), the influence of bedform system boundary conditions on bedform topography (Fig. 1.1a), and the propagation of signals from transient bedform system boundary conditions into sedimentary deposits created by dynamic bedform topography (Fig. 1.1c).

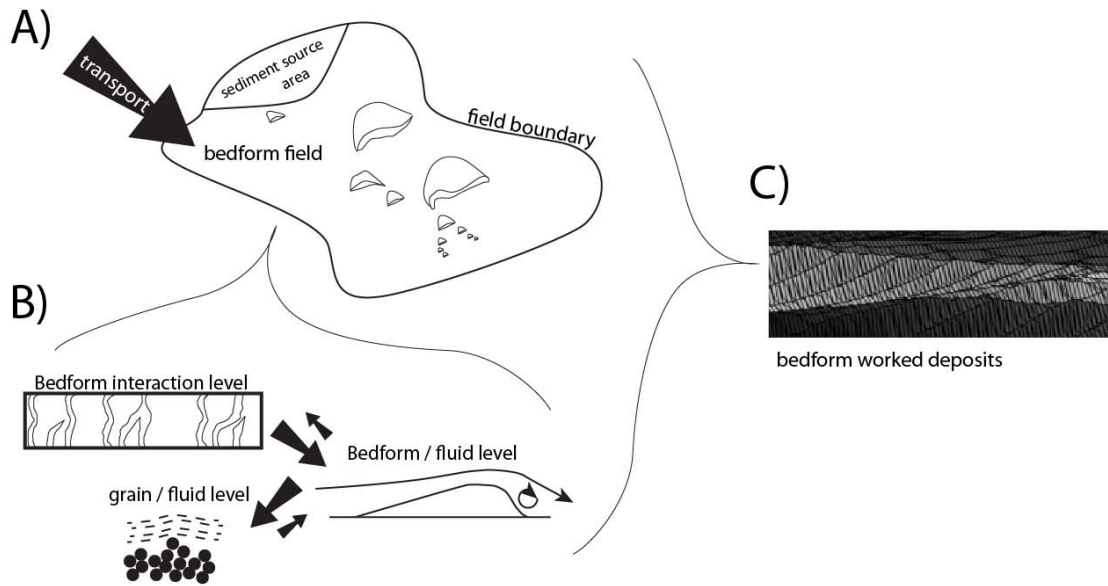


Figure 1.1: Conceptual diagram of a bedform system. A) Diagram of a hypothetical bedform system subjected to boundary conditions. B) Conceptual model of interactions within the bedform system modified from Kocurek et al. (2010) and Werner (2003). C) Rock record of dynamic bedform topography driven by boundary conditions (A) and interactions (B)

During a single sediment transporting flow aeolian bedforms are found to move unevenly (Eastwood et al., 2012; Rubin and Hunter, 1985). Yet, when viewed as a field, bedform crests are found to align as perpendicular as possible to all sediment transporting directions (Rubin and Hunter, 1987; Rubin and Ikeda, 1990). This behavior presents an apparent paradoxical connection between a boundary condition (Fig. 1A), transport regime, uneven bedform motion a driver for bedform interaction (Fig. 1B), and the large scale geometric organization of bedform crests within the field. Despite the uneven motion of bedforms over single sediment transporting events and during bedform interactions, at a larger time and spatial scale, bedforms align to become as perpendicular as possible to the net resultant transport direction (Ping et al., 2014; Rubin and Hunter, 1987; Rubin and Ikeda, 1990). Assumed but never demonstrated is how unequal motions of bedform crest maintain dune crest organization as a trend line. Chapter 2 documents how non-uniform motion of aeolian dunes over an annual cycle of sediment

transporting wind events is demonstrated to be symmetrically distributed about a compass direction. Although portions of dunes may move unevenly, when calculated for a sufficiently large area dune motion and motion induced sediment flux become very nearly symmetrically distributed. Dune crest motion in direction away from the line of symmetry is directionally balanced, drives geometric organization of dune crests.

Interaction between fluid and bedform topography is a fundamental driver of bedform motion, deformation and bedform interactions. Chapter 3 thoroughly documents the discovery of a new interaction between fluid motion and dynamic bed topography. Bedform spurs (Allen, 1968) also known as bedform fins (Guy et al., 1966) or lee projections (Cooper, 1958) are linear bodies of sediment that extend from the lee surface of bedforms. Previously attributed to near bed helical vortices (Allen, 1977), the presence of bedform spurs is found to be caused by vortices that trail from the lee surface of the parent bedform, a newly discovered interaction between fluid motion and dynamic bed topography. The interaction manifests as a bedform wake composed of helical vortices that trail from segments of bedform crests oriented obliquely to the fluid flow direction. The spacing between sequential trailing helical vortex filaments is found to scale with the vertical distance between the crest and lee trough of the parent bedform crest and the incidence angle to upstream fluid flow. This relationship is well described by a cross-stream Strouhal number (Levi, 1983; Snarski, 2004; Strouhal, 1878; Thomson and Morrison, 1971); which predicts the spacing of helical vortex filaments that trail from an obliquely oriented obstruction to flow. A conceptual model for the occurrence and spacing of bedform spurs is developed directly from the criteria for helical vortices to trail from a bedform. Once initiated, a trailing helical vortex rapidly entrains sediment and augments sediment transport. Augmented sediment transport due to a trailing helical flow is an interaction between topography and fluid

motion (Fig. 1.1b). The augmented sediment flux due to the interaction is sufficient to scour through the body of a downstream bedform, directly causing an interaction at the bedform interaction level (Fig. 1.1b). Augmented sediment delivery downstream of the parent bedform may deform downstream bedforms, perhaps forming additional oblique crests, which may trail additional helical vortices. In this manner, trailing helical vortices and their focused delivery can self-propagate through a field of bedforms. This feedback is promoted as an interaction to help explain why there is a distinction between straight crested (2D) and sinuously crested (3D) bedforms (Southard and Boguchwal, 1990; Venditti et al., 2005).

A surface model of dynamic bedform topography allows for bedform shape and motion to be approximated for durations of time impossible to realize through natural observation. Although other forward models of bedform topography exist, many utilize a cellular automata approach (Eastwood et al., 2011; Werner, 1995). Cellular methods produce astoundingly robust bedform shapes and behavior using simple, plausible rules for the motion of quantized parcels of sediment. However, because of this abstraction, cellular models are difficult to relate to natural bedform systems. As an tractable alternative to cellular methods, a process-based continuum expression of dynamic bedform topography is adapted to model aeolian bedform systems (Jerolmack and Mohrig, 2005). The bedform modeling framework casts bedform growth as a feedback between topography, shear stress and sediment flux (Jerolmack and Mohrig, 2005). Originally crafted for the study of subaqueous bedforms (Jerolmack and Mohrig, 2005), a two dimensional surface evolution equation is adapted to capture multidirectional sediment transport, a chief boundary condition of aeolian bedform systems. The newly adapted continuum forward model of aeolian bedform topography is explored using four sets of boundary conditions: a unimodal transport regime, a bimodal transport regime, a unimodal transport regime growing

bedforms from a line sediment source and a bimodal transport regime growing bedforms from a line sediment source. For the first time, change in dune shape with distance from a sediment source boundary is directly related to the time-equivalent for bedforms growing without the influence of a sediment source boundary. The model is promoted as a framework for further observation and quantification of bedform interactions.

Over long time scales, bedform field boundary conditions are transient features. One such example of a transient boundary condition is periodic fluctuations in sediment transport due to the relative strengthening or weakening of an annual wind. A numerical experiment is performed in chapter 5 to investigate signal propagation from a bedform system boundary condition into numerically created bedform stratigraphy. The aeolian bedform surface equation presented in chapter 4 is reduced to solve for 1D dynamic bedform topography. The 1D bedform surface equation is modified to accept two allogenic drivers used in separate model simulations. This hypothetical modeling scenario is thought to conceptually represent long term climatic variation of a dry intra-erg aeolian bedform system. The resulting time steps of 1D topography are used to create 2D sections of synthetic aeolian stratigraphy. Signals due to externally sourced variation in sediment transport magnitude is found to comingle with autogenic signals within the architecture of the stratigraphic sections. A pre-existing modification (Bridge and Best, 1997) to a stochastic theory of bedform topography and the select preservation of bedform topography in stratigraphy (Paola and Borgman, 1991) is re-interpreted to accommodate unexpected preservation of bedform topography due to variability in bedform topography sourced from autogenic or allogenic signals.

Chapter 2: Aeolian dune sediment flux variability over an annual cycle of wind

2.1 INTRODUCTION

Aeolian dune cross stratification is a record of directionally varying wind driving dune movement. Along crest, dunes move unevenly with every sediment transporting wind event, yet aeolian dune crest lines are geometrically organized into a coherent trend line by an annual cycle of wind. Understanding variation in dune movement within such a cycle of wind is directly applicable to constraining the uncertainty when interpreting past dune morphology and movement from the architecture of aeolian deposits. This work elucidates how uneven movement of dune crests offset over an annual cycle of wind to maintain dune crest organization as a well-defined trend line.

In practice, cross-strata sets with limited exposure, such as core and outcrop are used to infer the motion and morphology of ancient dunes. The inferred dune morphology and kinematics are often used to interpret past climate associated with the ancient aeolian system. Such interpretation is supported by several models that provide mechanistic links among annual cycles of wind, the mean alignment of dune crest lines, and dune motion. Through experimentation, Rubin and Hunter (1987) developed a predictive model for crest trend alignment to the net resultant of an annual cycle of wind. Their experimental results illustrate that bedform crests, measured as a trend line, become as orthogonal as possible to the net resultant of all sediment transporting wind directions. In a landscape scale experiment, Ping et al. (2014) observed oblique dunes grow from a flattened bed and realign to each seasonal wind direction until a statistically steady motion and orientation to the overall wind regime was

observed, empirically confirming the experimental result of Rubin and Hunter (1987). Crest motion due to a single wind event (Eastwood et al., 2012; Rubin and Hunter, 1985) and crest motion due to sediment routing over an individual barchan dune (Howard et al., 1978) is shown to be highly variable and sensitive to the shape of the dune crest. A gap in knowledge exists because models of bedform alignment and motion in response to annual cycles of wind explicitly assume, but do not demonstrate, that uneven crest motion from individual wind events offset to actively maintain crest organization as a well-defined trend line.

In this study, successive airborne LiDAR surveys of White Sands dune field, south-central New Mexico, provide high resolution observations of spatially and temporally varying dune movement that can in turn be directly related to field-averaged values of dune alignment and motion. Local dune behavior is connected to field-scale behavior using a kinematic model of dune crest motion that predicts the average motion of dune crests. The model demonstrates that although dunes move unevenly and deform, over an annual cycle of wind a geometric organization of dune crest lines is maintained because variations in local crest-line orientation, sediment flux and dune motion, measured over a sufficiently large portion of a dune field, are symmetrically distributed about a mean dip direction. Topographic data from the LiDAR surveys at Whites Sands are used to directly determine how large an area of dune field must be explored to produce a representative picture of the entire field. While this result is specific to the White Sands dune field, it provides a methodology and point for comparison with other dune fields.

2.1.1 Background: Kinematic modeling of dune crest motion

The bedform crest motion and alignment model for directionally varying flow, termed gross bedform-normal transport (GBN) collapses the entire annual variation in sediment-

transport regime into a simplified description, two sediment flux vectors. Their simple description is entirely composed of a primary, or dominant (\vec{d}) sediment transport vector and a secondary, or subordinate (\vec{s}) sediment transport vector (Rubin, 1987; Rubin and Ikeda, 1990). Rubin (1987) and Rubin and Ikeda (1990) systematically varied the relative magnitude and direction of \vec{d} and \vec{s} in sets of experiments and found that bedform crests align so that the value of crest trend-normal sediment transport is maximized (Fig. 2.2). This simple model has been found to successfully predict the bedform field crest trend and mean transport direction in cellular automata dune pattern models having diverse annual distributions of sand-transport directions (Kocurek and Ewing, 2005; Werner, 1995) and has been widely applied to connect observed dune crest trend alignments to annual wind roses (Lancaster et al., 2002; Ping et al., 2014; Sweet et al., 1988).

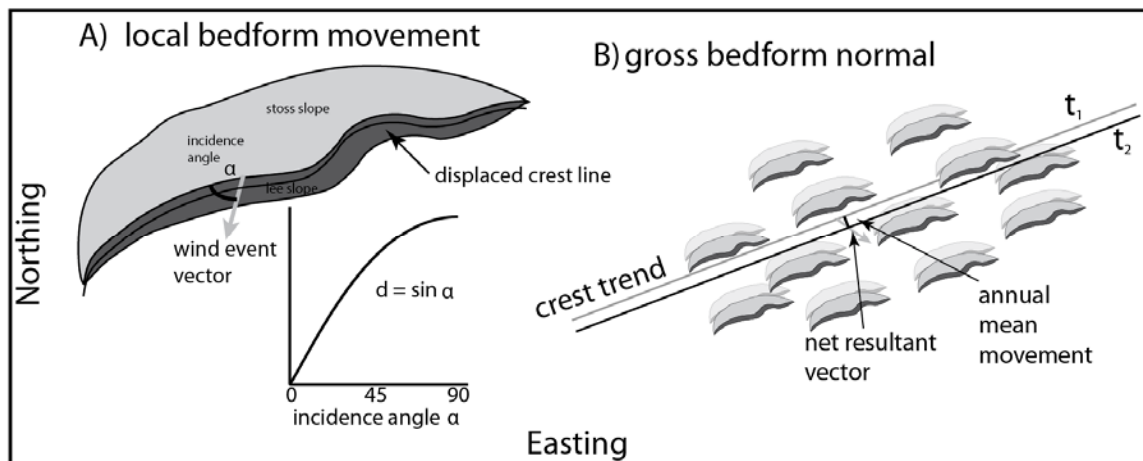


Figure 2.1: Kinematic models of bedform movement. Conceptual model showing local bedform movement (LBM) and gross bedform movement normal to the crest trend line (GBN).

Local bedform motion (LBM) is a kinematic model that describes non-uniform motion along a dune crest due to a single sediment transporting wind event. LBM was initially proposed by Rubin and Hunter (1985) and compared to field measurements by Eastwood et al. (2012). In this model, the lee slope deposit thickness due to a single wind event varies directly with the incidence angle α formed between the local orientation of dune crest line and a unit vector that describes the wind event direction (Fig. 2.1a). Variation in the along-crest bedform movement is described by $d(\alpha) = D \sin \alpha$, where D is the maximum displacement associated with portions of lee slopes most perpendicular to the wind direction ($\alpha = 90^\circ$). Portions of lee slopes most parallel to the wind direction ($\alpha = 0^\circ$) displace the least (“displaced crest line” Fig 1a). As presented, LBM does not explain bedform crest orientation to an annual wind rose or how crest motion varies with dune height or any other control on dune motion.

The experiments performed by Rubin and Ikeda (1990) produced bedforms with curved crests and non-uniform height (see their figures 7 through 9). Bedforms with varying lee surface dip direction are predicted to displace unevenly by LBM, even for a unidirectional flow. Despite predicted uneven crest movement, the overall trend line of the sinuous crest lines is predicted by the GBN model. How can sinuous bedforms achieve alignment at the time and spatial scale of a transport regime when LBM suggests that each unidirectional wind event moves portions of curved crests unevenly? To understand how incremental, uneven crest movements accrue over an annual cycle of wind produce a GBN-type organization, a kinematic model of dune crest motion is driven using an annual cycle of wind events for White Sands gypsum dune field, New Mexico. These model results are then compared to DEMs (digital elevation models) of the dune field that resolve bedform movement for variable dune height and lee surface dip direction.

2.1.2 Field location: White Sands NM, N.M. USA

White Sands, NM, is a gypsum sand dune field that emerges from a playa source area (Fig. 2.2b) (Kocurek et al., 2007). Dunes rapidly grow from the source area and coalesce into crescentic dunes that populate the center of the dune field. The crescentic field transitions to and is flanked by parabolic dunes correlated with encroaching vegetation (Fig. 2.2b). This study focuses on the motion of crescentic dunes within a morphologically homogenous $1.96 \text{ [km}^2\text{]}$ portion of the core of the field (Fig. 2.2).

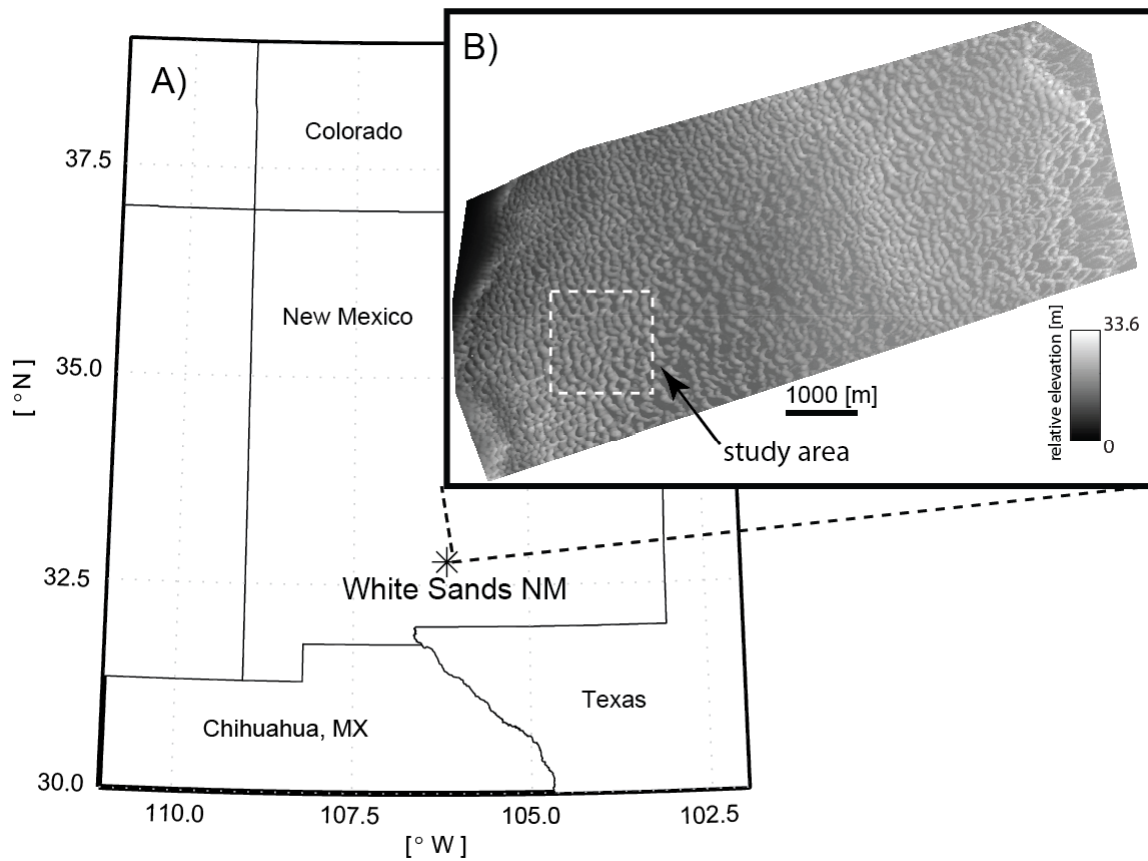


Figure 2.2: Maps of field area. A) Map showing the location of White Sands National Monument, New Mexico, USA. B) Full LiDAR based DEM of White sands showing the crescentic dune core transitioning to parabolic dunes to the East. The study area is outlined in a white dashed box. Gray scale is relative elevation.

2.2 METHODS

2.2.1 Kinematic modeling of dune crest motion

The underpinning of GBN and LBM modeling is that the angle separating bedform crest orientation from the sediment transport direction defines the partitioning of sediment flux into a component that is deposited, driving bedform crest movement, and a component that bypasses the lee face. Interestingly, LBM and GBN partition sediment flux by the same geometric argument. The component normal to the crest is deposited in the case of LBM. In the case of GBN the component normal to the crest trend (GBN) is deposited. To model GBN-type motion over an annual cycle of wind, we simply calculate the gross sediment flux accrued in the dip directions representative of White Sands, including the dip direction corresponding to the overall crest-line trend. This calculation yields the anticipated motion of dune crests of all orientations. This also gives an estimate of LBM-type crest motion, assuming that lee surfaces do not change dip direction significantly over the annual cycle of wind.

2.2.2 Algorithm for computing sediment flux vectors

The displacement of hypothetical “crests” is determined using dune height, dip direction and a sediment flux vector for time intervals of wind that exceed a threshold-of-motion.

Conceptually, a wind event sediment flux vector, \vec{l} (Wind event vector, Fig. 2.1a) represents the sediment flux driving the motion of a bedform due to stoss slope erosion and lee slope deposition. Each wind vector is taken from an annual cycle of wind events reported by Pedersen et al. (2015) from nearby Holloman Air Force Base. This record yields similar velocities and directions to those measured within White Sands dune field (Eastwood et al., 2012). A threshold-shear velocity based calculation is used to estimate sediment flux for each wind event.

Shear velocity, $u_* [ms^{-1}]$, is estimated using a logarithmic velocity profile of wind $u_* = \frac{\kappa |\vec{u}_{wind}|}{\ln(Z/Z_0)}$. Where κ is Von Karman's constant 0.401 [-], $Z = 10[m]$ is the height of wind velocity observation, \vec{u}_{wind} is the wind vector at height Z , $Z_0 \approx 0.01 [m]$ is the appropriate roughness height (Eastwood et al., 2012). Volumetric sediment flux $q_s [m^2s^{-1}]$, corresponding to u_* is estimated by $q_s \approx 0.8 \frac{\rho_f}{g(\rho_s - \rho_f)} u_*^3$, where $\rho_f = 1.2 [kgm^{-3}]$, is the density of the transporting fluid $\rho_s = 2300 [kgm^{-3}]$ is the particle density, $g = 9.81[ms^{-2}]$ is a gravitational constant (Bagnold, 1941). Sediment flux vectors have the same direction as the corresponding wind event ($\vec{l} = q_s \hat{u}_{wind}$). Any wind velocities below a threshold-of-motion ($8.3 ms^{-1}$) representative of gypsum sand grains within the White Sands dune pattern are discarded (Eastwood et al., 2012; Pedersen et al., 2015).

2.2.3 Kinematic modeling of crest motion

The sediment flux vectors are used to estimate the motion of hypothetical dune crests for a range in dune height and lee surface dip direction corresponding to those in the White Sands dune field (Fig. 6). The movement of a dune crest oriented perpendicular to the sediment transport direction is estimated using a statement of sediment conservation $q_s = \frac{h}{2} c_{dune} \varepsilon$ (Bagnold, 1941), where $q_s [m^2s^{-1}]$ is volumetric sediment flux, $c_{dune} [ms^{-1}]$ is dune celerity or speed, $h [m]$ is dune height, and $\varepsilon [-]$ is volumetric sediment concentration (1 – porosity). Integration of $q_s = \frac{h}{2} c_{dune} \varepsilon$ over the time duration, $\Delta t [s]$, of the event and rearranging, yields the magnitude of bedform crest movement, $d = \frac{2q_s}{h\varepsilon} \Delta t [m]$. To estimate how dune crests with various dip directions are moved by particular sediment flux vectors, the kinematic model is

modified to account for incidence angle (Fig. 2.1), $d(\theta) = \frac{2q_s\Delta t}{h\varepsilon} \sin \theta$. The incremental “crest” movement is accrued through the time series of sediment-flux vectors, $\sum d_i \sin \theta_i$, and binned by compass direction. This calculation gives the GBN-type displacement distance for each hypothetical dune dip direction while accounting for the variation in dune height present in White Sands dune field and is summarized in Figure 2.5.

2.2.4 Estimating crest motion from repeat LiDAR surveys

Repeat LiDAR surveys yielded uniform 1 [m] (raster) DEMs capturing snapshots of dune topography at White Sands. Details on the LiDAR data collection methods are presented by Pedersen et al. (2015). The LiDAR derived DEMs were used to create aspect maps, slope maps and elevation change maps. Dune brinks, dramatic breaks in dune surface slope that mark the upwind extent of slip faces on lee slopes are strongly correlated to dune crests. Dune brinks are used in place of dune crests for the LiDAR portion of this study because they can be accurately and automatically detected in the airborne LiDAR derived DEMs using the Canny edge detection algorithm operating on a slope map of dune topography (Canny, 1986). The resulting elevation, position and dip direction found using dune brink locations are used to estimate brink motion, and sediment flux within White Sands.

Dune brink-based displacement were computed for the 1.96 km² morphologically homogenous portion of White Sands over a time interval of $\Delta t = 1.1$ [yr]. A brink detection and filtering algorithm detected 7218 brink nodes and their co-registered geometrically computed movement in the dip direction (Fig. 2.3). Elevation, Northing, Easting, and vectors oriented normal to the dune surface were stored in co-registered data arrays, such that values corresponding to automatically detected brinks are used to find corresponding spatial data.

Automatically detected edges in the surface slope map were logically filtered to remove false positives which included topographic edges created by superimposed dunes, ridges within interdune areas, lee toes or aprons. Any dune brink computed to have migrated more than the brink height was discarded. Additionally, nodes with surface slope $< 20^\circ$ or $> 35^\circ$ slope were discarded.

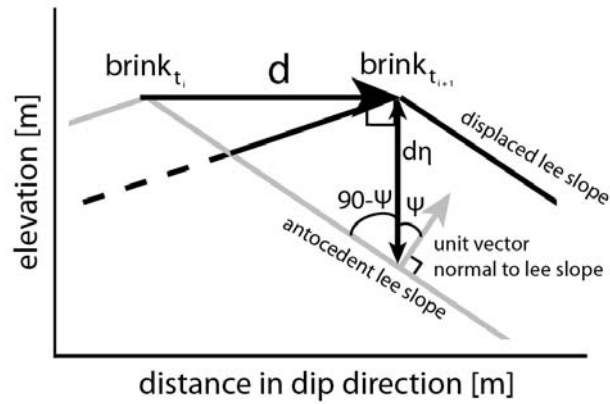


Figure 2.3: Sketch of brink displacement calculation. Diagram showing the geometric construction for calculating displacement length d from two time snapshots of dune topography imaged in LiDAR-derived DEMs.

The motion of dune brink nodes between LiDAR surveys was calculated by stepping backward in time (Fig. 2.3). Brink node movement in the dip direction was estimated by calculating how far antecedent lee slopes need to be translated to obtain their future horizontal brink position (Fig. 2.3). The geometric construction used the brink nodes at t_{i+1} (06-09-2008) to find ψ , the angle formed between the vertical axis and a unit vector normal to the antecedent (t_i , 06-09-2007) lee slope (Fig. 2.3). Using the antecedent lee slope to calculate dip direction and slope takes advantage of the smooth slip faces of dunes, which allows for a more accurate calculation of surface geometry. The elevation change $\Delta\eta = \eta_{t_{i+1}} - \eta_{t_i}$ is then used to find the horizontal distance $d = \Delta\eta \tan(90^\circ - \psi)$ required to translate the antecedent lee slope to

achieve the t_{i+1} brink elevation (Figure 2.3) for each brink node. Sediment flux due to brink movement is calculated as $q_s = \frac{h}{2} d\varepsilon [m^2 yr^{-1}]$ (Bagnold, 1941) using node brink height h (interdune elevation is set to zero), and an assumed sediment concentration $\varepsilon = 0.7 [-]$. This method allows brink movement in the dip direction and brink-movement based sediment flux to be estimated for brinks of various dip direction and height within White Sands.

2.3 RESULTS

2.3.1 Kinematic model results

Wind events observed at nearby Holloman Air Force Base (ID: KHMN) by a 10 [m] meteorological tower from 06-09-2007 to 07-06-2008 (a duration of 1.1 [yr]) are used to drive the kinematic dune crest model (Pedersen et al., 2015). The wind events recorded at Holloman Air Force Base are very similar to the wind events over the White Sands dune field (Eastwood et al., 2012; Pedersen et al., 2015). This annual cycle is described by a dominant wind blowing from the South West (Mode “d”, Fig. 4a), and a subordinate wind blowing from just South of East (mode “s”, Fig. 4a). Although the “s” mode are apparent in the wind rose, the transport regime is predominately unimodal (Jerolmack et al., 2012), as the subordinate winds are much weaker and less frequent than the prevailing Southwest wind. Winds that exceed threshold-of-motion are used to create sediment flux vectors shown in Figure 2.4b. Overall, the angular distribution of sediment flux vectors mimics the wind rose, but, due to the threshold of motion, few events force sediment movement in any direction but mode “d”. The greater strength of mode “d” is clearly demonstrated by the greater frequency and magnitude of sediment flux vectors in first quadrant of Figure 2.4b.

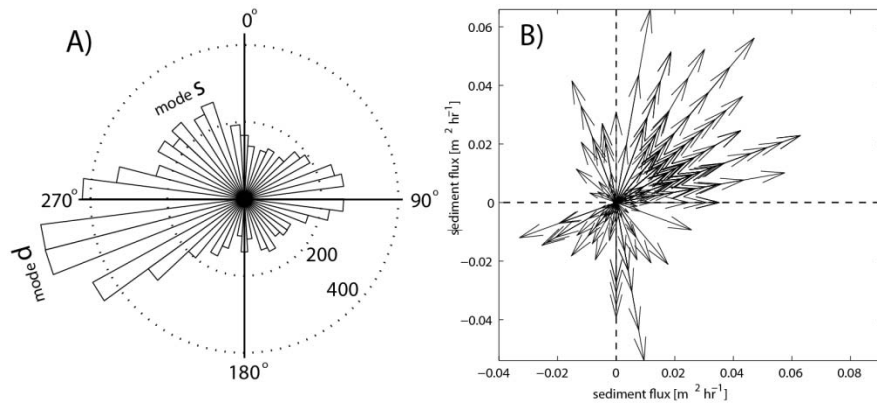


Figure 2.4: Wind rose and sediment transport vectors. A) Wind rose showing distinct “d” and “s” modes of wind direction sampled from 06-09-2007 to 07-06-2008 (a duration of 1.1 [yr]). B) Sediment flux vectors computed from wind events in A) that exceed a threshold-of-motion corresponding to the gypsum sand ($8.3 [ms^{-1}]$).

Kinematic modeling of dune crest motion predicts a simple sinusoidal variation of sediment flux with compass direction (Fig 2.5a). Sediment flux accumulated for each compass direction is then used to calculate dune motion. The maximum dune displacement length and sediment flux correspond to the vector net resultant (\vec{r}) direction of 055.45° (Fig. 2.5a, black square). Dune movement as a function of compass direction is shown in Figure 2.5b. The assumed brink height used to calculate dune brink movement can account for variation in dune movement for a given compass direction (Fig. 2.5b). The solid line in Figure 2.5b represents the anticipated dune movement for a brink of average height for various compass directions. The dashed lines in Figure 2.5b represent the motion of a dune brink that is one standard deviation greater or less than the mean brink height. Sediment flux, however, is constant for a single compass direction (Fig. 2.5a).

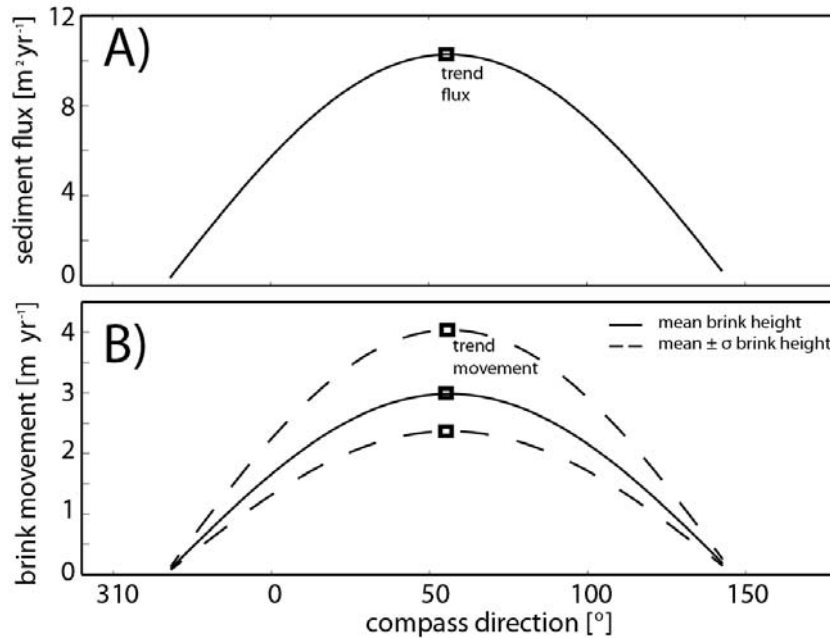


Figure 2.5: Kinematic model results. Sediment flux (A) and crest movement (B) predicted by kinematic modeling. The dashed lines represent crest movement for mean brink height \pm standard deviation. The solid curve represents predicted crest movement for mean brink height within the White Sands gypsum sand dune field.

2.3.2 LiDAR based results:

2.3.2.1 Brink height and lee surface dip direction

Brink nodes within the DEMs of the White Sands LiDAR surveys reveal brink height (Fig. 2.6a) and lee surface dip direction (Fig. 2.6b). Brink height and dip direction are used to geometrically estimate dune brink movement and sediment flux. The dip directions of lee slopes within the morphologically homogenous portion of White Sands (Fig. 2.6b) are approximately symmetrically distributed about a mean dip direction of 055° and standard deviation $\sigma = 39.8^\circ$ (Fig. 2.6b). The skewness of the population of dip directions is 0.1262 and the kurtosis is 2.74 where the expected values are 0 and 3 for data that are distributed normally (Fig. 2.6b). Brink

height within the same morphologically homogenous portion of White Sands (Fig. 2.6b) is well described by a two parameter gamma distribution (Fig. 2.6a), which has previously been used to describe bedform height (Leclair, 2002; Paola and Borgman, 1991). The fitted gamma distribution gives a shape parameter $\alpha = 14.4$ and scale parameter $\beta = 0.48$ which corresponds to a mean of $\frac{\alpha}{\beta} = 6.89m$ and a variance of $\frac{\alpha}{\beta^2} = 3.30 m$ in brink height (Fig. 2.6a).

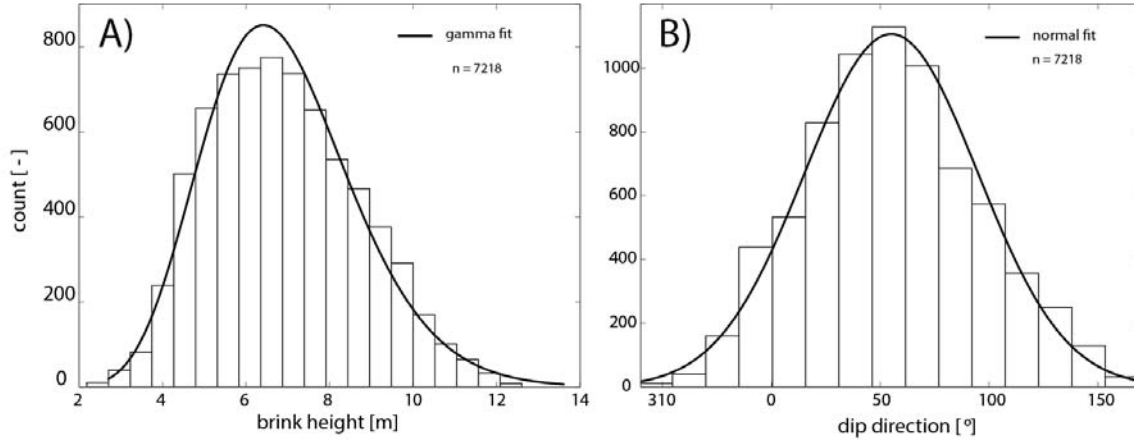


Figure 2.6: Brink height and lee surface dip direction histograms. A) Histogram of brink height found in the t_{i+1} DEM. Brink height is computed as the vertical distance between the brink and the bottom of the immediate lee slope. A fitted two parameter Gamma probability density function is shown by the solid line. B) Histogram of lee surface dip directions computed on the t_i DEM. A fitted normal probability density function is shown by the solid line. Both histograms have a population of 7218 brink “nodes”.

2.3.2.2 Motion and sediment flux calculated by brink nodes

Brink movement is color-mapped onto detected brink nodes in Figure 2.7. Portions of dune brink oriented roughly parallel to the field-scale crest-line trend (perpendicular to \vec{r} , Fig. 2.7) typically have the greatest movement and portions of lee surfaces that dip either North or South move substantially less (Fig. 2.7). Taller dunes shown by the brighter grayscale values

move the least as well, which is expected as $c_{dune} \propto \frac{1}{h}$.

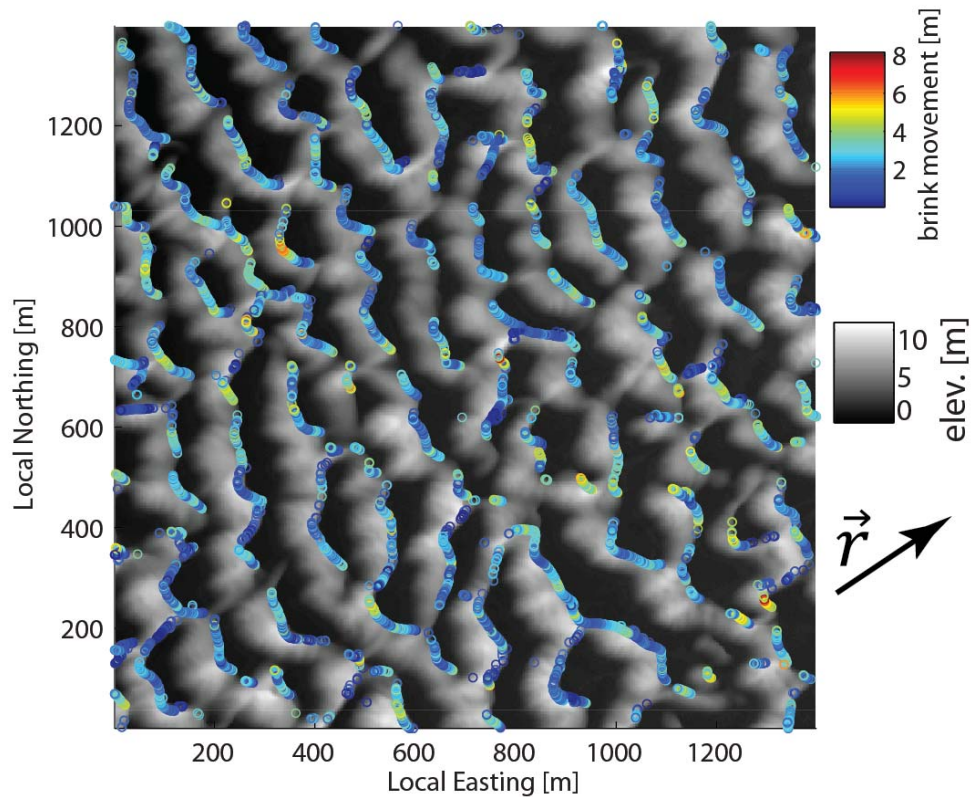


Figure 2.7: Map of dune topography and brink displacement. Gray scale LiDAR derived DEM of White Sands dune topography. Detected brink nodes are shown by the colored circles. Dune motion in the dip direction is shown by the color of the circles plotted on dune brinks. Conservative filtering leaves some empty intervals along dune brinks. This is acceptable because the filtering does not systemically remove any specific brink height or lee surface dip direction, only nodes that violate the method of estimating brink motion and sediment flux.

LiDAR estimated brink movement is plotted as a function of lee surface dip direction in Figure 2.8. The plotted values of brink movement follow the sinusoidal character of the kinematic model results (Figs. 2.5 and 2.8). However, significant variation in both estimated sediment flux and brink movement is readily apparent. Even so, large values of dune movement are generally in the direction normal to the field-scale crest-line trend (Fig. 2.8) and drop precipitously as brink dip direction approaches the crest trend direction (334° , 154°). Of particular interest are counterintuitive brink movements. Figure 2.7 and 2.8 show that portions of

dune crest oriented parallel to the crest trend may not move at all during an annual cycle of wind. Conversely, portions of dune crest with a dip direction nearly parallel with the crest trend may move distances approaching field maximum, although, unlikely. Such dune movements can never be predicted by the kinematic model.

Sediment flux computed from LiDAR-based brink displacement also exhibits substantial variability about each brink dip direction (compare Figs. 2.5b and 2.8b). Even so, calculated sediment flux is maximum near 55° , the direction normal to the field-scale crest-line trend, and decreases precipitously to the North and South. Calculating sediment flux from DEMs uses brink height, brink movement distance and lee slope dip direction. Figure 2.9a shows the bivariate histogram of brink height and lee surface dip direction. Intriguingly, the mean value of brink height corresponds to brink nodes that also have the mean lee surface dip direction (Fig. 2.9a). Similarly, brink nodes achieving mean magnitude of brink movement correspond to the mean lee surface dip direction (Fig. 2.9b). These data are combined to calculate sediment flux, which in turn, gives the result that the mean and median sediment flux occurs in the mean and median lee surface dip direction (Fig. 2.9c). The red curves superimposed on Figure 2.9B and 2.9c are the wind driven kinematic model results. The most frequently observed values for brink movement and estimated sediment flux correspond to same compass direction as the maximum sediment flux and dune crest movement computed using the kinematic model.

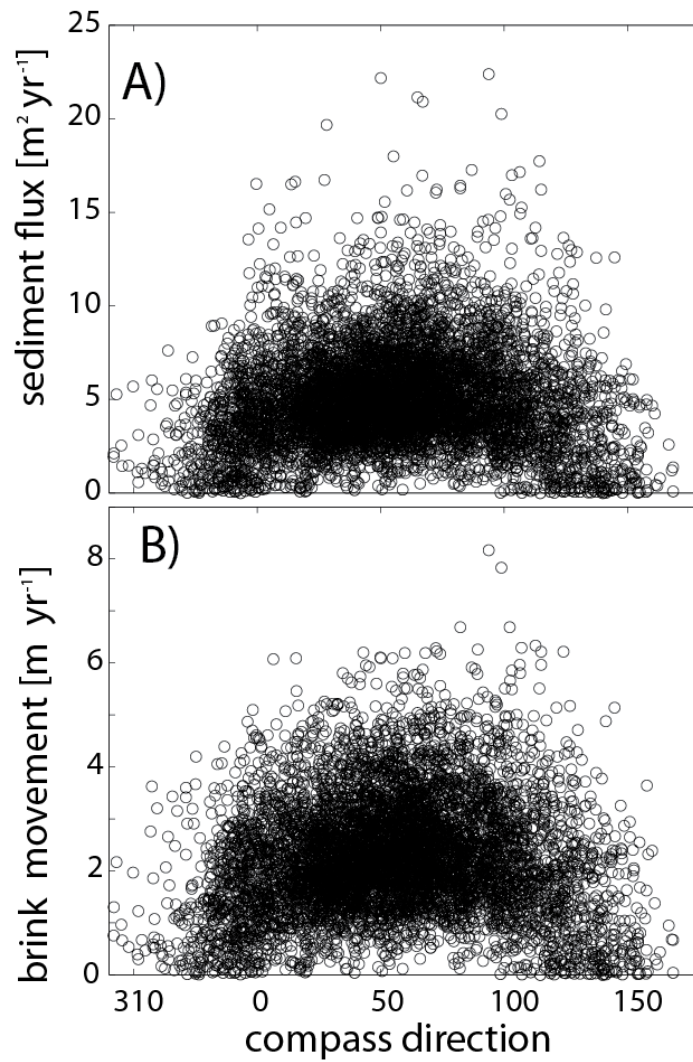


Figure 2.8: DEM-based sediment flux and brink movement. Scatter plots of A) sediment flux and B) dune brink movement as a function of lee surface dip direction. Each plotted open circle represents a single brink node.

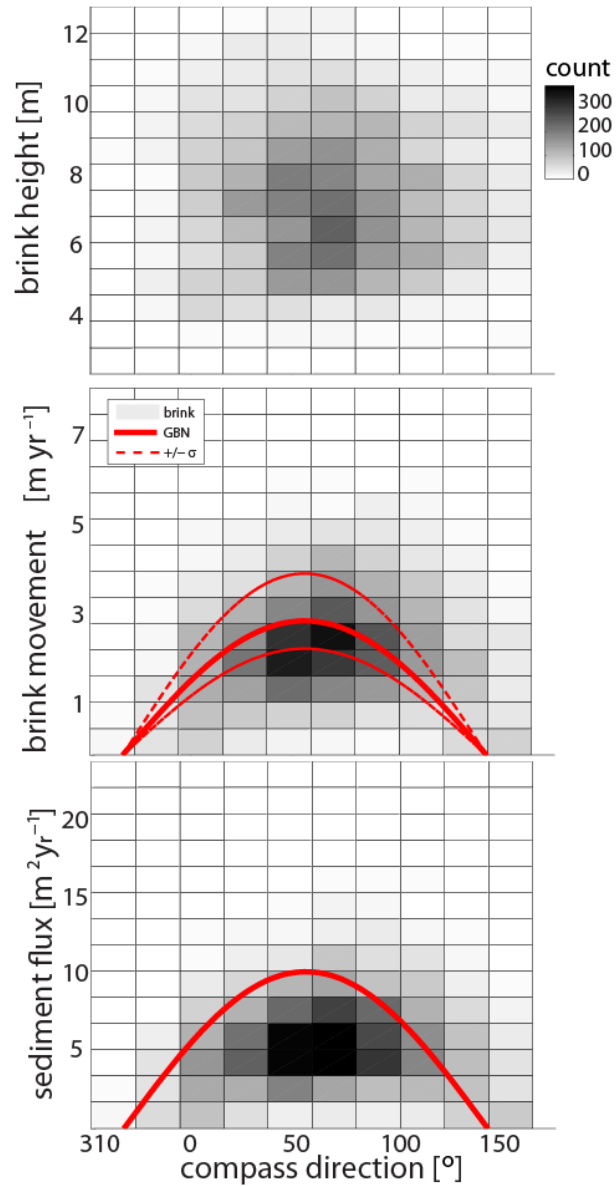


Figure 2.9: Comparison of kinematic modeling with DEM derived estimates. Bivariate histograms of A) brink height B) brink movement and C) sediment flux compared to lee surface dip direction. Brink movement from the wind driven kinematic model is overlain on B). Sediment flux from the kinematic model is overlain on C). The gray scale representation of histogram count is constant between subfigures.

2.3.2.3 Reaching average values

Ensuring that lee surface dip direction, brink height and brink movement are adequately sampled is fundamental to this or any study of bedform evolution. All three quantities are plotted as a function of increasing sample area in Figure 2.10 and simultaneously approach their average values as the sample window increases to a square with 632 [m] sides. This window length is just larger than the crest length of an average White Sands dune, approximately 550 [m] and corresponds to approximately six average White Sands dune wavelengths (measured crest to crest in the downwind direction) (Baitis et al., 2014; Baitis, 2011). As the sampling window grows beyond this size the calculated mean values of dip direction, brink height and brink movement become nearly invariant. The selected sampling area of 1.96 [km²] is sufficiently large to accurately characterize dune movement, dip direction and brink height used in this study.

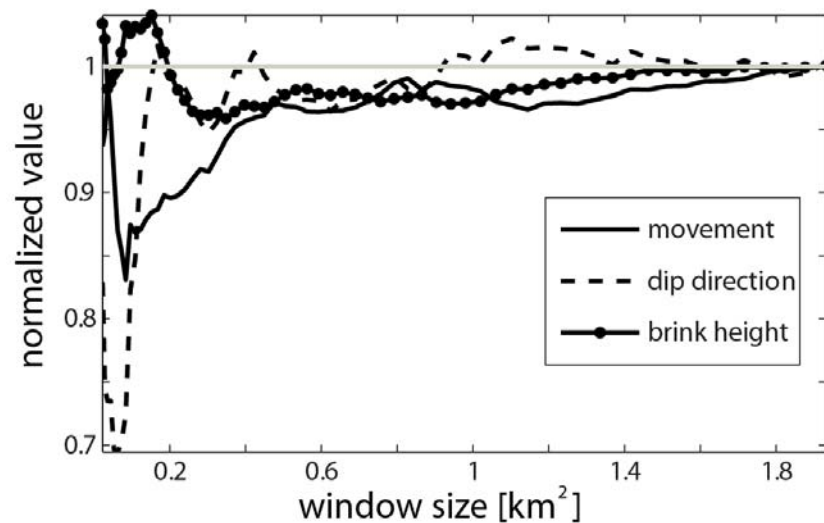


Figure 2.10: DEM derived dune observations as a function of window size. Normalized mean values of brink movement, lee surface dip direction and brink height are plotted as function of a growing sample area of White Sands. For comparability, all values are normalized by the mean value at the largest sampling window (1.96 [km²]).

2.3.3 Error

Error associated with computing dune movement using simple kinematic models is most likely attributable to using observations from nearby Holloman AFB, however, unfortunately, no onsite wind observations are available between LiDAR surveys. Additionally, wind records at Holloman AFB have been successfully compared to observed dune movement (Pedersen et al., 2015). The sediment flux vector algorithm is somewhat arbitrary chosen as other excess shear velocity sediment transport relationships exist. However, choosing another relationship would alter the magnitude of the sediment flux for a transport event, not the direction, and the kinematic model output would be similar in character.

Error associated with airborne LiDAR surveys, calculation of dune topography-surface normal vectors and the simple geometric conversion from vertical elevation change to horizontal brink displacements propagate through this analysis and contribute to the variation from the predicted trends. However, the observed values of crest height, movement and orientation are similar to other studies (Baitis et al., 2014; Baitis, 2011; Ewing et al., 2006b; Jerolmack et al., 2012). A dune field average crest trend of 334° measured by Ewing et al. (2006b) from 2,151 dune crest lines at White Sands. The average dip direction of 055° corresponds to a trend of 325° . Although similar, small deviations in crest trend are apparent within the White Sands dune field (Fig. 2.2) , as dunes encounter antecedent topography (Baitis et al., 2014; Baitis, 2011), variable water table elevation, and vegetation (Jerolmack et al., 2012).

2.4 DISCUSSION

White Sands dunes interact with an annual cycle of wind (Fig. 2.5a) to produce distributions of dune brink height, displacement length and lee surface dip direction (Fig 2.9).

The mean values of dune shape and motion are found to be dependent on the sampling area (Fig. 2.10). When measured over a representative area, the shape and motion of dune brinks all form symmetric distributions with steady mean values (Fig. 2.10) centered on the dune crest trend normal direction (55° , Figs. 2.9, 2.8). At this scale, the internal, or autogenic, variability of dune shape is directionally balanced such that GBN-type movement is observed. This area dependence of dune shape and motion is thought to describe the spatial scale at which the wind regime boundary condition, or allogenic driver, imprints on the shape and motion of dune brinks within a dune field. In this sense, GBN-type motion may be interpreted as behavior that emerges from sufficient sampling of LBM-type motion. For White Sands, the transition between LBM and GBN corresponds to six average sized dunes ($\sim 0.4 [km^2]$, Fig. 2.10). Although this result is not expected to be general, the dependence on sample size when evaluating the performance of kinematic models of bedform crests is seldom considered (Eastwood et al., 2012; Pedersen et al., 2015; Ping et al., 2014).

Autogenic processes are thought to create the substantial variation in sediment flux, even for a given compass direction (Figs. 2.8, 2.9). The variation in sediment flux is attributed to unequal mobility of sediment within White Sands. Unequal mobility may be driven by spatial variation in transport stage driven by irregular stoss slope shape, dune height, lee slope, and/or dune spacing, all of which may affect a relative sheltering from wind, as well as differences in turbulence production and dissipation. Sediment transfer from one dune to another is likely to be an additional source of variation in sediment flux. Sediment that is sourced from an upwind dune may be routed along bypass surfaces to down-wind dunes. The transfer of sediment from one dune to another may cause the upwind dune to halt, as it is leaking sediment. The leaked sediment is routed to the downwind dune, which may move rapidly due to an enhanced sediment

flux. This variation in relative transport stage is thought of as an autogenic process that occurs spontaneously simply due to the ever changing shape, height and spatial configuration of dunes.

2.5 CONCLUSIONS

Aeolian architecture is often interpreted to encode the motion of dune crests driven by an annual cycle of wind. Interpretations of aeolian architecture are frequently based on limited exposure, such as core and outcrop. Dune motion over an annual cycle of sediment transporting wind events is highly variable. Despite high variability, dune crests align as a trend line to become as orthogonal as possible to the net resultant of an annual cycle of wind. Seemingly disparate, uneven motion of dunes within White Sand is found to be very nearly normally distributed about the crest trend-normal compass direction. Therefore, dune motion measured over a sufficiently large area of White Sands offsets, so that dune motion in directions other than GBN are directionally balanced. This result elucidates how the highly variable motion of dune crests can reconcile with the development and maintenance of the dune crest organization as a trend line.

For the first time, measurement area dependence for calculating GBN-type dune motion and sediment flux from local values of dune motion is demonstrated. For the portion of White Sands investigated, it was found that the motion of a minimal set of six, average-sized dunes were required to capture GBN-type alignment and motion tied to an annual cycle of wind. While this exact result is not expected to be general, the corollary is that every small set of dunes of average size within a dune field grow to accommodate the variability of the aeolian system. Compared to analysis of dune shape and motion over a single annual cycle of wind, aeolian architecture is a highly concentrated record of past dip direction and dune motion. Therefore,

obtaining GBN-type results from aeolian strata is postulated to require sampling over a smaller area than required for a modern dune field.

2.6 ACKNOWLEDGEMENTS

Deep thanks are owed to Elizabeth Rinehart and Virginia Smith for processing LiDAR data into digital elevation models. An acknowledgement is owed to Anine Pedersen for collecting a high resolution time series of meteorological records from Holloman Air Force Base. Extraordinary helpful comments and suggestions were given by Douglas Jerolmack during the review of an earlier version of this manuscript. Funding for this work was provided by the Royal Dutch Shell Oil Company. This work does not reflect the views of the Royal Dutch Shell Oil Company.

Chapter 3: Bedform spurs: a symptom of a trailing helical vortex wake

3.1 INTRODUCTION:

Bedform spurs, sometimes called fins (Guy et al., 1966) or lee projections (Cooper, 1958), are ridges of sediment that extend downstream from the lee surfaces of bedforms (Figs. 3.1a, 3.2). Bedform spurs are pervasive features of natural bedforms (Allen, 1968; Elliott and Gardiner, 2009) and experimental bedforms (Guala et al., 2014; Guy et al., 1966; Venditti et al., 2005). A clear distinction exists between spur-bearing and non-spur-bearing bedforms, and classification schemes typically assign spur-bearing bedforms to the three-dimensional bedform category (Southard and Boguchwal, 1990). Surprisingly, bedform spurs are not viewed as criteria for determining the three dimensional nature of a bedform crest and trough.

Cooper (1958) found that aeolian bedform spur crests are aligned nearly parallel to the primary flow direction, yet formed an acute angle with their parent bedform crests. Working in a tidal channel, Elliot and Gardiner (1987) reported a similar geometric arrangement between spur and bedform crests, noting that nearly all spur crests formed a characteristic angle of 45° (α , Fig. 3.1b) with their parent bedform crests. Dietrich and Smith (1984) and Rubin (1987) noted that spurs are not stationary, but tend to migrate laterally along the lee faces of bedforms in the downstream direction (Fig. 3.1c). This motion of spurs is captured in the time-lapse animations used by Venditti et al. (2005) to document the transition from two-dimensional to three-dimensional bedforms and is reported here for dunes in the North Loup River, NE, USA (Figs. 3.2, 3.3).

Allen (1968) directly associated the occurrence of bedform spurs with a flow-parallel helical vortex positioned laterally adjacent to and/or between consecutive bedform spurs. Allen

(1968) noted that in some cases, this helical vortex was able to entrain sediment from the lee slope of the parent bedform to the point of halting its downstream motion (Fig. 3.1d). Allen also observed that grains entrained within the helical vortex were transported downstream more rapidly and at higher concentration than sediment transported across stoss slopes without helical vortices. These corridors of enhanced transport are marked by trains of ripples with bowed, convex-downstream crest lines that create a fan-like appearance (Perillo, 1995). The helical vortices also increase the characteristic excursion distance or advection length of mobilized sediment. Depending on the size of the vortex and distance to the lee face of a downstream bedform, the enhanced sediment transport associated with a flow-aligned helical vortex can either grow or erode the downstream form (Allen, 1968). Increased sediment flux captured on the lee face leads to a local increase in bedform migration rate and tends to elongate that bedform segment. When the increased sediment flux bypasses the lee face, the focused scouring beneath a vortex can break the downstream crest line, producing multiple bedforms (Allen, 1968). This behavior is commonly observed in the North Loup River when spur bearing segments of upstream and downstream bedforms are separated by a relatively short distance.

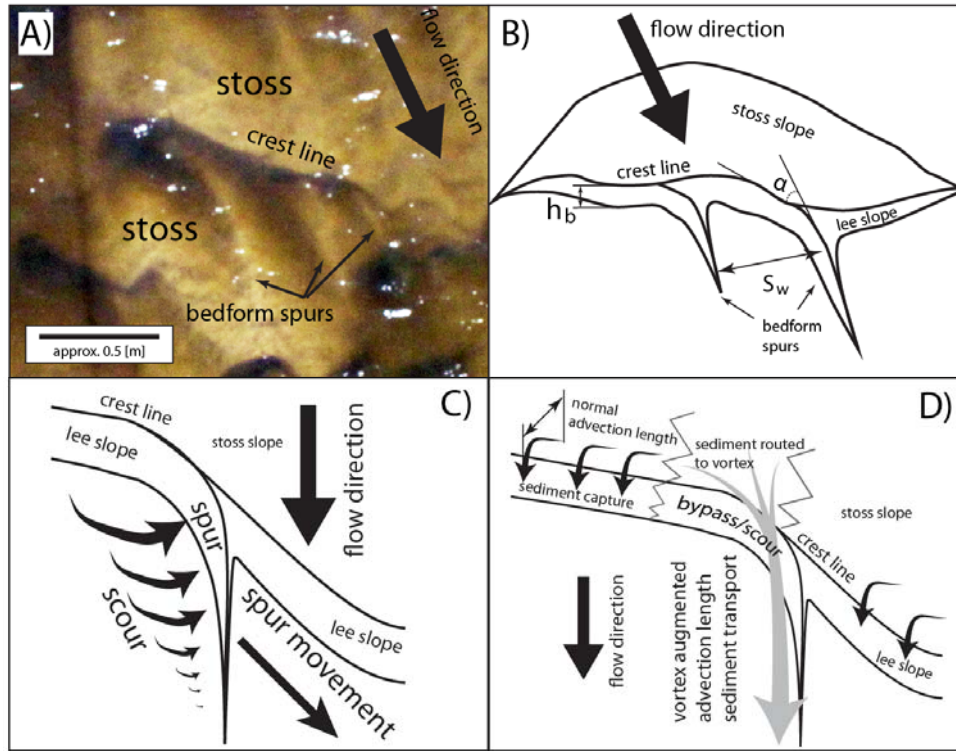


Figure 3.1: Conceptual model of bedform spur A) spur formation on an oblique lee slope of a bedform. Spur movement is always along the downstream side of the lee surface. B) Area of lee surface where sediment is entrained into spur is shown by the zig-zag gray lines. Adjacent portions of lee slope retain sediment carried over the crest of the bedform. Sediment entrained into the body of the trailing helical vortex is quickly advected downstream, shown by the large gray vector. C) Conceptual illustration of sediment and spur motion induced by scour in the interdune trough (traces are on the bed). D) Conceptualization of enhanced sediment motion driven by the trailing vortex

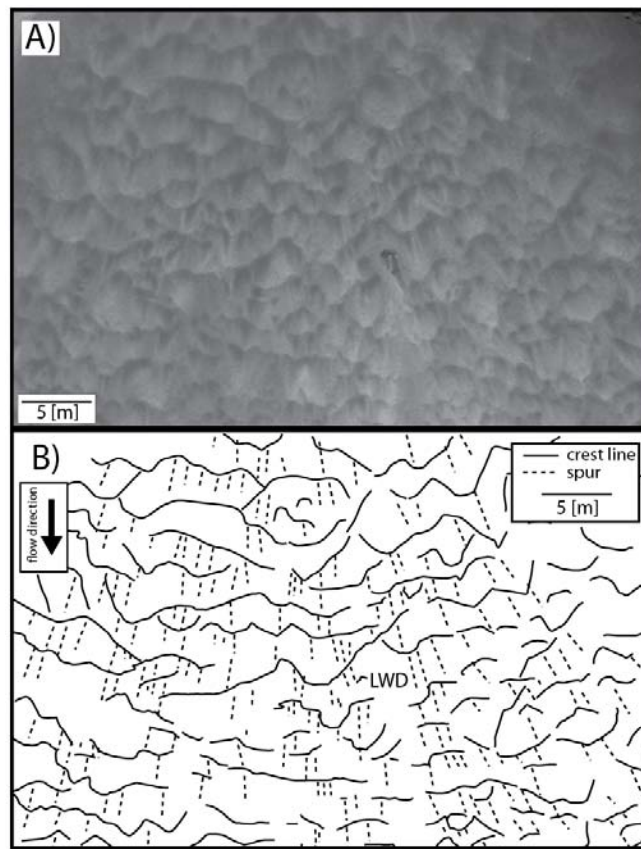


Figure 3.2: Image North Loup bedforms and crest traces A) orthorectified photo mosaic of bedforms superimposed on a bar in the North Loup River with abundant spurs. B) Traces of bedform crest lines (solid black lines) and active and relic spur crests (dashed lines) in A). The large woody debris in A) is shown as “LWD” in B).

Herein we present a collection of observations from spur-bearing bedforms. The helical vortices connected to the formation of bedform spurs (Allen, 1968, 1977) are now thought to be a symptom of a newly diagnosed wake flow in the lees of bedforms. Bedforms with portions of crests oriented obliquely to flow may generate a wake in which the helical separation vortex can detach from the lee face and trail downstream. These trailing helical vortices rotate into the direction of the flow, scour into the bedform troughs and pile this sediment into the bodies of spurs (Fig. 3.1c). We hypothesize that an oblique incidence angle between a bedform crest line and the flow direction acts as the threshold for generation of trailing helical vortices. Guided by the analysis of helical vortices that trail from cylinders (Thomson and Morrison, 1971), we demonstrate how the distance between adjacent trailing helical vortices and, therefore, spurs is controlled by the local height of the parent bedform as measured from crest to trough. Furthermore, the trailing helical vortex enhances sediment transfer between bedforms, thus serving as a driver for bedforms to deform, collide, interact and grow. These sediment-flux conduits associated with the presence of bedform spurs are a type of interaction between fluid motion and bed topography (Kocurek et al., 2010; Werner, 2003) that acts to build and maintain dynamic three-dimensional bedform morphology. To test these hypotheses, we measure the geometric configuration of active bedform spurs, and monitor the behavior of bedforms subject to the influence of a wake composed of trailing helical vortices.

3.2 METHODS:

For this study bedform spurs were observed in a reach of the North Loup River near Taylor, NE (Fig. 3.3), and in time-lapse photographs from laboratory experiments by Venditti et al. (2005). We carefully document the behavior of spurs associated with commonly observed

bedform motions: bedform deformation, interaction, and a transition between two dimensional and three dimensional bedforms. Dunes covering the bed of the North Loup River (Fig. 3.2) were used to observe the birth and death of spurs from deforming bedforms, as well as the roles of spurs during bedform interactions. Time lapse imagery of flume experiments performed by Venditti et al. (2005) captures the growth of spur-bearing bedforms from an initially flat bed. These images are used to capture the story of spur involvement with growing bedform topography, and ultimately spur involvement in the transition between two dimensional and three dimensional bedforms. Time lapse images of spur-bearing bedforms in both settings are used to create a mechanistic model of spur development in the presence of a trailing helical wake. The local height of the parent bedform (Fig. 3.4a), h_b (Fig. 3.4b), is measured next to the spur of interest and spur width, s_w (Fig. 3.4c), is measured as the cross-stream width of a spur scour, or the crest-to-crest distance between consecutive spurs. Only active bedform spurs were selected for measurement. An active spur exhibits an oblique angle with a local segment of the parent bedform crest line, and evidence of enhanced sediment transport within the spur scour as shown by an active ripple fan emerging from the vortex-scoured bedform trough (Perillo, 1995) or billows of suspended sediment within the core of a trailing helical vortex. For an example of an active spur view the time lapse video spanning 50 minutes provided in the supplementary materials (North Loup ripple fan.avi).

The geometric evolution of spurs and their parent bedforms were imaged in the North Loup River using a digital camera suspended from a 9.75 m truss. Two time lapse movies of spur-bearing bedform motion spanning 7.65 and 6.3 hours are provided in the supplementary materials (Spur_bearing_bedforms_1.avi and Spur_bearing_bedforms_2.avi, respectively). To highlight spur-bearing bedform behavior, the video files are provided at a fast and slow

framerate. Digital imagery collected using the stationary camera was corrected for geometric distortion using a lens model for the specific camera model in Adobe Photoshop. Raster data were georeferenced using several stationary control points within each image. Fluid depth was measured at every control point at a time interval of 5 minutes. Combining measurements of depth and light intensity from the collected digital imagery allows light intensity in digital images to be converted to estimates of bathymetry by the Beer-Lambert law (Jerolmack and Mohrig, 2005; McElroy and Mohrig, 2009; Soo, 2013). The bedform height and the spacing between bedform spurs were measured using orthorectified images converted to bathymetric DEMs. Bedforms were selected such that the presence of a shadow, solar reflection from the surface of the river, or piece of equipment did not interfere with the light intensity return to the camera (Fig. 3.4a). One transect was used to measure bedform height from crest to trough (Fig. 3.4b) and another to measure the spur crest to spur crest distance (Fig. 3.4c). In instances where an active but solitary bedform spur was identified, the spur width is estimated as the cross-stream distance between the spur crest and the furthest position along the oblique lee face where the trailing helical vortex could have possibly originated. Each DEM pixel carries its own value of depth and error, so the measurement procedure is performed three times per selected bedform spur. The mean value of these repeated measurements is carried forward as the accepted value and its associated standard deviation serves as a measure of uncertainty.

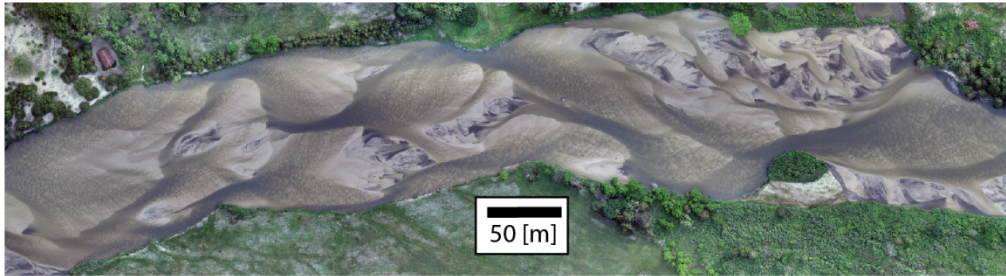
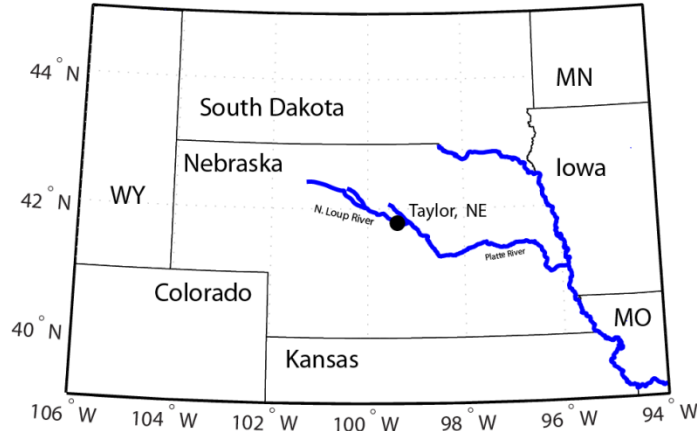


Figure 3.3: Field area. A) map showing study site study site along the North Loup River near Taylor shown by the black dot. B) Orthorectified photomosaic a portion of the North Loup River channel where measurements of spur bearing bedforms were performed.

Experimental data of Venditti et al. (2005) capture the transition from bedforms with no spurs, to a field dominated by spur-bearing bedforms. Still images from these experiments were corrected for geometric lens distortion and georeferenced utilizing a fixed grid suspended above the experimental flume bed. Non-uniform lighting above the flume bed prohibits the construction of bathymetry from the light intensity return image. Therefore bedform height is estimated using the following method: the horizontal length of the lee face (l_{lee}) is measured perpendicular to bedform crest, and assuming an angle-of-repose lee slope, converted to bedform height as $h \cong \tan(32^\circ) l_{lee}$. Time lapse imagery of this experiment is available by accessing the URL: [http://www.sfu.ca/~jvenditt/dissertation/Appendix_B/09_Flow_B_2D-3D_Bedform_Transition\(Run54\).gif](http://www.sfu.ca/~jvenditt/dissertation/Appendix_B/09_Flow_B_2D-3D_Bedform_Transition(Run54).gif).

Digital imagery of the North Loup River was also gathered using a small remotely controlled airplane with onboard camera. These images were orthorectified and merged into a photomosaic using Agisoft's photoscan software. The photo mosaics capture entire bars, nearly completely covered by spur bearing bedforms (Figs. 3.2, 3.3). These photomosaics are used to measure the acute angle formed between the parent bedform crest and linear crest of the bedform spur (α , Fig. 3.1b). To do this, both spur and parent bedform crests are traced as lines. The spur and parent bedform crest lines are converted to unit vectors \hat{s} and \hat{b} . The acute angle α between spur and parent bedform (Fig. 3.1b) is then found by using the dot product, $\alpha = \text{acos}(\hat{s} \cdot \hat{b})$.

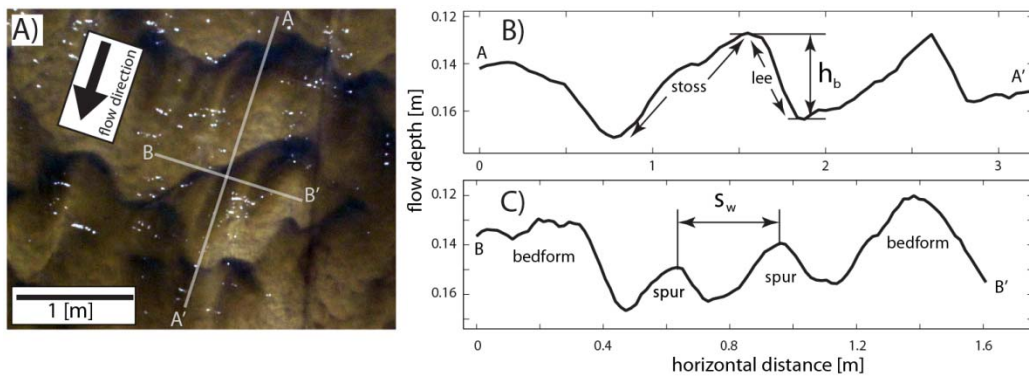


Figure 3.4: Measurements of spur bearing bedform topography A) Map view photo of spur-bearing bedforms. B) Transect of bedform topography from upstream to downstream (A-A' in map view). h_b is measured from dune crest height to lee trough. C) Transect in the across-flow direction (B-B' in map view). s_w is the distance measured spur-crest to spur-crest.

3.3 RESULTS:

3.3.1 The geometric configuration of spur-bearing bedforms

Bedform heights measured in the North Loup River and within a flume experiment ranged from approximately 1 cm to 10 cm (Fig. 3.4). The distance between spur crests were

found to range from approximately 10 cm to nearly 80 cm. Despite considerable differences in the field and laboratory environments, spur width, s_w , exhibits a common linear correlation with bedform height, h_b (Fig. 3.5). Assuming that the y-intercept equals zero yields the best-fit line, $s_w = 7.89h_b$ ($R^2 = 0.912$). The spacing between spurs is on average slightly less than eight times the local bedform height.

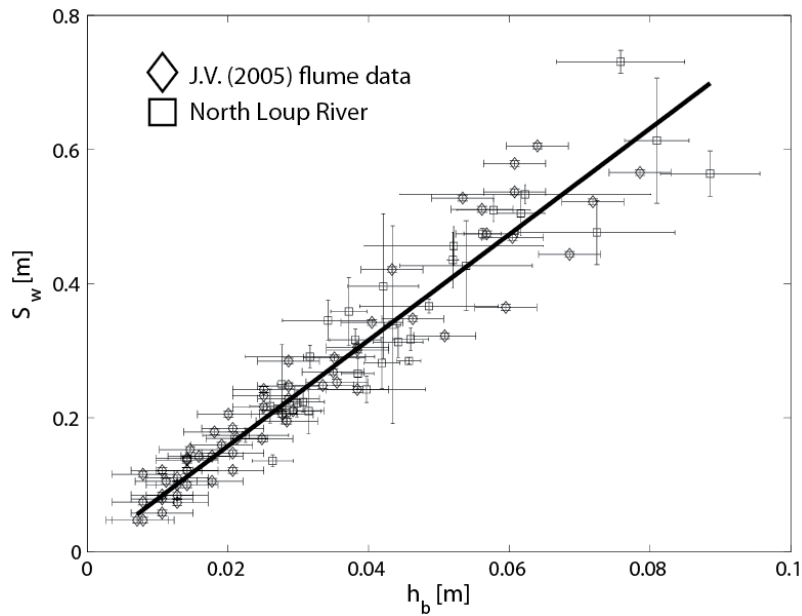


Figure 3.5: Spur width as a function of bedform height. Scatter plot of spur width s_w as a function of bedform height h_b [m]. Black diamonds are data from Venditti et al. (2005), black squares are data from the North Loup River. Linear regression model, $s_w = 7.89h_b$ ($R^2 = 0.9109$, $n = 95$) is shown by the thick black line. Error bars display the standard deviation of repeat measurements for each bedform spur.

Measured over the naturally varying topography of bars in the North Loup River (e.g., Figs. 3.2, 3.3), spur crests are found to form a mean acute angle α of 47° with their parent bedform crests (Fig. 3.6). The standard deviation for α is 8.14° (Fig. 3.6). This result is consistent with the qualitative observation of the spur-occurrences documented by Allen (1968)

and observations by Elliot and Gardiner (1987). The data suggests that there might be a relatively narrow range of angles where bedforms are capable of spawning and maintaining active spurs.

The range of α is well described by a normal distribution (Fig. 3.6).

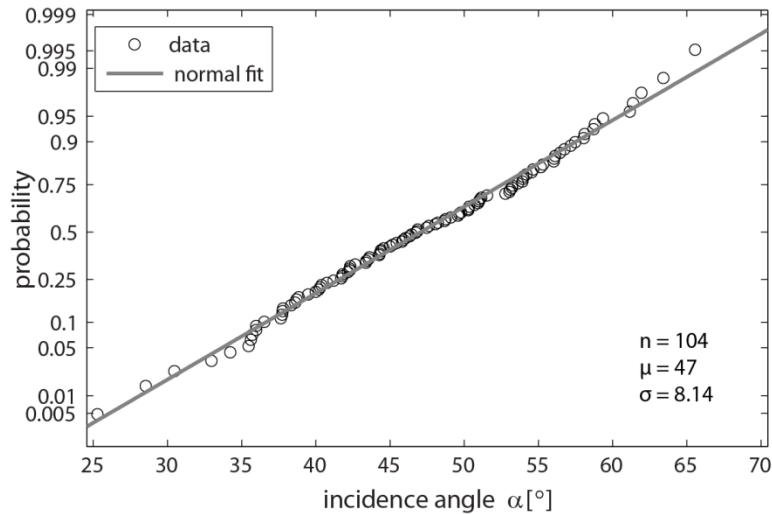


Figure 3.6: Probability plot of the angle between spur and parent dune crest. Data shown by open circles with a population of $n = 104$, the solid gray line is a fitted normal distribution with $\mu = 47^\circ$, $\sigma = 8.14^\circ$.

3.3.2 Observations of spur-bearing bedform behavior

3.3.2.1 Connecting trailing helical vortices to spurs

In agreement with Allen (1968), spurs were observed to form when bedform crests became oblique to upstream flow. Departing from Allen's ideas, however, based on direct observation of spur-bearing bedforms in the North Loup River, the formation of a spur is due to a helical vortex that trails from the lee face of the parent bedform. Once the trailing helical vortex has formed, sediment is quickly scoured from the bedform trough located immediately below the

vortex and accumulated into a ridge immediately to its side (Figs. 3.1c, 3.7). Spur growth always occurs on the side where the vortex circulation is directed upward, lifting off from the bed. The upstream-most section of spur is always slightly curved, following the filament of the vortex as it detaches from the lee face of the parent bedform (Fig. 3.7). The vortex filament and spur straightens downstream, becoming parallel to the overall flow direction. Trough scour by the trailing vortex in the lee of the parent bedform may produce a local armored surface or a lag as only coarser grains remain on the bed (Fig. 3.7).

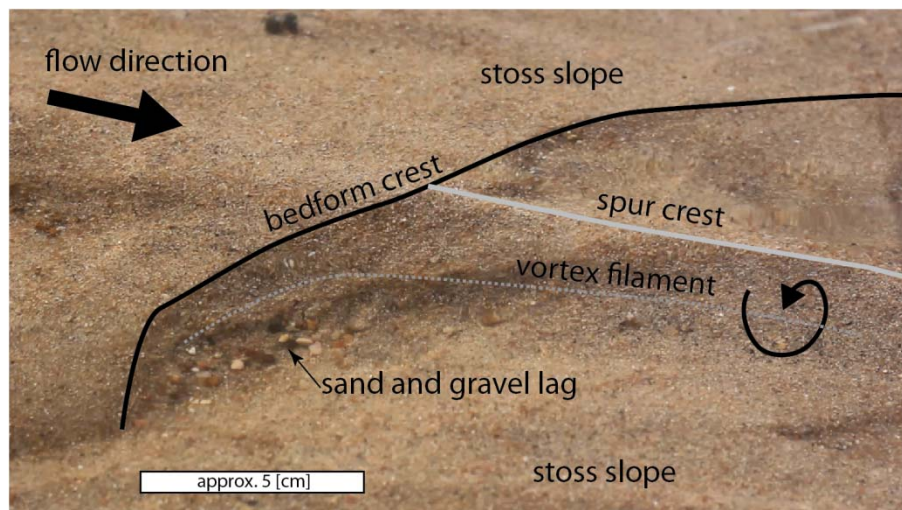


Figure 3.7: An oblique image of a spur extending from a ripple crest. The spur scour area immediately leeward of the ripple shows a gravel lag. A video clip of this active spur trough is available in supplementary materials (see `single_spur.mov`).

3.3.2.2 *Connecting trailing vortices to bedform interactions*

The effects of trailing vortices are not just local, producing trough scour and building spurs, but also allow sediment to bypass the parent bedform lee slope. Trailing vortices, therefore, enhance downstream sediment motion, but cause deceleration of the parent bedform.

Augmented sediment transport may either be routed to, or bypass the downstream bedform (Allen, 1968). Bedforms receiving the augmented sediment load undergo changes in celerity and shape. Time lapse imagery of one bedform interacting with another is shown in Figure 3.8. A time lapse video containing this trailing vortex-mediated bedform interaction is provided in the supplementary information (North Loup bedform Interaction.avi).

Sediment routed through trailing vortices is observed to drive a bedform interaction, known as defect repulsion, in Figure 3.7. The interaction begins when bedform A captures sediment routed through upstream trailing vortices (top left corner, Fig. 3.8a). This enhanced sediment delivery to bedform A allows the left termination to quickly migrate up the stoss slope of the downstream bedform (labeled B, Fig. 3.8a). The oblique crest of bedform A produces trailing vortices (Fig. 3.8b). These trailing vortices form bedform spurs, and route sediment downstream (Fig. 3.8b). The leftmost trailing vortex causes sediment to bypass the lee slope of bedform B, while sediment routed by the vortex to the right is captured by the lee of bedform B. This spatial variation in sediment capture causes erosion of the left portion of bedform B while the right portion accelerates. This vortex-mediated motion breaks the crest line of bedform B. Bedform A continues to migrate over the stoss slope of bedform B until the lee surfaces of A and left portion of B merge (Fig. 3.8c). Afterward, the newly merged crest continues to enhance sediment delivery to the severed portion of crest B, driving it downstream at a rapid rate (Fig. 3.8c,d). In Figure 3.8d, enhanced sediment transport from vortices trailing from an upstream bedform (upper left vortex filaments, Fig. 3.8d) deform the newly merged crest. Vortices cease to trail from the deformed segment of the newly merged crest in Figure 3.8d. All enhanced crest motion during the defect repulsion is simultaneously observed with the occurrence of trailing vortices and bedform spurs.

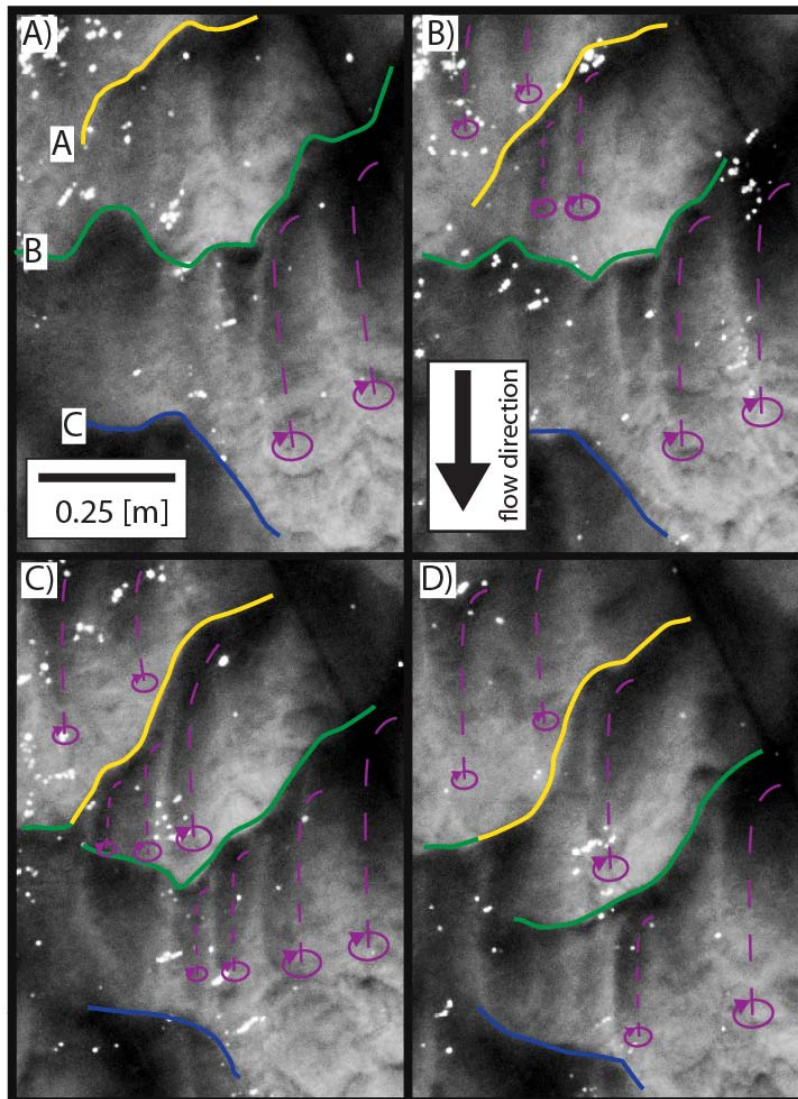


Figure 3.8: Time lapse defect bedform interaction. A-D) Snapshots of a bedform interaction imaged in the North Loup River. Primary bedform crests are mapped by solid lines. Solid line color delineates between crest originating from bedform A, B, or C. Dashed curves are interpreted trailing vortex filaments. Not all bedform spurs are interpreted as hosting trailing vortices. Bright spots are reflections of sunlight.

3.3.2.3 Growth of spur-bearing bedforms in a flume experiment

An experiment performed by Venditti (2003) captures the growth and dynamic motions of bedforms within a flume channel. In an experiment entitled “Run 53”, flow depth and velocity are held constant at 0.1516 [m] and 0.5009 [ms^{-1}], respectively. Despite steady flow conditions, a time series of images captures the spontaneous transition of straight crested (two-dimensional) bedforms (Fig. 3.9a) to sinuously crested (three-dimensional) bedforms (Fig. 3.9f) (Venditti et al., 2005). We reanalyze these images to describe the role of trailing vortices in the transition between two-dimensional and three-dimensional bedforms by a proxy, the presence of bedform spurs.

Run 53 begins with a flat sediment-covered bed. Small defects quickly appear and coalesce into nearly perfect two-dimensional bedforms with no spurs (Fig. 3.9a). Soon, however, bedform spurs appear in regions of the bed nearest flume walls, the top and bottom portions of Figure 3.9a (arrows). The occurrence of the first spurs is attributed to a decrease in fluid velocity and sediment flux very near the flume wall boundary condition. The segments of spur-bearing bedform crests near flume walls slow. The halting of bedforms nearest the flume wall creates oblique segments of bedform crests that extend from the flume walls (arrows in Fig. 3.9b; bottom arrows in Fig. 3.9c). These newly oblique segments of crest are associated with the formation of spurs further away from flume walls (Fig. 3.9b, arrows). Shown by arrows in the top portion of Figure 3.9c, bedform crests near spurs are severed and deformed, which are known non-local effects of trailing vortices documented in the North Loup (Fig. 3.8). With time, segments of bedform crests within the interior of the flume become oblique (Fig. 3.9d, arrow), and interior spurs form (Fig. 3.9e, arrows). The non-local effects of trailing vortices associated with the presence of bedform spurs allows for the creation of new oblique portions of crest

through downstream bedform crest deformation. New oblique crest shapes spawn additional bedform spurs, until the flume bed is completely populated with bedform spurs (Figure 3.9f).

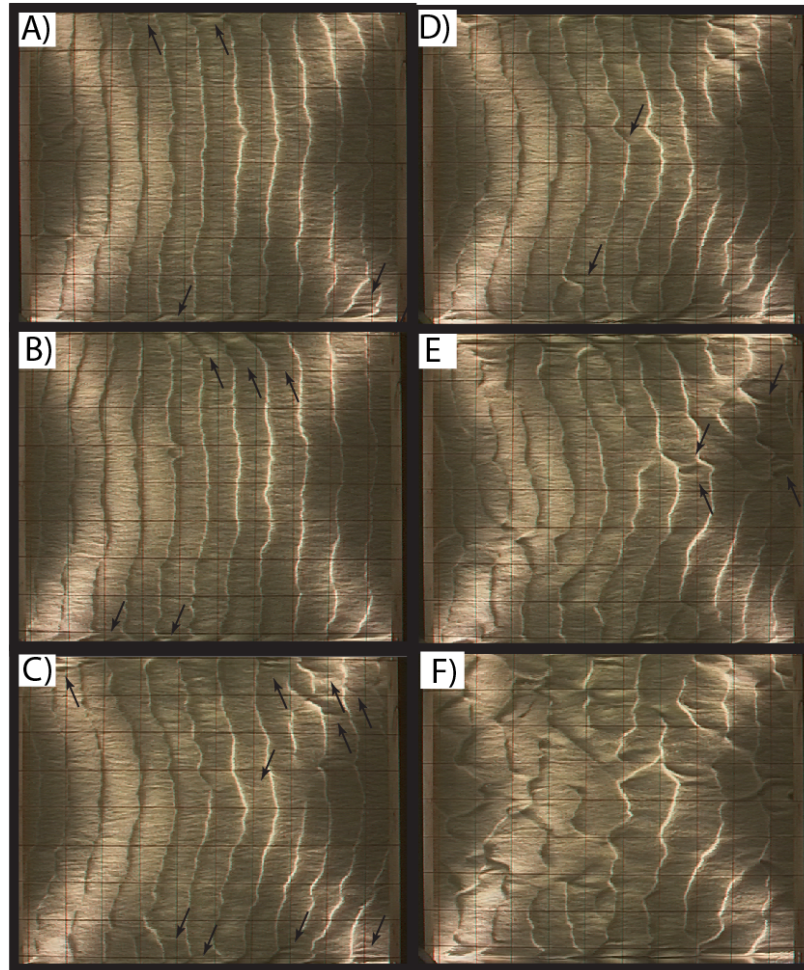


Figure 3.9: The transition between 2D and 3D bedforms from Venditti et al. (2005). Flow direction is from left to right in each image. A) Experimental time elapsed (t) = 260 sec, First spurs shown by arrows near flume walls (top and bottom of image). B) t = 340 sec . Spurs propagate inward from flume walls. C) t = 650 sec. Bedforms begin to interact with bedforms due to juxtaposed halting and acceleration of bedform crests. D) t = 670 sec. Large segments of bedform crest within the interior of the flume become strongly oblique to flow. E) t = 780 sec. Previously identified oblique crest lines now bear spurs, and interacting crest lines. F) t = 1130 sec. Bedform spurs and bedform interactions are visible within the entire flume area.

Shortly after bedform spurs have fully populated the flume bed, pronounced increases in average values of bedform crest height, h_b (Fig. 3.4b) (Venditti, 2003; Venditti et al., 2005) and wavelength, or spacing between primary bedform crests, were observed in run 53 (Fig. 3.10). The difference in bedform crest height and wavelength is illustrated by comparing of the initial two-dimensional bedforms in Figure 3.9a with the spur-rich bed in Figure 3.9f. Bedforms continue to increase h_b and wavelength through snapshots in Figure 3.10a-d. Increases in bedform height, h_b , are correlated with increases in s_w , the spacing between spur crests, shown by the black diamonds plotted in Figure 3.5. These increases are qualitatively visible by comparing bedforms and spur spacing in Figure 3.10a and Figure 3.10c or 3.10d. Near the end of the flume experiment, small superimposed bedforms were present on the stoss slopes of primary bedforms (Fig. 3.10d). These superimposed bedforms form oblique incidence angles and are host to small spurs shown by arrows in Figure 10d.

Bedform spurs are observed to be a nearly ubiquitous morphological component of three-dimensional bedforms (Figs. 3.2, 3.8, 3.9, 3.10). Bedform spurs, and the associated non-local effect of their trailing vortices mediating sediment transfer between individual bedforms is a mechanism involved in the spontaneous transformation from two-dimensional to three-dimensional bedforms (Fig. 3.9). The non-local effects strongly contribute to the behavior of three-dimensional bedforms (Fig. 3.10), and are even present in superimposed bedforms on the stoss slopes of three-dimensional bedforms (Fig. 3.10d).

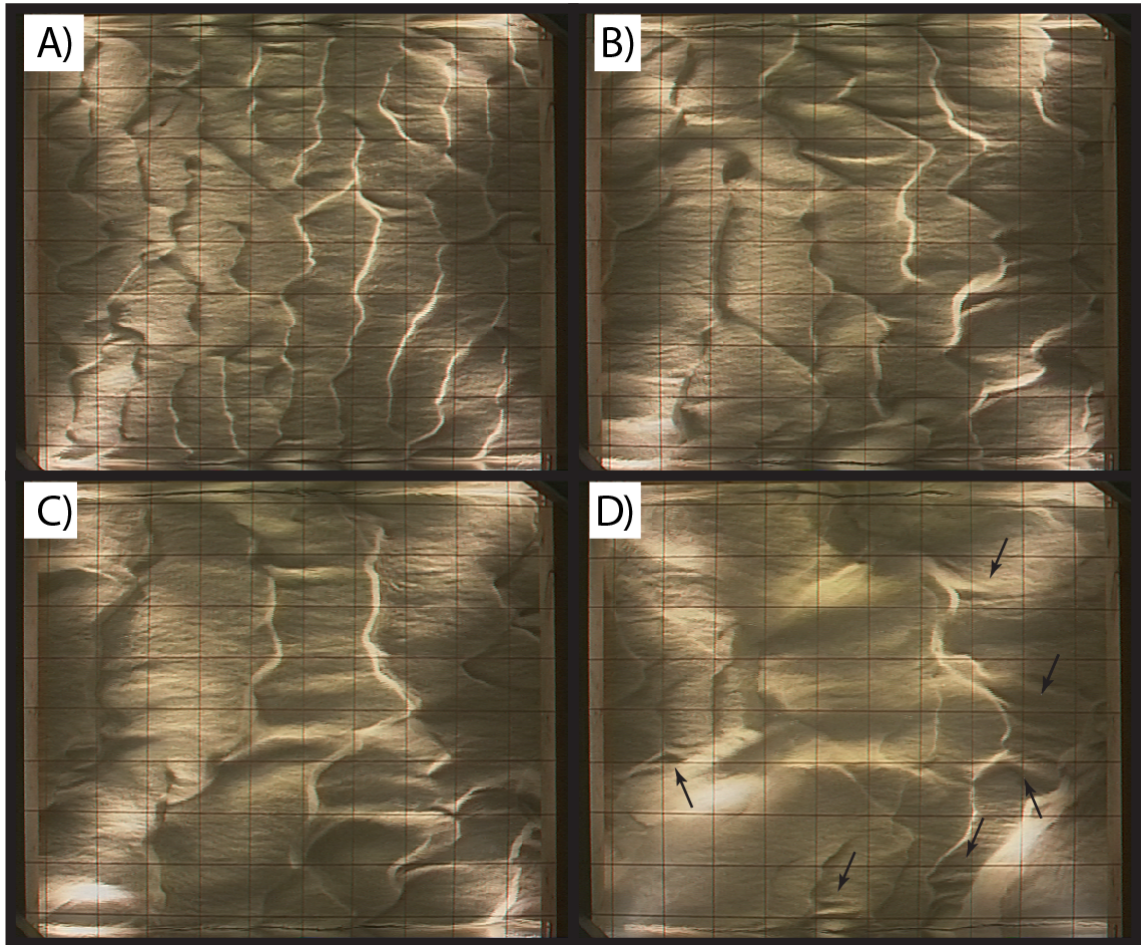


Figure 3.10: Deformation of 3D bedforms beyond the 2D-3D transition are captured in images recorded by Venditti et al. (2005). A) time elapsed = 1130 sec. Time snapshot where spurs first fully occupy the bed. B) $t = 2340$ sec. Growth in bedform height, wavelength, and increased distance between spur crests. C) $t = 3810$ sec. Further bedform growth. D) $t = 19230$ sec. The largest primary crests extend from flume wall to wall. Superimposed bedforms are long lived, and deform sufficiently to form their own spurs (arrows).

3.4. DISCUSSION:

Allen (1977) correctly noted that the occurrence of spurs within a bedform field is tied to occurrence of flow-aligned vortices within the flow field. We have shown how each spur arises from a sediment transport pattern that is governed by a trailing vortex. Here we develop a new model for the occurrence and geometric configuration of a trailing vortex associated with the wake of a bedform using measurements defining the onset and geometric configuration of trailing vortices within a wake generated by a cylinder. The wake created by a cylinder takes on three distinct regimes depending on the angle of incidence, α , which is measured similarly to bedforms as the acute angle formed between the upstream flow direction and the long axis of the cylinder (Snarski, 2004; Wei et al., 1983). At small incidence angles, $0^\circ \leq \alpha \leq 25^\circ$, an internal boundary layer grows with distance downstream from the point of flow attachment on the cylinder (Fig. 3.11). This span of incidence angles defines the attached boundary layer regime. At larger incidence angles, $25^\circ \leq \alpha \leq 55^\circ$, counter rotating helical vortices are shed from and trail the cylinder (Fig. 3.11). This regime is called the trailing helical vortex regime. For yet larger angles of incidence where $\alpha > 55^\circ$, a vortex spanning the length of the cylinder remains attached to its lee surface (Snarski, 2004; Strouhal, 1878; Wei et al., 1983) (Fig. 3.11). This regime is referred to as the roller regime, in which a counter rotating vortex filament runs parallel to the long axis of the cylinder.

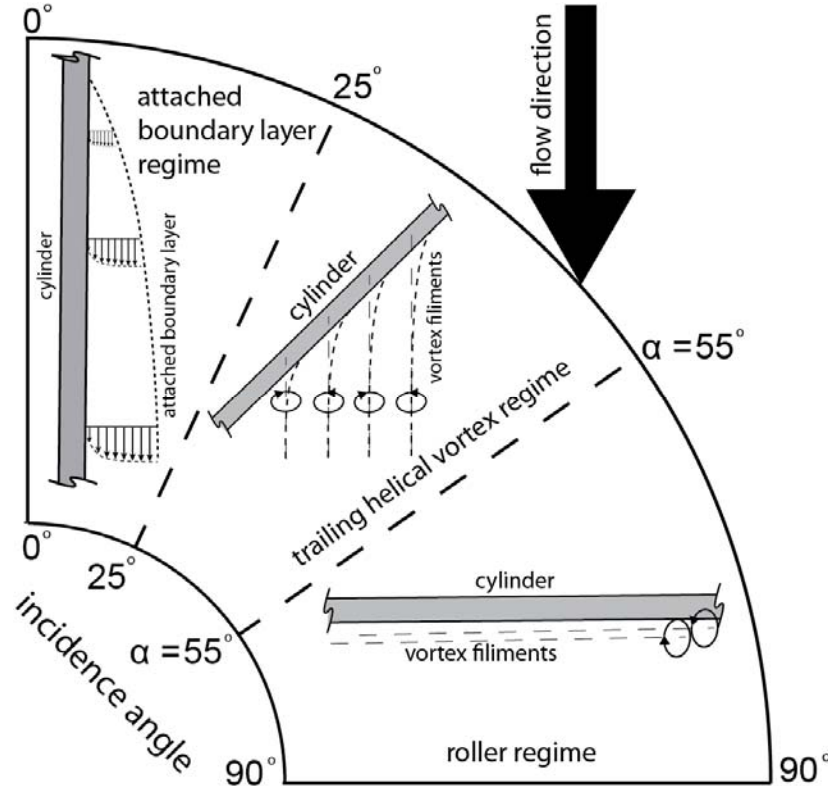


Figure 3.11: A conceptual model of fluid circulation around a circular cylinder (gray bar) at various incidence angles, which is subtended between the long axis of the cylinder and flow direction (top to bottom of cartoon). Vortex filaments are shown as thin dashed lines, and vortex circulation direction is shown by the circular arrow placed concentrically with each vortex filament. Thick dashed lines labeled with values of incidence angles are guides used to discern between wake regimes, an attached boundary layer regime, a trailing helical vortex regime, and a roller regime.

3.4.1 A conceptual model for the creation of bedform spurs:

Study of fluid circulation around a cylinder suggests that an incidence angle of $25^\circ \leq \alpha \leq 55^\circ$ with the upstream flow direction and a flow velocity sufficient for vortices to detach ($Re \gg 100$) are criteria for helical vortices to trail from the lee surface of a bedform. This range of incidence angles agrees with the 45° acute angle measured between spurs and their parent

bedform crests by Elliott and Gardiner (2009) and the distribution of measured angles for spurs on dunes covering bar topography within the North Loup River (Fig. 3.6).

Any gradient in sediment flux along the crest of a bedform will cause uneven displacement (Fig. 3.12a), which drives the bedform to become more oblique to upstream flow (Fig. 3.12b). Predicted from Figure 3.11, once a portion of bedform crest forms an incidence angle of approximately 25° to primary flow, a helical vortex may trail from the lee slope (Fig. 3.12c). The sequential photos shown in Figure 8a, b demonstrate the formation of a bedform spur, and therefore the trailing of a helical vortex, once the parent bedform crest achieved an oblique incidence angle. Provided that flow velocity is sufficient for vortices to detach ($Re \gg 100$), an angle of incidence over 25° but less than 55° , with some variability, is suggested as a criterion for initiating trailing vortices from bedforms.

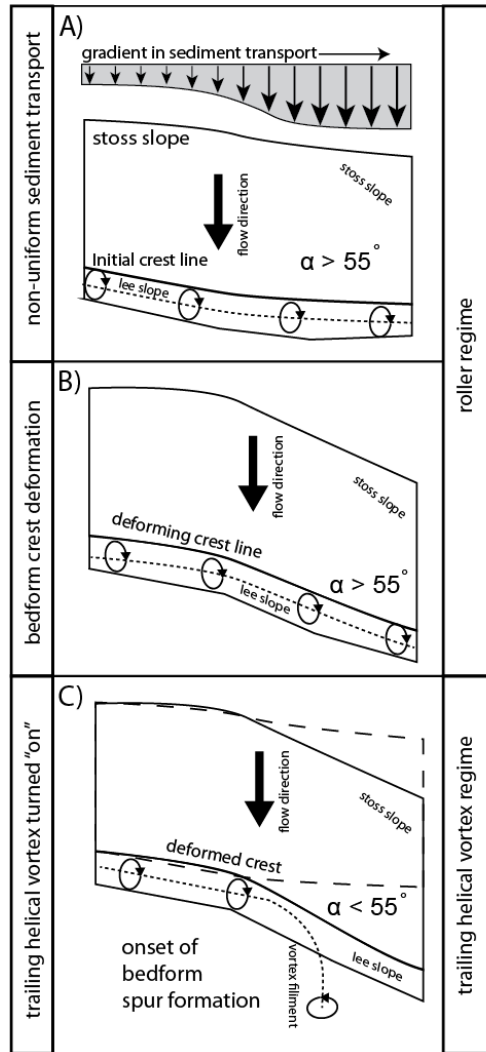


Figure 3.12: Trailing vortex formation. Conceptual model illustrating how crest deformation allows a trailing helical vortex to form. A) A nearly transverse bedform crest with a roller regime wake is shown in the plan view. B) Crest deformation ensues due to the gradient in sediment transport shown in A), which is a function of the incidence angle. C) The threshold incidence angle for the trailing of a helical vortex has been exceeded. The initial stoss slope outline is shown by dashed lines.

3.4.2 The geometric configuration of trailing vortices:

The Strouhal number, S , is a dimensionless group that is used to compare fluid acceleration to fluid inertia (Strouhal, 1878). The dimensionless group is constructed as $S = nd/U$ where n is the characteristic frequency of vortex production within a flow [t^{-1}], d [L] is a length scale, typically the diameter or height of a flow obstruction, and U [t^{-1}] is the velocity of the fluid upstream and away from influence of the flow obstruction, often referred to as a free stream velocity. Traditionally, the Strouhal number has been applied to explain the production of vortices that shed from an obstacle with its long axis nearly perpendicular to the upstream flow direction, such as the “singing” telegraph wires (Strouhal, 1878). Thomson and Morrison (1971) applied a modified Strouhal number to predict the regular spacing of counter rotating vortex filaments that trail from a cylinder between incidence angles $25^\circ \leq \alpha \leq 55^\circ$, shown in Figure 3.11.

The geometric model of Thomson and Morrison (1971) describes the spacing of trailing helical vortex filaments from a cylinder of constant diameter using what they term a cross-stream Strouhal number. A full derivation of the wake model is provided in Thomson and Morrison (1971), however, the premise of their model is that the time-shedding of vortex filaments from an obstacle, determined using the traditional Strouhal number can be translated into a distance traveled by fluid along the length of the cylinder, if the fluid velocity and incidence angle is known. Their cross-stream Strouhal number is given as $S = \frac{1}{2(\frac{g}{d}) \tan \alpha}$ where g is distance separating adjacent trailing vortices along the cylinder lee. The distance between filaments of opposite sign measured orthogonal to the upstream flow direction is given as $l = g \cos \alpha$ (Fig.

3.13a). Adjacent helical vortices rotate in opposite directions because they emerge from opposite half-circles in the lee of the cylindrical obstruction (Fig. 3.13a).

The shape of helical vortex filaments that trail from both bedforms and cylinders are geometrically similar in their plan view shape. In both systems, the vortex filament originates on the surface of the obstruction and curves away from the lee surface of the obstruction strongly until the filament becomes parallel with upstream fluid motion (Fig. 3.13a). In the model of Thomson and Morrison (1971) trailing helical vortices shed from the same half-circle along a cylinder rotate in the same direction (Fig. 3.13b). Consecutive vortices trailing from a single bedform are always of like sign, therefore, the distance between consecutive helical vortices trailing from a bedform may be thought of as the distance between vortex filaments of like sign trailing from one half-space of an oblique cylinder (Fig. 3.13b, c). The height of a bedform can, in turn, be thought of as half of the diameter of an oblique cylinder (Fig. 3.13b, c). Restating the geometric model of Thomson and Morrison (1971) in terms of a bedform spur spacing, $s_w = 2g \cos \alpha$ and bedform height $h_b = \frac{d}{2}$. Solving for the ratio of spur width to bedform height, we obtain $\frac{s_w}{h_b} = \frac{2 \cos \alpha}{S}$. Choosing an approximate incidence angle of $\alpha = 45^\circ$, and solving we find $\frac{s_w}{h_b} = \frac{1.4142}{S}$. This geometric model for the occurrence of spurs now directly relates the Strouhal number to the bedform height and the spacing between consecutive trailing vortices. We have already shown that bedform spur spacing is linearly correlated with parent bedform crest height (Fig. 3.5). This linear relationship between height and the interpreted spacing of trailing helical vortices as defined by spur spacing suggests that a constant Strouhal number would directly relate s_w to h_b , and α .

The Strouhal number for a bluff body is often cast as a function of the Reynolds number (Norberg, 2003). For Reynolds numbers ranging $10^2 < Re < 10^5$ the Strouhal number is

typically found to be very nearly invariant at a value of $S \cong 0.2$ (Norberg, 2003). In practice, the Strouhal number remains largely independent of the Reynolds number for many engineered and natural systems (Levi, 1983). Even for fluvial bedform wakes, the Strouhal number is nearly invariant spanning scales of natural and experimental bedforms and fluid velocity (Venditti and Bennett, 2000). Assuming $S = 0.20$, the spacing between spur crests (Fig. 3.13c) is now directly estimated using the height of the bedform $\frac{s_w}{h_b} = 10 \cos \alpha$. For incidence angles of $\alpha = 25^\circ$ and 55° that represent the extremities of the trailing helical vortex wake regime, the ratio is predicted to be, $\frac{s_w}{h_b} = 9.1$ and 5.7 , which agrees with the observed ratio of 7.89 (Fig. 3.5).

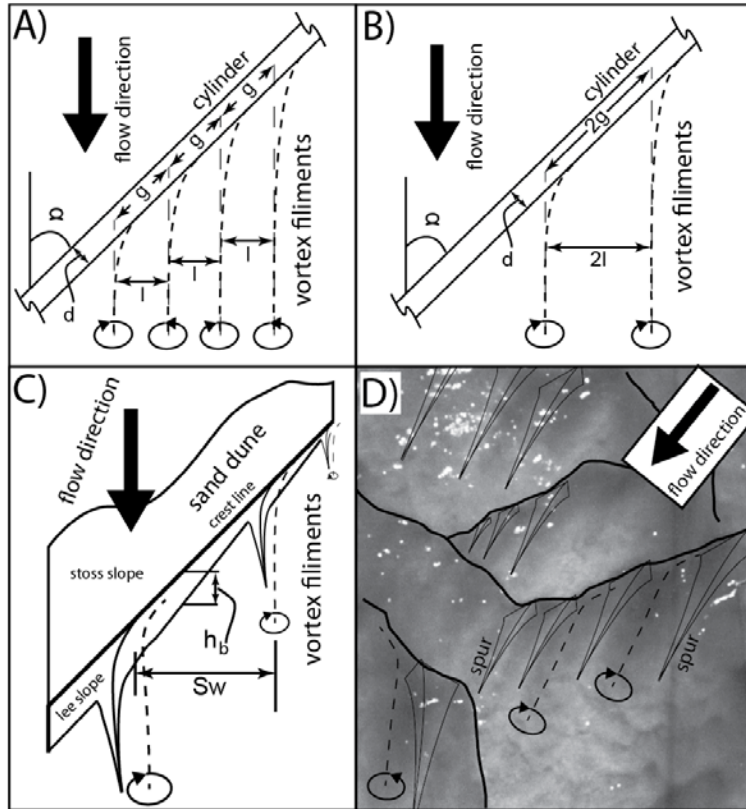


Figure 3.13: Geometric model of trailing vortices. A) Geometric model of trailing helical vortex wake adapted from Thomson and Morrison (1971). B) The geometric model of (A) adapted to show the wake structure trailing from one side of a circular cylinder. C) Conceptual model of spur width s_w as a function of bedform height, h_b as an analogy to one-sided flow around a circular cylinder. The bedform model shows spur spacing as a function of local bedform crest height. D) Snapshot of bedform morphology showing uneven spur crest spacing along the lee slope of bedforms of non-uniform height.

3.4.3 Downstream crest deformation

A trailing vortex enhances sediment transport over a relatively narrow swath of bed area. As observed in Figure 3.7, a trailing vortex can either route sediment to or bypass a downstream bedform. Although the nuances of successful sediment capture by a downstream bedform are both detailed (Mohrig and Smith, 1996) and highly circumstantial, two end-member outcomes are roughly attributed to proximity of the two bedforms. If the two bedforms are relatively far

apart, sediment routed by a trailing vortex is captured on and added to the lee face of the downstream bedform (top row, Fig. 3.14). If the two bedforms are too close, a trailing vortex ejects sediment past the lee of the downstream dune such that most sediment bypasses the downstream bedform entirely (bottom row, Fig. 3.14).

If a bedform captures sediment from a trailing vortex (Fig. 3.14a), that segment of the bedform extends and migrates downstream at a faster rate than if there had been no vortex (Fig. 3.14B). The deformed crest may form oblique incidence angles, and, therefore, create new spurs and additional zones of augmented sediment motion (Fig. 3.14c). Alternatively, if crest deformation forces the incidence angle of spur-bearing bedform outside of the range of incidence angles suitable for trailing vortices, existing vortices can cease to exist. Bedform deformation may birth new trailing vortices and kill existing trailing vortices.

If a bedform with trailing vortices is more proximal to a downstream bedform, vortex-mediated sediment transport may eject past the lee face of the downstream bedform (Fig. 3.14d, e). This is the necessary condition for trailing vortices to completely erode the downstream bedform, severing it into two (Allen, 1968). The erosion of the downstream bedform may also cause deformation of the bedform crest nearest the new terminations. The newly created terminations may become deflected downstream, or merge lee slopes with one or more of the terminations from the upstream bedform. Figure 14F shows a bedform with trailing vortices that erode a downstream bedform, then asymmetrically merge lee slopes with the downstream bedform. This bedform behavior is known a style of bedform interaction, termed “lateral linking” (Kocurek et al., 2010). In a similar fashion, a lateral linking can be thought of as a half “defect repulsion”, another commonly observed bedform interaction (Kocurek et al., 2010). The speed at which these interactions propagate through a field of bedforms is substantially more

rapid than mean bedform celerity (Werner and Kocurek, 1997). Here this is due to the rapid motion and deformation of bedform crests imparted by trailing vortices, which self-propagate through fields of bedforms.

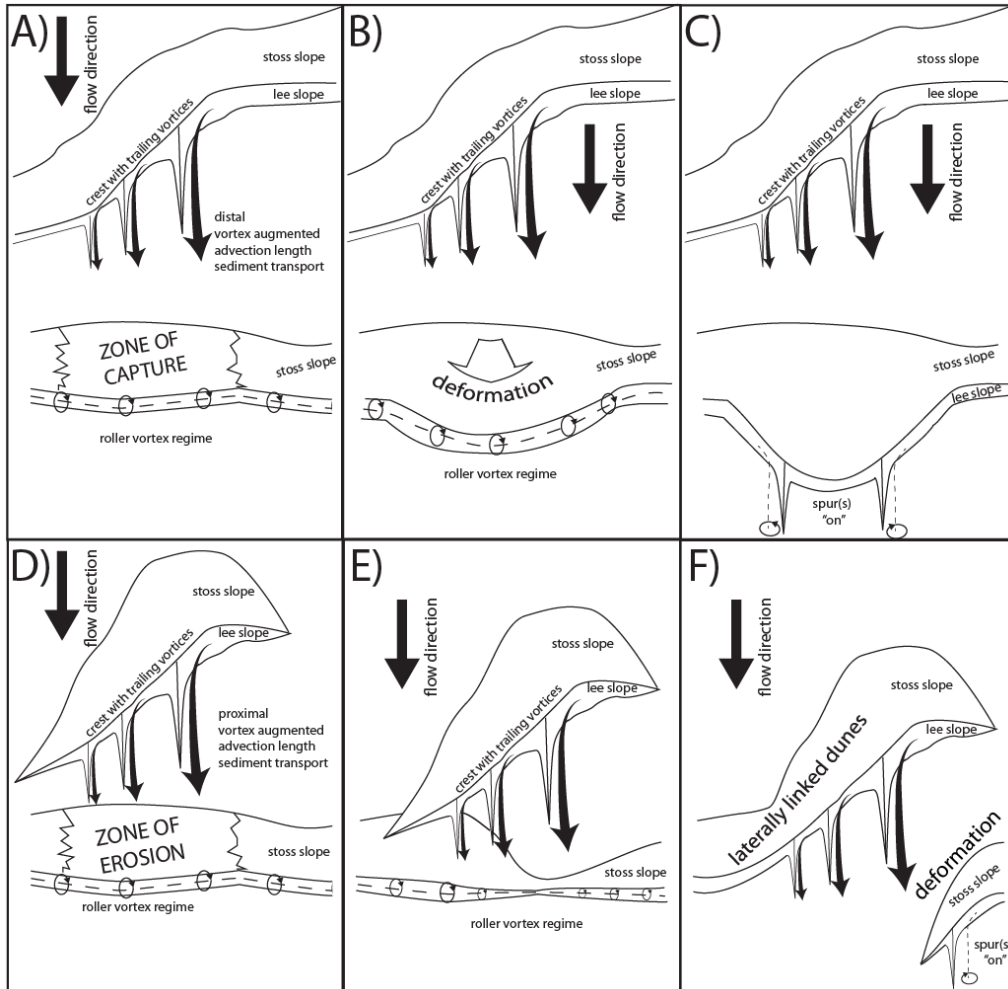


Figure 3.14: Sediment routing by trailing vortices. (Top row) Trailing vortices routing sediment to a bedform. A) The upstream bedform trails a helical wake, which routes an augmented sediment flux to the downstream bedform. B) The middle portion of the downstream bedform extends, growing in wavelength due to the augmented sediment delivery. C) The crest deformation of the downstream bedform may be sufficient to trail helical wake, and create new spurs. (Bottom row) D) An oblique upstream spur-bearing dune approaches a downstream dune. E) Trailing vortices scour through the downstream dune. The left termination of the upstream bedform climbs the stoss slope of the downstream bedform. F) The left portion of the lee slopes of the upstream and downstream bedforms merge. The free termination deforms and may create new trailing vortices and spurs.

3.4.4 The trailing helical vortex motor

Gradients in sediment transport are ubiquitous within natural and experimental fields of bedforms. Spur-bearing bedforms create gradients in sediment flux, through sediment conveyance and ejection by trailing vortices. From observations gathered in the North Loup River and in the experiments of Venditti et al. (2005), over a bedform field, both the quantity of sediment and the excursion lengths for this sediment are enhanced by trailing vortices. Downstream bedforms grow to accommodate the augmented sediment flux, and in doing so, alter their height and wavelength. Here, this morphodynamic feedback is termed the *trailing helical vortex motor*. The term motor is used to describe the self-propagation of trailing vortices due to trailing vortex mediated sediment transport and downstream bedform deformation. The motor engages when a deformed crest enables a helical vortex to trail from a parent bedform. Trailing vortices enhance sediment transport, thereby deforming downstream bedform crests, spawning additional trailing vortices. The ensemble of trailing vortices greatly enhances bed-material transport within a field of bedforms. By conservation, this enhanced transport must increase the wavelength and height of bedforms, as sediments are sourced directly from the bed. Increased bedform height increases the distance between spurs. An increased spur width allows more sediment to be entrained from the lee slope of the parent bedform of a trailing vortex, further increasing vortex-mediated sediment transport. This positive or self-amplifying morphodynamic feedback is here called the trailing helical vortex motor.

The incidence angle control for the formation of trailing vortex wake and bedform spurs is exceptionally clear in the flume experiments performed by Venditti et al. (2005) (Figs. 3.9, 3.10). The experiments of Venditti et al. (2005) detail the sudden and dramatic change between two dimensional and three dimensional bedforms. Although this transition is common attributed

to a change in the velocity of the sediment transporting fluid, it occurs spontaneously with no change in mean values of fluid velocity. The generation of free crest terminations, defects, begins slowly in the experiment, then the production of defects overwhelms the two dimensional pattern. The rapid motion of these defects, and their interactions with the otherwise straight crests are attributed to the dramatic change from two dimensional to three dimensional crests (Venditti et al., 2005). The production of these defects, crest bifurcations and interactions is largely driven by the trailing helical vortex motor initiated by a local gradient in sediment transport near flume walls.

Perceived limitations on vortex mediated bedform growth include “container” boundary conditions such as flow depth, flow steadiness and sediment supply (Kocurek et al., 2010). If a trailing vortex breaks on the free surface of a flow, the upward component of velocity is diminished and sedimentation of the vortex enhanced sediment transport occurs. Flow must be sufficiently steady in both direction and magnitude to allow for bedforms to form oblique segments of crest, and trail vortices. Experiments performed by Perillo et al. (2014b) investigated bedform growth and shape using oscillatory flow of various frequencies and flows with combined oscillatory and unidirectional components. Only flows with longer oscillatory periods, or larger components of unidirectional flow produced spur-bearing bedforms (compare their figures 5 and 6).

3.5 CONCLUSIONS:

Spurs populate fields of ripples (Venditti et al., 2005), combined flow bedforms (Perillo et al., 2014a), fluvial (Allen, 1968; Allen, 1977; Elliott and Gardiner, 2009) and aeolian dunes (Cooper, 1958). Even so, bedform spurs are ignored in practically every facet of bedform studies.

The presence of spur-bearing bedforms is a symptom of a previously unrecognized trailing helical wake regime. By analogy, we adapt a cross-stream Strouhal number that describes the configuration of helical vortex filaments trailing from a circular cylinder (Thomson and Morrison, 1971) at an oblique incidence angle to upstream flow to describe the regular occurrence of spurs along the lee surface of bedforms. Measurement of bedform spur orientation to parent bedform crest confirms that spurs are likely to host active trailing helical vortices for incidence angles $25^\circ \leq \alpha \leq 65^\circ$ (Fig. 3.6), in good agreement with the range found for circular cylinders $25^\circ \leq \alpha \leq 55^\circ$ (Fig. 3.11). Although the spacing between consecutive spurs is predicated to be a function of both parent bedform crest height and incidence angle the spur spacing is well described by a linear relationship with only parent dune height. The trailing vortex allows sediment to largely bypass both the lee slope of the parent bedform and the spur trough that cradles the trailing vortex. By inhibiting deposition, trailing vortices create and maintain the narrow window of angles (α) measured between spur and parent bedform crest lines.

Bedform spurs are typically not sought or reproduced by state-of-the-art models that simulate dynamic bedform topography (Durán et al., 2010; Jerolmack and Mohrig, 2005; Khosronejad and Sotiropoulos, 2014; Narteau et al., 2009; Werner, 1995). The substantial modeling efforts of Khosronejad and Sotiropoulos (2014) produce sand waves that reproduce the transient behavior of experimental primary bedform crests (Venditti et al., 2005), however, bedform spurs and their associated dynamic behavior are not reproduced. The ability to resolve bedform spurs and the larger scale dynamic bedform behavior associated with their presence could be envisioned as a benchmark for forward models of bedform topography.

Ubiquitous gradients in sediment transport within fluvial channels, aeolian landscapes and flume channels drive deformation of bedform crests. Crest deformation forms oblique incidence angles, a trailing helical wake, and bedform spurs. Trailing helical vortices that reside within the scour pits of bedform spurs rapidly move sediment downstream. The augmented and focused sediment delivery causes local deformation, and the spawning more trailing helical vortices. Bedform deformation begets bedform deformation, a feedback between the birth and death of trailing helical vortices, vortex-mediated sediment routing, and bedform deformation. The feedback grows bedform topography until trailing helical vortices are unable to further enhance sediment transport between bedforms. Therefore, trailing helical vortices are shown to mediate interaction between particles, fluid and topography that drives some of the emergent behavior of bedform fields.

3.6 ACKNOWLEDGEMENTS:

We are very grateful for field work assistance from John Shaw, Yao You, Ben Cardenas, Wayne Wagner, and David Brown. Vastly helpful conversations about a trailing helical wake regime were held with Ben Cardenas, Wayne Wagner, Nick Howes, John Martin, Will Andersen and Gianluca Blois. This project was supported by an NSF grant to G. Kocurek and D. Mohrig.

Chapter 4: A surface model of aeolian dune topography

4.1 INTRODUCTION

We present a surface model of aeolian topography and apply it to approximate aeolian dune growth in response to different hypothetical bedform field boundary conditions. The aeolian surface model is a modification of the surface evolution equation presented by Jerolmack and Mohrig (2005). The original surface evolution equation cast the dynamic motion of subaqueous dune topography driven by unidirectional flow as a nonlinear relationship between sediment flux and bedform topography, subject to stochastic variability. The surface model for aeolian bedforms is created by implementing two principle modifications to the original model. First, the surface evolution equation is discretized in two dimensions. Therefore, sediment transport can occur in any azimuth direction. Second, sediment elevation can be prescribed along a side of the rectangular domain which is useful to simulate dune growth from a sediment source area. Despite these modifications, the model presented here attempts to preserve as much similarity to the original surface evolution equation as possible.

Stochastic bedform motion is envisioned to arise from a hierarchical cascade of interactions between fluid, grains and topography within fields of bedforms (Kocurek et al., 2010). The bedform surface evolution equation abstracts the complex hierarchical cascade of bedform interaction as a simple non-linear relationship between topography and boundary shear stress and sediment flux (Jerolmack and Mohrig, 2005). Bedform fields are subject to boundary conditions, which, in a departure from the mathematical sense, describe any phenomena external to the bedform field. Bedform field boundary conditions can be imagined as a spatially restrictive sediment source area, or perhaps an annual cycle of sediment transporting wind

events, termed wind regime, which drives interaction within the field of bedforms (Kocurek et al., 2010). The two principle modifications of the original model allow modeled aeolian bedform topography to inherit morphological traits from two boundary conditions common to natural aeolian bedform fields: a multidirectional sediment transport regime, and a spatially restrictive source area, the region where bedforms originate.

The aeolian bedform surface model is driven using four permutations of the two boundary conditions to resolve the inheritance of signals from various environmental conditions. A unimodal and bimodal set of sediment transport directions are used to grow synthetic dune topography with and without the constraint of a prescribed sediment source elevation. In these case studies, bedform topography interacts, deforms, and grows through time and space. Bedform growth with time is demonstrated to replicate bedform growth with distance away from the prescribed sediment elevation boundary condition. However, the rates at which bedforms morphologically “age” with time and space is demonstrated to be highly dependent on the transport regime boundary condition.

4.2 METHODS

4.2.1 An aeolian surface model

This model driven study is a direct extension of the bedform surface evolution equation presented by Jerolmack and Mohrig (2005). At the core of the surface evolution equation is the ability to resolve the growth of bedform topography. The modeling framework presented by Jerolmack and Mohrig (2005) describes the growth and deformation of a surface, the interface between sediment and the sediment transporting fluid. The primary strength of their model is the

realistic reproduction of bedform growth and scaling of topographic roughness through space. The original surface evolution equation of Jerolmack and Mohrig (2005) arises from combining three components that describe bedform growth, deformation and motion as a morphodynamic feedback. This feedback is described by three components: dynamic bedform topography, η , basal shear stress, τ_x and saturated sediment flux q_s . The feedback is formed by solving for τ_x as a function of η . Through conservation of sediment, η is then modified by saturated sediment flux, q_x . Completing the morphodynamic feedback, q_x is cast as a power law relationship of τ_x (Jerolmack and Mohrig, 2005; Meyer-Peter and Müller, 1948). This system captures the spontaneous growth and migration of trains of bedforms as a non-linear wave from rough topography (Jerolmack and Mohrig, 2005).

A common boundary condition for fields of aeolian dune topography is growth from multidirectional wind regime, or annual cycle of wind. The surface evolution equation developed by Jerolmack and Mohrig (2005) is therefore adapted to accept transport in any azimuthal direction. Conservation of sediment between neighboring cells is accomplished by a finite volume method with quadrilateral cells. The magnitude of flux is computed for each cell centered node, and then decomposed into cell wall-orthogonal components for exchange with neighboring cells. In all model runs the mean transport directions is made to be as parallel to a grid direction as possible. This practice helps to minimize numerical dispersion. Sediment flux between elements is always computed by an explicitly approximated in time first order upwind scheme within the frame of reference of the transport direction, θ_k . The subscript 'k' refers to the k^{th} time step during model execution. If a transport direction is parallel to a grid axis, sediment flux along the orthogonal direction is set equal to zero. Otherwise, the indices, i and j , of the

upwind (subscript ‘u’) or downwind (subscript ‘d’) neighbor nodes are given by the following (Eqs. 4.1-4.4):

$$i_d = i + \text{sign}(\cos(\theta_k)) \quad (4.1)$$

$$i_u = i + \text{sign}(\sin(\theta_k)) \quad (4.2)$$

$$j_d = j + \text{sign}(\sin(\theta_k)) \quad (4.3)$$

$$j_u = j + \text{sign}(\cos(\theta_k)) \quad (4.4)$$

Orthogonal components of basal (boundary) shear stress, τ_x, τ_y are computed for each node as a series expansion of topography (Jerolmack and Mohrig, 2005) (Eqs. 4.5 and 4.6). The practice of expressing basal shear stress as a function of topographic height is deeply rooted in early studies of fluid motion over bedform topography (Exner, 1925). However, shear stress is found to scale with the aspect ratio of bedforms $\tau \propto h/\lambda$ where h and λ are the crest height and wavelength of a bedform (Jackson and Hunt, 1975; Kroy et al., 2002). Therefore, any increase in height or mean slope, will create a proportional increase in shear stress over the stoss slope of the bedform. This fundamental behavior of shear stress increasing with flow blockage and shoaling are described by shape parameters A and B (Jerolmack and Mohrig, 2005) in Equations 4.5 and 4.6. Equations 4.5 and 4.6 reproduce the along stoss slope trend in shear stress derived from sediment flux over a stoss slope of an aeolian dune observed by Lancaster et al. (1996).

$$\tau_{x_{i,j}} = \tau_A \cos \theta_k \left(1 + A\eta_{i,j} + B \left(\frac{\eta_{i,j} - \eta_{i_d j}}{dx} \right) \right) \quad (4.5)$$

$$\tau_{y_{i,j}} = \tau_A \sin \theta_k \left(1 + A\eta_{i,j} + B \left(\frac{\eta_{i,j} - \eta_{i_d j}}{dx} \right) \right) \quad (4.6)$$

Any nodes with shear stress less than a threshold value, τ_c , are set to zero (Eqs. 4.7,4.8). This practice acts to represent a lee shadow zone (Jerolmack and Mohrig, 2005), as nodes along a lee slope are always computed to be negative. Stochastic runs set τ_c to be random over the

computational domain. This allows portions of the bed to be preferentially mobile and immobile, crudely mimicking wind gustiness ubiquitous in aeolian environments. The consequence of including a spatially variable threshold for sediment motion is nearly identical to the addition of a stochastic sediment flux term considered by Jerolmack and Mohrig (2005). Without the addition of threshold of motion noise, a single wavelength of bedform topography is evolved. Adding the stochastic threshold of motion creates new perturbations, and spawns superimposed bedforms on stoss slopes.

$$\tau_{x_{i,j}} = \begin{cases} \tau_{x_{i,j}}; \tau_{x_{i,j}} > \tau_c \\ 0; \tau_{x_{i,j}} \leq \tau_c \end{cases} \quad (4.7)$$

$$\tau_{y_{i,j}} = \begin{cases} \tau_{y_{i,j}}; \tau_{y_{i,j}} > \tau_c \\ 0; \tau_{y_{i,j}} \leq \tau_c \end{cases} \quad (4.8)$$

Closely following the bedform modeling practices of Jerolmack and Mohrig (2005) , Hersen (2004), and Diniega (2010) lee slopes relax via an down-wind calculated expression of sediment diffusion where lee surfaces have exceeded an enforced angle of repose, θ_c (Eqs. 4.9 and 4.10). Provided that the avalanching coefficient E is large, the slope relaxes via an “avalanching sediment flux”, $q_{ax_{i,j}}$, $q_{ay_{i,j}}$, to an angle of repose in a single time step (Diniega, 2010; Jerolmack and Mohrig, 2005). The down-wind nodes are chosen based on the transport direction, θ_k .

$$q_{ax_{i,j}} = \begin{cases} E \left(\left(\frac{\eta_{i,j} - \eta_{i_wj}}{\Delta x} \right)^2 - \tan^2 \theta_c \right) \left(\frac{\eta_{i,j} - \eta_{i_wj}}{\Delta x} \right) ; \text{atan} \left(\frac{\eta_{i,j} - \eta_{i_wj}}{\Delta x} \right) \geq \theta_c \\ 0 ; \text{atan} \left(\frac{\eta_{i,j} - \eta_{i_wj}}{\Delta x} \right) < \theta_c \end{cases} \quad (4.9)$$

$$q_{ay_{i,j}} = \begin{cases} E \left(\left(\frac{\eta_{i,j} - \eta_{i_ju}}{\Delta x} \right)^2 - \tan^2 \theta_c \right) \left(\frac{\eta_{i,j} - \eta_{i_ju}}{\Delta x} \right) ; \text{atan} \left(\frac{\eta_{i,j} - \eta_{i_ju}}{\Delta x} \right) \geq \theta_c \\ 0 ; \text{atan} \left(\frac{\eta_{i,j} - \eta_{i_ju}}{\Delta x} \right) < \theta_c \end{cases} \quad (4.10)$$

The magnitude of all sediment fluxes, $q_{i,j}$ is then computed for each node (Eq. 4.11).

Sediment flux at each node is computed using the local values of shear stress. The sediment flux – boundary shear stress relationship of Meyer-Peter and Müller (1948) with coefficients $m = 1$, and $n = 3/2$ is chosen (Jerolmack and Mohrig, 2005). The power law relationship is chosen as it is nearly the same as the ballistic formula of Bagnold (1941) and approximates saturated sediment flux over aeolian dune topography (Kroy et al., 2002).

$$q_{i,j} = \sqrt{\left(m\tau_{x_{i,j}}^n + q_{a_{x_{i,j}}}\right)^2 + \left(m\tau_{y_{i,j}}^n + q_{a_{y_{i,j}}}\right)^2} \quad (4.11)$$

The sediment flux magnitude at each node is then decomposed into components $q_{x_{i,j}}$ and $q_{y_{i,j}}$ which are orthogonal to the cell walls. These components exchange sediment with the relevant cell neighbors, as determined by the current transport direction θ_k (Fig. 4.1) (Eqs. 4.12, 4.13):

$$q_{x_{i,j}} = q_{i,j} \cos \theta_k \quad (4.12)$$

$$q_{y_{i,j}} = q_{i,j} \sin \theta_k \quad (4.13)$$

Following the original surface evolution equation of Jerolmack and Mohrig (2005), the elevation change at each node is computed as a first order upwind difference (upwind nodes are selected based on the transport direction θ_k). Superimposed is a discrete Laplacian, which handles the lateral transfer of sediment and also enhances the overall numerical stability of the model (Jerolmack and Mohrig, 2005; Press et al., 1988).

$$\Delta\eta_{i,j} = \frac{-\Delta t}{(1-p)\Delta x} \left(q_{x_{i,j}} - q_{x_{i_d,j}} + q_{y_{i,j}} - q_{y_{i_d,j}} \right) + \frac{\Delta t D}{(\Delta x)^2} \left(\eta_{i+1,j} + \eta_{i,j+1} + \eta_{i-1,j} + \eta_{i,j-1} - 4\eta_{i,j} \right) \quad (4.14)$$

4.2.2 Grid and boundary conditions

The rectangular model domain is rimmed by boundary nodes (Fig. 4.1). If the user selects a fully periodic simulation, these boundary nodes join the computational domain as the boundary nodes are mapped to become the cell neighbor of the opposite side of the domain. This configuration of boundary nodes is used in cases 4.3.2 and 4.3.3. If chosen by the user, the boundary nodes may represent sediment source areas, where specified low amplitude, random fluctuations in topography occur each time step. The specified random topographic fluctuations allow small bedforms to grow and coalesce into larger bedforms down transport direction. This boundary node configuration is used in cases 4.3.4 and 4.3.5.

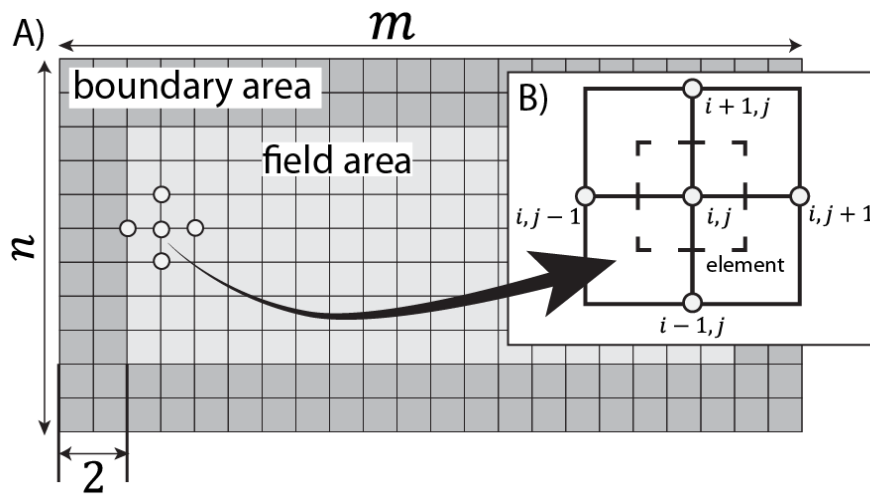


Figure 4.1: Diagram of model domain. A) Shaded areas are boundary nodes, which act as a source area, or as a no-flux boundary. Boundary nodes are field area nodes for periodic boundary conditions B) Diagram showing the finite cell volume and relative position of nodes.

4.2.3 Post-processing of aeolian surface model output

The aeolian surface model includes routines to post-process the model results into simple parameters of dune height, h , crest-to-crest bedform wavelength, λ , and the number of crest terminations within the model domain, ψ . Parameters h and λ are found by isolating peaks and troughs in one-dimensional transects of model topography that are oriented orthogonally to the bedform crests. Bedform height, h , is measured as the vertical distance between the peak and trough of a single bedform. Crest-to-crest wavelength is measured as the straight line distance. The number of terminations, ψ , is determined by first finding a logical mask of the dune surfaces above the mean elevation. This creates a binary image of the concave-downward portion of dune topography. The resulting binary image is skeletonized and cleaned by binary morphological operations. The endpoints and juncture points of the binary skeleton are identified and counted. This automated method of isolating and counting crest terminations was found to be consistent with eye measurements, but may not always match eye-measured termination counts. However, crest termination counting by this method is reproducible and exceedingly efficient.

For fully periodic simulations, h , λ and ψ are averaged over the entire model domain, and analyzed as functions of model time step. For simulations that grow dune topography from a sediment source, the model is first spun-up for $1e4 \Delta t$, to allow instabilities that originate near the sediment source to traverse the domain (Jerolmack and Mohrig, 2005). Afterward, h , λ and ψ are averaged through time, and analyzed as a function of distance away from the sediment source. The functions created for post-processing are highly modular and readily adaptable to include other metrics measured from either topographic peak and trough or binary image information. All model components are written in a highly readable computer language,

Matlab®, and are made freely available here (see supplementary files). Future work will develop the model in an open source computer language and include a graphical user interface.

4.3 APPLICATION

A comparison between model and real dune topography and four case studies of the growth of aeolian bedform topography from different boundary conditions are presented to gather support for the aeolian surface model. Two simulations are performed with a unimodal transport regime. Two additional simulations are performed with a bimodal transport regime with its modes separated by 160° . Each transport regime is applied to model dunes that grow with periodic boundary conditions and dunes that grow from a prescribed sediment source elevation. These model runs demonstrate the ability of the modified surface elevation equation to produce realistic, dynamic aeolian bedform topography. The final application is a comparison of the genetic history of model dunes growing through time, to those growing through space. This application demonstrates the exploratory value of research products generated by the aeolian surface model.

4.3.1 Model input for applied cases

In all model cases, the transport direction θ_k [°] ranges from 180° to -180° and is given by either a unimodal distribution made by random sampling of a normal distribution ($\mu = 0^\circ$ $\sigma = 15^\circ$), or a bimodal distribution made by alternating sampling from one of two normal distributions ($\mu = \pm 80^\circ$ $\sigma = 20^\circ$). The bimodal transport regime alternates between these two distributions every $20 \Delta t$. The time series of transport directions θ_k contains an entry for each time step of model execution. Gross bedform-normal transport analysis predicts alignment of the

crest-line trend to the transport regime (Rubin and Hunter, 1987). In its most concise form, the gross bedform-normal model predicts the compass direction of the crest-line trend based on the compass direction having the greatest sediment flux. The crest-line trend is therefore perpendicular to the magnitude-weighted mean direction of the transport regime (du Pont et al., 2014). This method is here applied to the bimodal and unimodal transport regime to predict the crest trend alignment for these model runs. Using only the wind regime data shows that for the unimodal transport regime, the crest trend should be perpendicular to the Northing axis. This crest trend gives a modes of dip directions of 0° and $\pm 180^\circ$ (Rubin and Hunter, 1987). Applying the method of Rubin and Hunter (1987) to the bimodal transport regime predicts that the crest trend will parallel the Northing axis. This crest trend for the bimodal transport regime gives modes of dip directions of $\pm 90^\circ$.

For all cases, the chosen grid is a uniformly spaced with 101×201 nodes. Simulations are run for a sufficient number of time steps to ensure that bedform topography is adequately sampled. Cases with periodic boundaries are run for $2e4 \Delta t$ for the unimodal transport regime, and $3e4 \Delta t$ for the bimodal transport regime. Topography is sampled every $50\Delta t$ from the the initial condition to the final time step. Because of the spontaneous growth of new bedform topography from the node down-transport of an existing bedform (Jerolmack and Mohrig, 2005), all model simulations with a sediment source area must be run until bedforms originally sourced from the supply area have traversed the entire domain. This practice ensures that only bedforms originating from the source area are considered for analysis. To accomplish this task, the model is spun-up for $10^4 \Delta t$ before any topography is recorded. Afterward, topography is sampled every $50 \Delta t$, and the model is run to $10^5 \Delta t$ time steps.

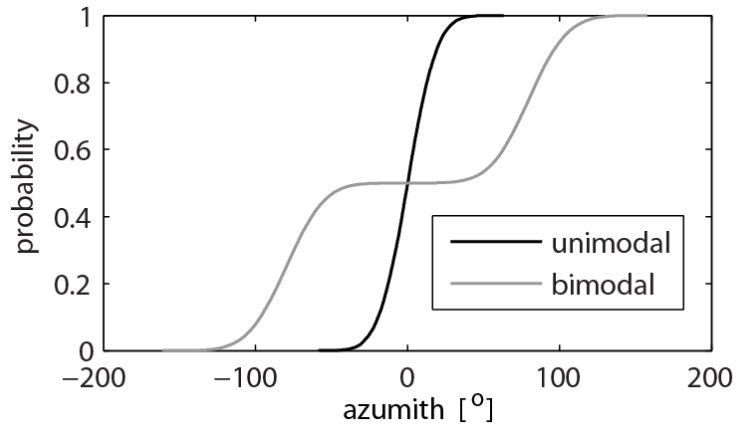


Figure 4.2: Transport direction ECDFs. Empirical cumulative distribution functions for the sets of transport event directions, θ_k used in unimodal and bimodal transport regimes for model cases.

Parameter	Value
A	0.1
B	3
m	1
n	1.5
E_0	20
D	0.08
p	0.4
θ_c	32°
τ_a	0.3
τ_c	3*rand
Δt	0.7
$\Delta x, \Delta y$	10

Table 4.1: Model parameters for all runs. Because the model is not calibrated, unless specified, the units of model parameters are arbitrary.

4.3.2 Model comparison to natural aeolian dune topography

The root mean square of surface elevation can be used to compare how model topography (Fig. 4.3a) and natural topography (Figure 4.3b) accrue roughness through space (Barabási, 1995). Following Jerolmack and Mohrig (2005), the root mean square width of modeled topography is compared to the root mean square of natural dune topography calculated for a growing window. For this, we use the topography modeled from the scenario in Section 4.3.3 that has transverse dunes growing from a unimodal transport regime (Fig. 4.3a). These simulation results are similar to the center of White Sands dune field, NM, USA (Fig. 4.3b), which contains crescentic dunes that maintain a transverse orientation to a nearly unimodal wind regime (Eastwood et al., 2012; Jerolmack et al., 2012).

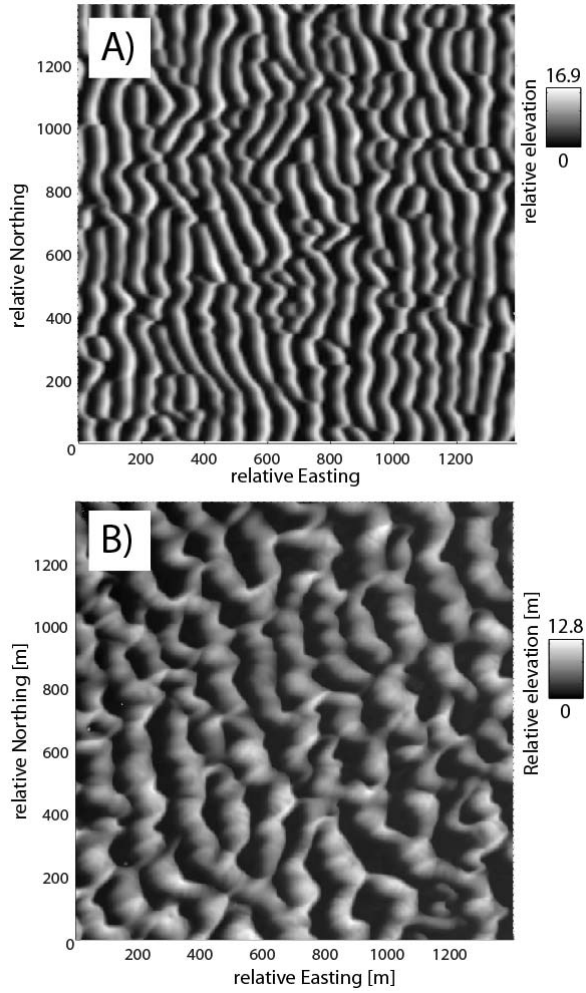


Figure 4.3: DEMs of modeled and natural aeolian bedforms. A) gray scale elevation map of model bedform elevation B) Gray scale elevation map of natural gypsum sand dune field elevation from White Sands NM, N.M.

The interface width, w , for the natural dune topography calculated as $w = \left(\frac{1}{N} \sum_{i=1}^N (\eta_i - \bar{\eta})^2 \right)^{1/2}$ over a systematically increasing window size, l_w . The result is summarized in Figure 4.4a and exhibits both a scaling regime and a saturation regime for w . The rollover point where the scaling regime gives way to saturation is labeled l_w^* in Figure 4.4a. In the scaling regime, the data are well described by a power law relationship, $w \sim l_w^\alpha$, where α is the slope of the solid line plotted in Figure 4.4a (Jerolmack and Mohrig, 2005). Jerolmack and Mohrig (2005) report

$\alpha = 0.64$ for natural fluvial bedform topography; whereas we find $\alpha = 0.91$ for the section of natural dune topography imaged in the LiDAR derived DEM of the White Sands dune field (Fig. 4.3b). In order to compare the model and natural interface width, both are scaled by their values for w^* , the interface width at the rollover point defining saturation. In turn, the window sizes are scaled by respective values of l_w^* . Plotting the scaled interface width, $\frac{w}{w^*}$, as a function of scaled window size, $\frac{l_w}{l_w^*}$, reveals that both the aeolian surface model and natural dune topography abide by the same scaling to saturation relationship (Fig. 4.4b). This comparison between modeled and natural topography establishes reasonable support for a surface model of aeolian bedform to represent the range of interface width found in natural aeolian dune topography but does not calibrate the model to data.

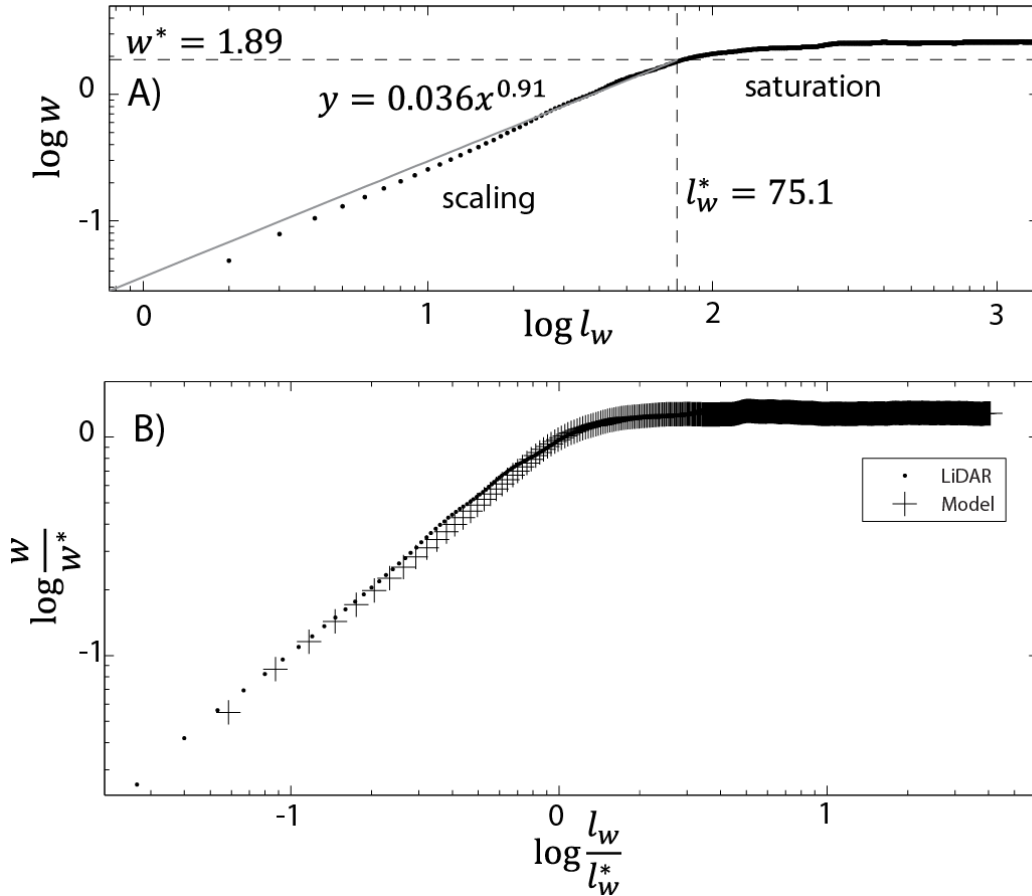


Figure 4.4: Roughness of modeled and natural dune topography. A) Root mean square interface width w as a function of window length l_w of natural dune topography imaged by LiDAR survey of White Sands Gypsum dune field, New Mexico. B) Scaled comparison of model topography and observed natural dune topography, both growing from a line sediment source area. This figure is modified from Jerolmack and Mohrig (2005).

4.3.3 Unimodal transport regime with fully periodic boundaries

The simulation is started from an initial condition of low amplitude uniformly distributed noisy topography. From this initial condition, small bedforms quickly grow and coalesce into larger forms (Figs. 4.5a, b); qualitatively similar to observations of coastal dune growth presented by Kocurek et al. (1992). At very early simulation time, sediment coalesces into small patches. As the small patches grow in height and wavelength, an asymmetry develops as stoss

slopes lengthen and pile sediment onto steeper, shorter lee slopes. During this phase, bedform crest height, $h(t)$, and wavelength, $\lambda(t)$, quickly increase (Figure 4.6a). The rapid increase and roll-over to saturation is well approximated by an exponential growth – saturation model, $a(1 - e^{-bt})$ (Baas, 1994). The fitted exponential growth – saturation models are plotted as dashed and solid lines in Figure 4.5a, and all fitted parameters are detailed in Appendix A. As $h(t)$ and $\lambda(t)$ increase, the number of crest terminations within the computational domain, $\psi(t)$, quickly decreases, then transitions to a second, much slower rate of decrease. This behavior is similarly observed in other bedform models (Werner, 1995). The number of crest terminations per time step $\psi(t)$ is very well approximated by a two-term exponential model, $a_1e^{-b_1t} + a_2e^{-b_2t}$ (fitted line, Fig. 4.6b). All models are fit using a nonlinear least squares routine, and all fit values and goodness of fit information are included in Appendix A. Eventually, very few terminations remain within the modeling domain (Figs. 4.5b and 4.6c).

As bedforms grow in height and wavelength they also grow longer in crest length as evidenced by fewer crest terminations. Throughout bedform growth the distribution of dip slopes decreases in variance and establishes two modes (Fig. 4.6c). These modes represent the well-organized lee and stoss slopes with modal dip directions of 0° and $\pm 180^\circ$, respectively. Similar changes in are observed in the first and second moments of dip direction during the growth of an oblique dune field from an initially flat sandy bed (Ping et al., 2014).

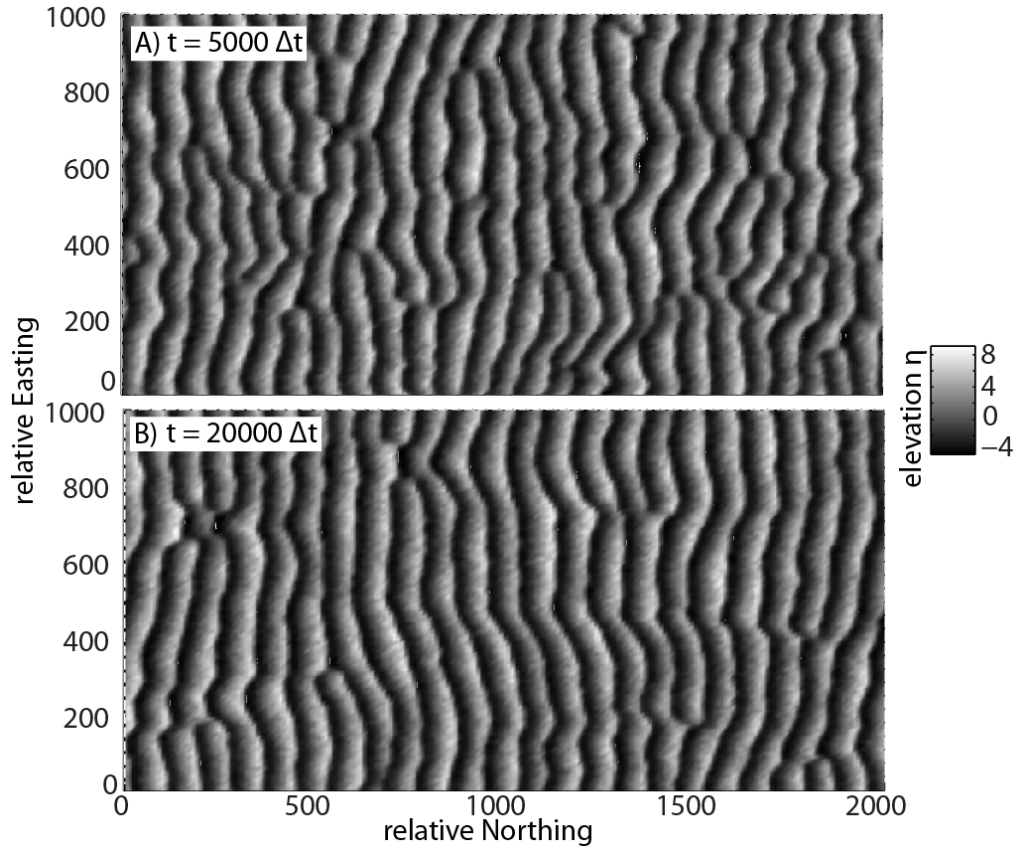


Figure 4.5: Unimodal aeolian bedform topography. A) Early time step of modeled bedform topography with fully periodic boundary conditions driven using a unimodal transport regime. B) End of simulation topography.

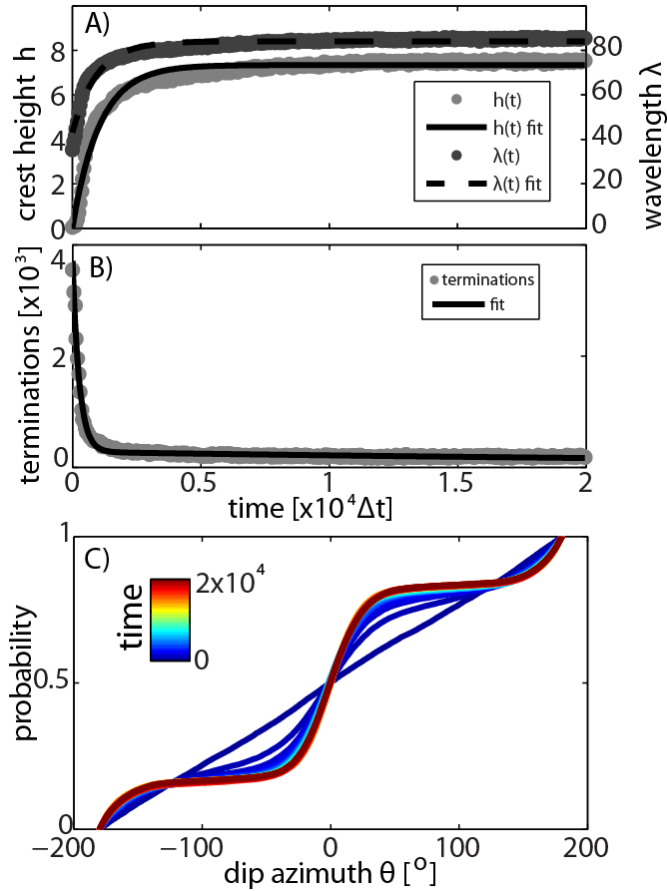


Figure 4.6: Unimodal bedform metrics as a function of time. A) Crest height, $h(t)$ and wavelength $\lambda(t)$ with fitted models B) Number of terminations present in computational domain $\psi(t)$ with fitted model C) Empirical CDF of dip direction color mapped by simulation time.

4.3.4 Bimodal transport regime with fully periodic boundaries

Applying a bimodal transport regime to the otherwise unaltered modeling scenario radically changes the morphology of the emergent topography (Figs. 4.7a, b). Starting from the same initial condition of low amplitude random topography, linear dunes emerge, interact, and merge to form larger dunes. During a single “seasonal” wind ($20 \Delta t$), an asymmetry between stoss and lee slopes develops as the stoss slope increases in length, and the lee slope shortens and steepens. The asymmetry developed from the previous “seasonal” wind is typically reversed by

the next “seasonal” wind. Interactions between dunes occur at distinct tuning fork junctures and by lateral linking, similar to natural linear dune fields. Through time, smaller, more sinuous bedforms (Fig. 4.7a) coalesce to become larger, straighter crested bedforms (Figure 4.7b). Despite distinct changes in bed morphology and growth rates, altering the transport regime does not change the functional form of $h(t)$, $\lambda(t)$ or $\psi(t)$, as all are well described by the same fitted models characterizing the unimodal case (Fig. 4.6a, b). However, the rate at which the topography achieves saturated values of $h(t)$ and $\lambda(t)$ is visibly different (compare Figs. 4.7a, b and 4.5a, b). During the simulation the distribution of dip directions decreases in variance, and becomes tightly distributed about two modes of $\pm 90^\circ$ (Fig. 4.8c).

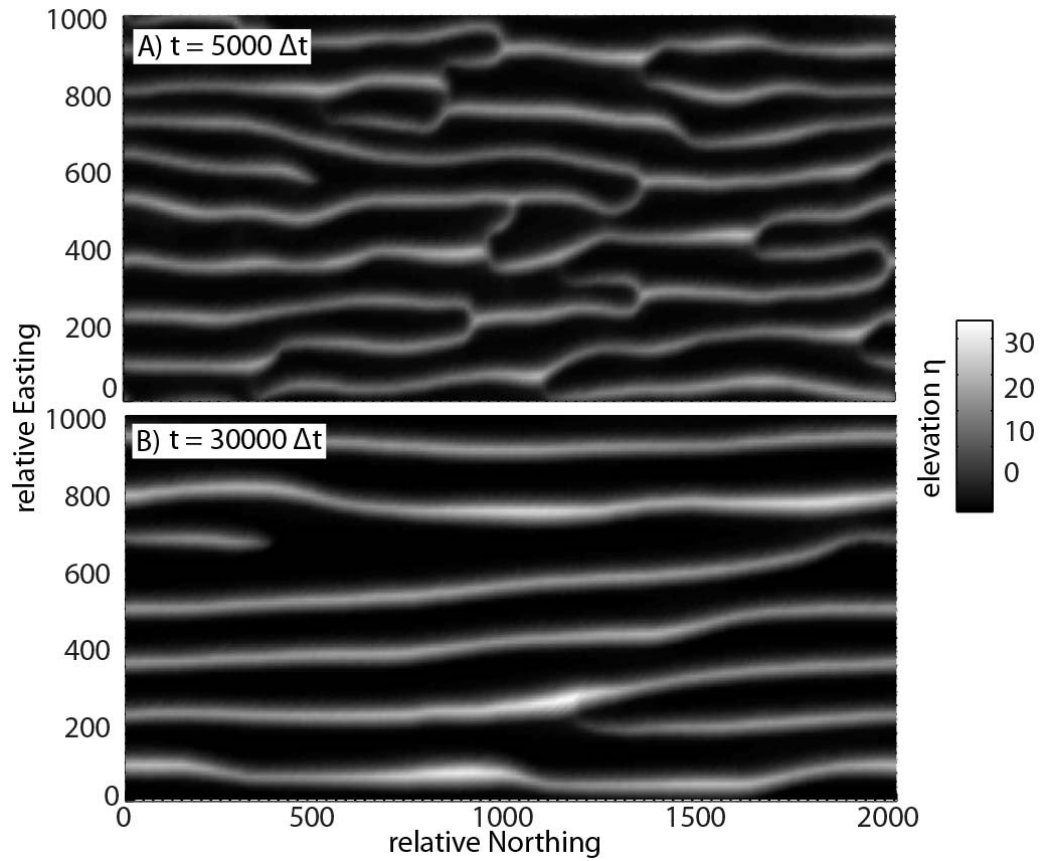


Figure 4.7: Bimodal aeolian bedform topography. A) Early time step of modeled bedform topography with fully periodic boundary conditions and bimodal transport regime. B) End of simulation topography.

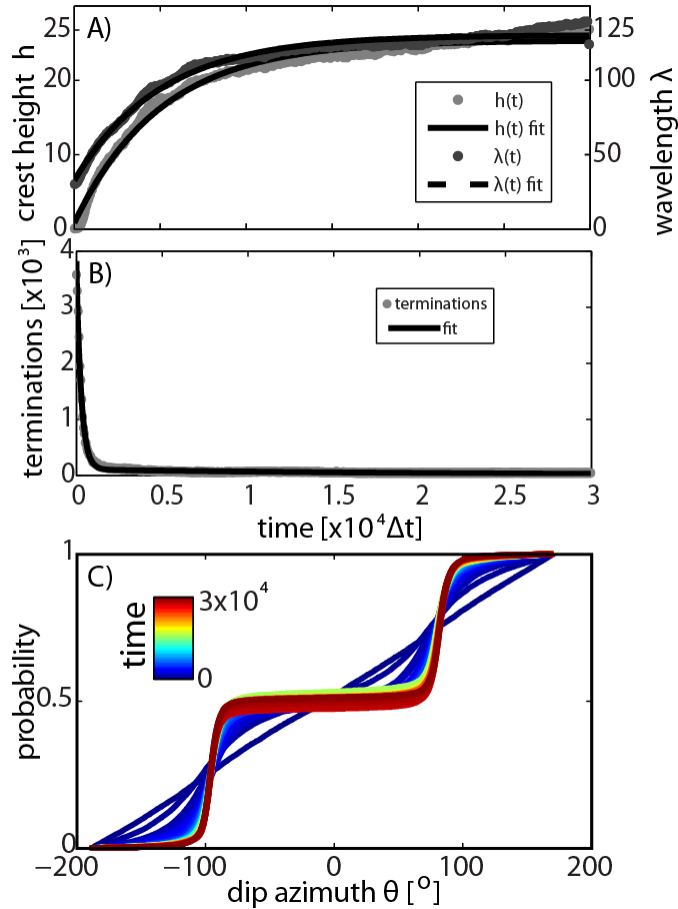


Figure 4.8: Bimodal bedform metrics as a function of time. A) Crest height, $h(t)$ and wavelength $\lambda(t)$ with fitted models B) Number of terminations present in computational domain $\psi(t)$ with fitted model C) Empirical CDF of dip direction color mapped by simulation time.

4.3.5 Unimodal transport from a line source area

The fully periodic boundary conditions of case 4.3.3 are changed to represent dunes growing from a sediment source area (right side, Fig. 4.9) driven by the same unimodal transport regime. The top and bottom sides of the domain do not allow sediment flux to cross. The second order term in Equation 4.8 and 4.9 cause instabilities to grow from the nodes down-transport direction of the lee surface of existing bedforms (Jerolmack and Mohrig, 2005). Therefore, the surface model is spun up for $1e4 \Delta t$ to ensure all bedforms within the domain have originated

from the source area and not from the interior of the domain. Changing the boundary conditions on the model domain radically changes the topography produced by the aeolian surface model. Small perturbations rapidly grow in height $h(x)$ and wavelength $\lambda(x)$ as a function of down-wind distance, x , from the sediment source area (Figs.4.6a, b). The simulation produces realistic looking dune topography of non-uniform height, wavelength and spacing, and with migration rates that vary through time (Fig. 4.9). However, the uniformity in all of these dune parameters increases dramatically with distance away from the sediment source area. Intriguingly, the time-averaged values of $h(x)$ and $\lambda(x)$ are well described by the same exponential growth to saturation equation used to model time changes in h and λ for fully periodic boundary conditions (Fig. 4.10a) and as dunes move away from the source area, their growth and coalescence drives a reduction in the number of crest terminations, $\psi(x)$ (Fig. 4.10b). Again, this reduction is well described by the same two-term exponential function used to describe the time change of crest terminations for the model cases with fully periodic boundary conditions. Because topography is not periodic, partial dunes are captured while exiting the domain by the post-processing routines. These boundary influenced regions are shaded light gray in Figure 4.10a and 4.10b. The dip direction of bedform topography is averaged for over the domain for each time step and plotted as an empirical cumulative distribution function (Fig. 4.10c). Despite the large changes in crest height and wavelength with space, the distribution of dip direction is nearly invariant in time (Fig. 4.10c). The distribution of bedform surface dip directions has two models, 0° and $\pm 180^\circ$ corresponding to lee and stoss slopes, respectively.

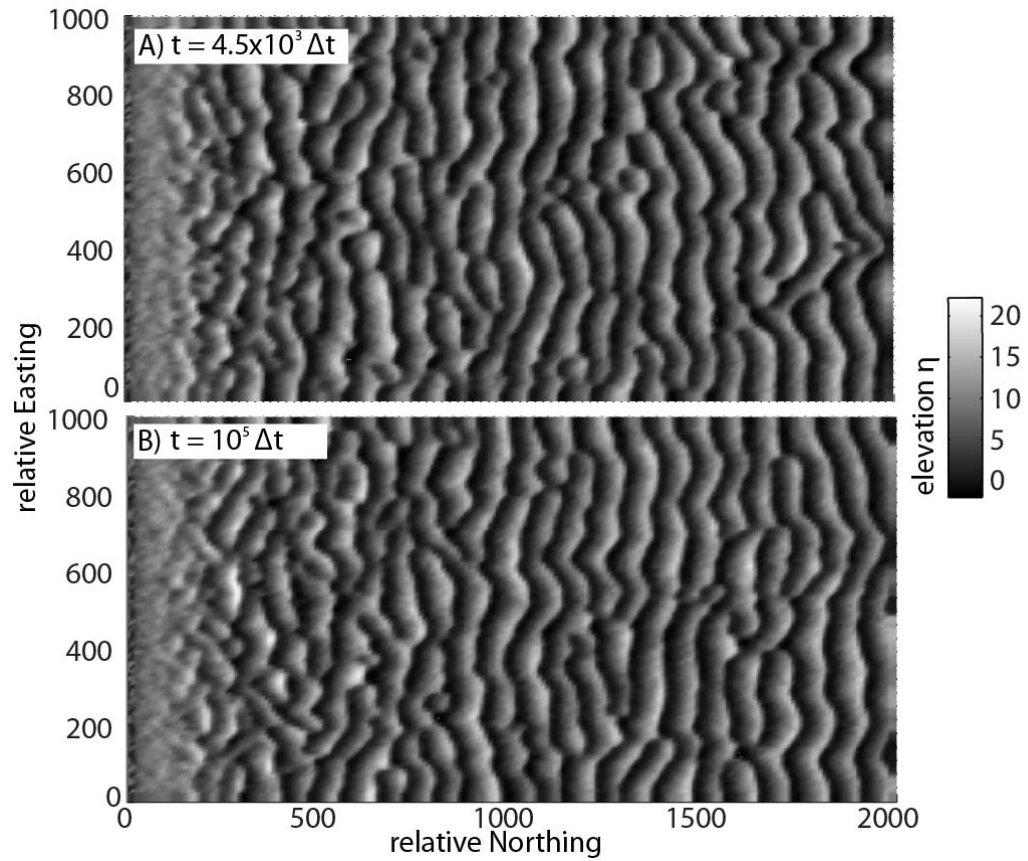


Figure 4.9: Unimodal aeolian bedform topography. A) Middle of simulation time step of modeled bedform topography with a sediment source area (left) no-flux (top and bottom) and an outlet (right) driven using a unimodal transport regime. B) End of simulation topography.

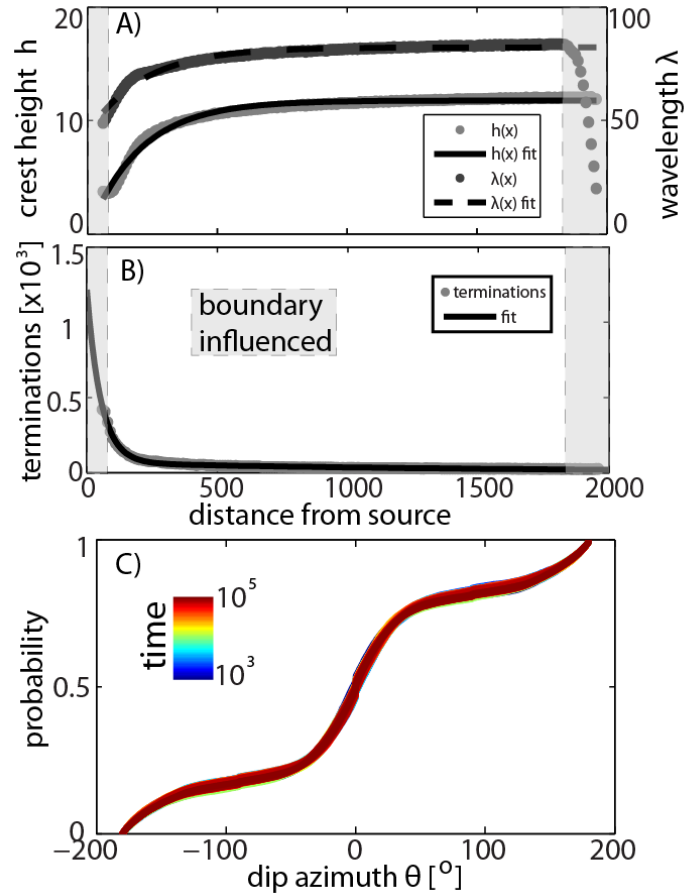


Figure 4.10: Unimodal bedform metrics as a function of space. A) Crest height, $h(x)$ and wavelength $\lambda(x)$ are plotted as a function of distance from the sediment source area. B) Number of terminations present in computational domain $\psi(x)$ with fitted model. C) Empirical CDF of dip direction color mapped by simulation time.

4.3.6 Bimodal transport from a line source area

The fully periodic boundary conditions of case 4.3.4 are changed to represent dunes growing from a sediment source area (right side, Fig. 4.11) driven by the bimodal transport regime. The top and bottom sides of the domain are handled as no-flux boundaries. Similar to the previous case, the surface model is spun up for $1e4 \Delta t$ to ensure all bedforms within the domain have originated from the source area, not from the interior of the domain. Again, changing the

boundary conditions on the model domain radically changes the resulting bedform topography. In stark contrast to the growth of transverse bedforms from a sediment source (case 4.3.5), the bimodal transport regime very quickly works sediment near the source area (Easting axis, Fig. 4.11) into small bedforms. The small dunes then coalesce into long linear bedforms of very low sinuosity and almost constant wavelength (Figs. 4.11a, b). The small bedforms close to the sediment source area do change position and crest length with time, but at a rate much slower than the unimodal case. During each “seasonal” wind of $20\Delta t$ an asymmetry between lee and stoss slopes develops. Typically the asymmetry between opposing bedform slopes is partially reversed during the next “seasonal” wind. Despite the apparent uniformity of model topography, defects and interactions are still present, and move through the domain (Figs. 4.11a, b). Because of the sparse nature of defects and interactions in this case an extremely long simulation time ($10^5 \Delta t$) is required to adequately capture the variation of defect density, crest height, and wavelength as a function of distance from the sediment supply area.

Measured quantities of bedform topography again demonstrate the same functional behavior with distance away from the sediment supply area (Easting axis, Fig. 4.11). Height, $h(x)$, and wavelength, $\lambda(x)$, grow exponentially and saturate to a steady value (Figs. 4.12a, b). Similar to case 4.3.5, topography is not spatially periodic therefore partial bedforms are caught exiting the domain by the post-processing routing. These boundary influenced regions are shaded light gray in Figure 4.12a and 4.12b. The distribution of dip azimuth through time is steady, but not as steady as case 4.3.5 (Figs. 4.10c and 4.12c). The lack of steadiness is due to the “seasonal” reversals of bedform asymmetry. During a single wind, one mode grows slightly larger in population due to an increase in slope surface area. The empirical cumulative distribution

functions of dip azimuth show two modes, $\pm 90^\circ$, corresponding to the stoss and lee slopes of the linear bedforms.

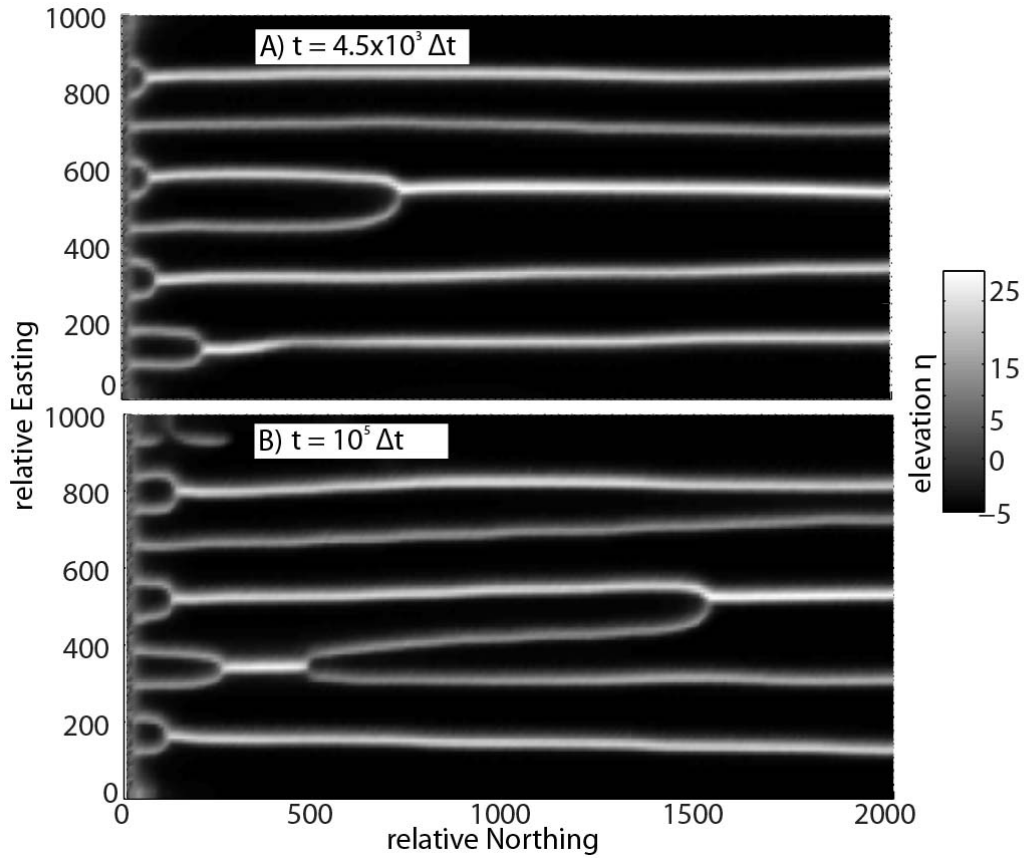


Figure 4.11: Bimodal aeolian bedform topography. A) Middle of simulation time step of modeled bedform topography with a sediment source area (left) no-flux (top and bottom) and an outlet (right) driven using a bimodal transport regime. B) End of simulation bedform topography.

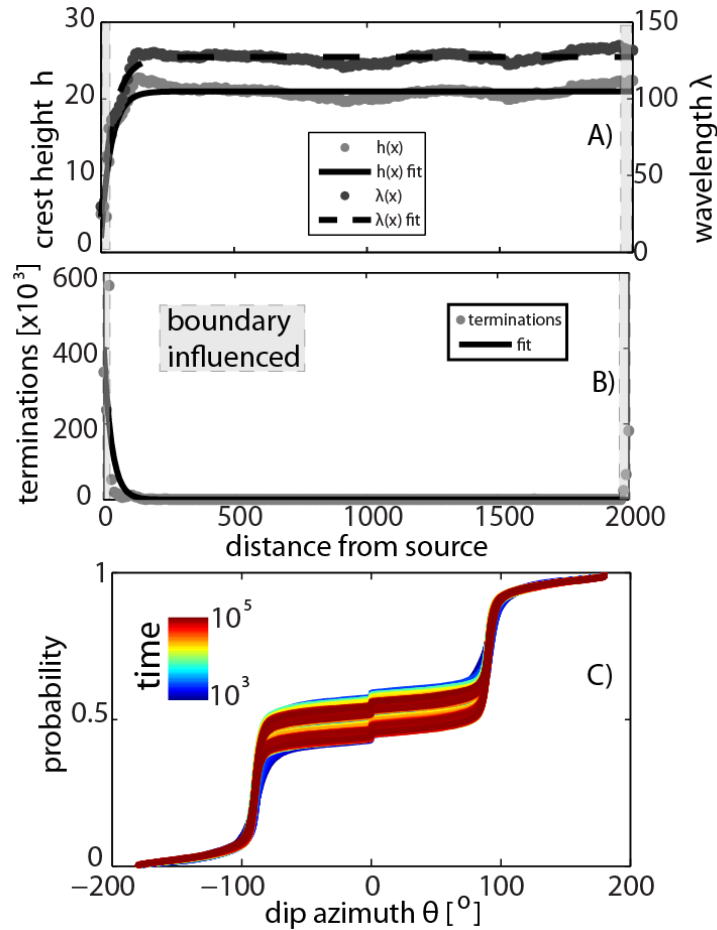


Figure 4.12: Bimodal bedform metrics as a function of space. A) Crest height, $h(x)$ and wavelength $\lambda(x)$ are plotted as a function of distance from the sediment source area. B) Number of terminations present in computational domain $\psi(x)$ with fitted model C) Empirical CDF of dip direction color mapped by simulation time.

4.3.7 Relative geomorphic aging

The last application demonstrates a simple exploratory research task: How quickly do bedforms reach an equilibrium size as a function of distance from a sediment source? How does this compare to bedform growth with time when bedforms are effectively disconnected from a sediment source?

To compare bedform growth driven by unimodal and bimodal wind regimes, as well as growth connected to either periodic or specified sediment elevation boundary conditions, it is useful to define an equilibrium timescale for specified periodic boundary conditions and an equilibrium length scale for specified sediment elevation boundary conditions. We adopt the convention of Baas (1994) and define equilibrium as being achieved when the value of $h(\xi)$ or $\lambda(\xi)$ reaches 99% of the fitted long-time coefficient a , in the exponential growth-saturation equation $a(1 - e^{-b\xi})$. $\xi = t$ for fully periodic runs, and $\xi = x$ for a bedform grown from a sediment source area. All fitted coefficients from all runs are listed in Appendix A and their calculated equilibrium scales are listed in Table 2.

Unimodal transport regimes achieve equilibrium in the least amount of computational time steps ($\sim 4500 \Delta t$) in fully periodic domains, while bimodal transport regimes achieve equilibrium with the shortest distance from the sediment source area ($\sim 22 \Delta x$). The equilibrium time t_e and equilibrium distance x_e for a single transport regime and parameter (h or λ) are compared to find a simple rate $v_e = \frac{x_e}{t_e}$, at which bedforms “age” in space compared to time (Table 4.2). The smaller the value of v_e , the quicker bedforms “age” as a function of distance away from a sediment source, for a given transport regime. Unimodal transport ages bedforms most slowly as a function of distance from the source area, while linear bedforms “age” much faster as a function of distance from the sediment source. Therefore, relative ages of aeolian dunes grown from a sediment source area may have a morphologic dependence. This result provides an interesting and testable hypothesis for ongoing studies in aeolian dune pattern analysis (Ewing et al., 2006a).

$h_e(\xi)$		$\lambda_e(\xi)$	
unimodal	bimodal	unimodal	bimodal
$t_e \cong 4589 \Delta t$	$t_e \cong 23235 \Delta t$	$t_e \cong 4412 \Delta t$	$t_e \cong 23149 \Delta t$
$x_e \cong 93.7 \Delta x$	$x_e \cong 18.2 \Delta x$	$x_e \cong 69.8 \Delta x$	$x_e \cong 25.5 \Delta x$
$v_e = 0.0204 [lt^{-1}]$	$v_e = 7.8330 e - 4 [lt^{-1}]$	$v_e = 0.0158 [lt^{-1}]$	$v_e = 0.0011 [lt^{-1}]$

Table 4.2: Comparison of geomorphic “aging”. Equilibrium scales for $h(\xi)$ and $\lambda(\xi)$, and a relative rate to equilibrium v_e , for all model runs.

4.4 CONCLUSIONS

The aeolian bedform surface model presented here is a compromise between realism and model complexity. While recent advances in modeling coupled fluid and granular motion have reproduced the behavior of bedforms within benchmark flume experiments (Khosronejad and Sotiropoulos, 2014), simple models are arguably useful as a computationally inexpensive tool for exploratory research (Jerolmack and Mohrig, 2005). The surface model output should be suitably robust as to describe the temporal and spatial evolution of aeolian topography driven by transport regime. Although the model is not explicitly calibrated to data, the behavior of model bedform topography reproduces the functional form of bedforms as measured in the field and flume.

Although the surface model is only applied to four cases, more cases are available to run in the supplied source code. All model simulations are executed by running the script “main.m”. If desired, the model can be compiled using Matlab’s built-in compiler, and executed without a Matlab license by installing the Matlab Runtime on the target computer. The post-processing routines places the complex output into easily analyzed values of dune height, wavelength, dip direction and number of crest line terminations that are in turn ready for use in creating of new and intriguing exploratory research products.

4.5 ACKNOWLEDGEMENTS:

Caroline Hern provided continuous feedback and conceptual steering and support for this project. We deeply thank Mauricio Perillo, Man Liang and Matthew Wolinski for helpful conversation, guidance and suggestions concerning code development. Funding for this work was provided by the Royal Dutch Shell Oil Company. This work does not reflect the views of the Royal Dutch Shell Oil Company.

Chapter 5: Self-organization, autogenic and allogenic signal preservation in aeolian cross-stratification

5.1 INTRODUCTION:

We apply a one-dimensional (1D) surface model for aeolian bedforms driven by temporally variable allogenic forcing to create two-dimensional sections (2D) of cross stratified deposits. Numerical models of natural systems are necessarily incomplete, yet direct observations of aeolian dune behavior capturing growth and motion driven by transient climate signals such as strengthening and weakening of a wind are extremely difficult. The numerical experiment presented in this work is promoted as an exploratory research product. As such, synthetic cross sections generated from forward models of bedforms are used to guide and develop reasonable and testable hypotheses of how self-organization, autogenic and allogenic signals may encode into the architecture of aeolian sedimentary deposits.

Reconstructing the aerodynamic conditions of ancient aeolian environments is useful to understanding past climates and climate variability. Wind regimes, or annual cycles of sediment transporting wind events, are an allogenic driver of bedform motion and sedimentation within dune fields. At shorter time scales, a steady wind regime has been shown to interact with the shape of aeolian bedforms to produce different stratification types such as wind ripples, grain flow and grain fall (Eastwood et al., 2012; Sweet and Kocurek, 1990; Sweet et al., 1988). Because individual events within a wind regime encode directly into recognizable stratification types, the shape and motion of individual dunes can be reconstructed from their preserved aeolian stratification (Eastwood et al., 2012). At much longer time scales, wind regimes are dune field boundary conditions (Kocurek et al., 2010). Can long-term allogenic variability,

expressed by temporally varying wind intensity be detected within sections of aeolian cross-stratification? We employ a numerical model that mimics the time and space evolution for trains of bedforms (Chapter 4) in order to elucidate the preservation of self-organization, autogenic and allogenic signals within 2D sections of synthetic aeolian stratigraphy. The numerical experiment suggests that early self-organization and growth of dunes is always eroded by later dune forms and therefore not preserved in the rock record.

5.2 METHODS:

5.2.1 Original 1D bedform surface model

The modeling framework presented by Jerolmack and Mohrig (2005) and expanded here in Chapter 4 describes the growth and deformation of a surface that is the interface between non-moving sediment below and the sediment transporting fluid above. A primary strength of this model is the realistic reproduction of bedform growth as demonstrated by realistic scaling of topographic roughness through space and time. The original surface evolution equation of Jerolmack and Mohrig (2005) arises from combining three components that describe bedform growth, deformation and motion as a morphodynamic feedback between dynamic bedform topography, η , boundary shear stress, τ_x and saturated sediment flux q_s . The feedback is formed by (1) casting q_x as a power law function of τ_x (Jerolmack and Mohrig, 2005; Meyer-Peter and Müller, 1948), (2) solving for τ_x as a function of η , and (3) calculating temporal change in η using spatial change in q_x . This system captures the spontaneous growth and migration of trains of bedforms as non-linear waves (Jerolmack and Mohrig, 2005). By using a

model that produces realistic bedform geometry and kinematics, we intend to generate and evaluate synthetic dune stratigraphy arising from chosen boundary conditions and forcing.

5.2.2 1D bedform stratification model

The original surface evolution equation is adapted to create synthetic stratigraphy. We apply this surface model to examine cross-stratification arising from two allogenic signals: synchronized increases and decreases in sediment transport and aggradation rate. In this hypothetical scenario, boundary shear stress applied to bedform topography and aggradation rate are chosen to be in-phase, sinusoidal functions of time. This condition approximates enhanced sediment delivery to a basin due to a strengthened wind (Fig. 5.1). Such conditions are representative of dry aeolian systems where unlimited sediment is thought to be repetitively introduced to a sand sea due to waxing and waning wind strength (Fig. 5.1) (Kocurek, 1999). To complete the numerical experiment two “control” model simulations are performed that do not include variable aggradation or wind strength.

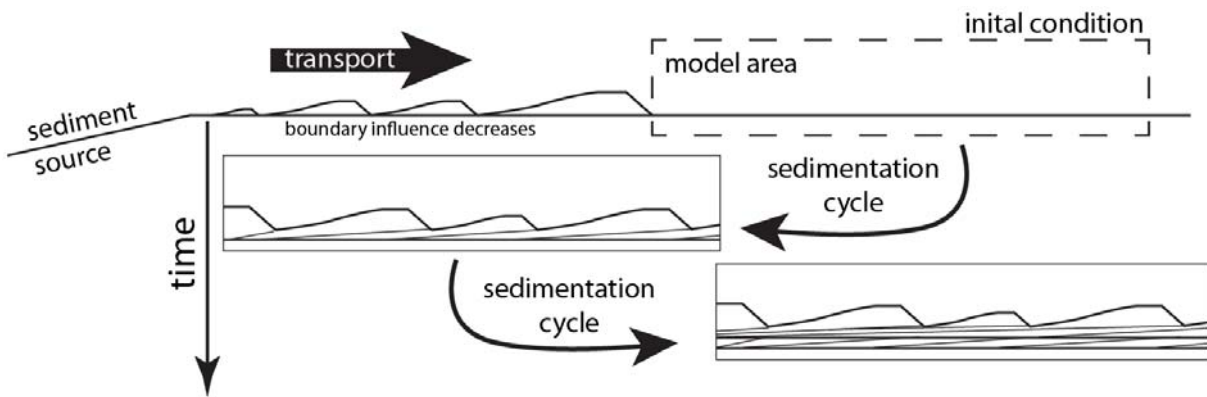


Figure 5.1: Conceptual hypothetical model scenario. The model area is imagined to represent a segment of an aeolian system (intra erg) away from the influence of a sediment source boundary condition. Synthetic aeolian stratigraphy is created by two sedimentation cycles.

The surface evolution equation is adapted to accept changes in mean elevation and ambient shear stress. Conservation of sediment between neighboring cells is accomplished by a finite volume method with node centered elements or cells (Fig. 5.2). The magnitude of flux is computed for each cell centered node, and then differenced for exchange with neighboring elements. The algorithm adopted to solve the bedform surface evolution equation in this study closely follows the original work of Jerolmack and Mohrig (2005).

At each time step boundary shear stress, τ_x , is computed for each node as a generic expansion of topography (Jerolmack and Mohrig, 2005) (Eq. 5.1). The practice of expressing boundary shear stress as a function of topographic height is deeply rooted in early studies of fluid motion over bedform topography (Exner, 1925). However, shear stress is also found to scale with the aspect ratio of bedforms, $\tau \propto h/\lambda$, where h and λ are the height and wavelength of a bedform (Jackson and Hunt, 1975; Kroy et al., 2002). Therefore, any increase in height or mean slope, will create a proportional increase in shear stress over the stoss slope of the bedform. This fundamental behavior of shear stress increasing with flow blockage and shoaling are described by shape parameters A and B , respectively (Jerolmack and Mohrig, 2005). A modification from Jerolmack and Mohrig (2005) removes the any allogenic influence from the blocking term in Equation 5.1 by placing the morphodynamic feedback in a moving reference frame. By subtracting $\eta_a = \sum_1^j r(j)$, the addition of sediment from sedimentation cycles does not modify the behavior of Equation 5.1. Without modification, adding sediment to the domain would globally increase the boundary shear stress. This modified shear stress – topography relationship qualitatively reproduces the along stoss slope trend in shear stress derived from sediment flux over a stoss slope of an aeolian dune observed by Lancaster et al. (1996).

$$\tau_{x_i} = \tau_A(j) \left(1 + A(\eta_i - \eta_a) + B \left(\frac{\eta_i - \eta_{i-1}}{dx} \right) \right) \quad (5.1)$$

Any nodes with shear stress, τ_{x_i} , less than zero are set to zero (Eq. 5.2). This practice crudely represents a lee shadow zone (Jerolmack and Mohrig, 2005), as nodes along a lee slope are always computed to be negative.

$$\tau_{x_i} = \begin{cases} \tau_{x_i}; \tau_{x_i} > 0 \\ 0; \tau_{x_i} \leq 0 \end{cases} \quad (5.2)$$

Closely following the practices of Jerolmack and Mohrig (2005), Hersen (2004), and Diniega (2010) lee slopes that exceed a threshold angle, $\theta_c = 34^\circ$, relax via an down-wind calculated diffusion (Eq 5.3). Provided that the avalanching coefficient E is large, the slope relaxes by an “avalanche flux”, q_{ax_i} , to an angle of repose in a single time step (Diniega, 2010; Jerolmack and Mohrig, 2005). Lee slopes that are below the threshold angle do not trigger the calculation of q_{ax_i} for their respective nodes (Eq. 5.3).

$$q_{ax_i} = \begin{cases} E \left(\left(\frac{\eta_i - \eta_{i+1}}{\Delta x} \right)^2 - \tan^2 \theta_c \right) \left(\frac{\eta_i - \eta_{i+1}}{\Delta x} \right) & ; \text{atan} \left(\frac{\eta_i - \eta_{i+1}}{\Delta x} \right) \geq \theta_c \\ 0 & ; \text{atan} \left(\frac{\eta_i - \eta_{i+1}}{\Delta x} \right) < \theta_c \end{cases} \quad (5.3)$$

The magnitude of all fluxes, q_{x_i} is then computed for each node (Eq. 5.4). Sediment flux at each node is computed using the local values of shear stress and the sediment flux – boundary shear stress relationship of Meyer-Peter and Müller (1948) with coefficients, $m = 1$ and $n = 3/2$ (Jerolmack and Mohrig, 2005). The chosen power law relationship is nearly the same as the ballistic formula of Bagnold (1941) and was chosen to model saturated sediment flux over bedform topography (Kroy et al., 2002).

$$q_{x_i} = m \tau_{x_i}^n + q_{ax_i} \quad (5.4)$$

The elevation change at each node, $\Delta \eta_i$, is computed as a first order upwind difference of sediment flux q_{x_i} , accounting for porosity, p (Eq. 5.5). a 1D discrete Laplacian with diffusivity,

D , is superimposed for enhanced numerical stability (Jerolmack and Mohrig, 2005; Press et al., 1988).

$$\Delta\eta_i = \frac{-\Delta t}{(1-p)\Delta x}(q_{x_i} - q_{x_{i-1}}) + \frac{\Delta t D}{(\Delta x)^2}(\eta_{i+1} + \eta_{i-1} - 2\eta_i) + r(j) \quad (5.5)$$

All six simulations used the same parameters listed in Table 5.1 and initial conditions. However, each simulation is driven using a different pair of allogenic signals, $\tau_A(t)$, and $r(t)$. Simulation 1 holds constantly at $\tau_A(j) = \tau_a = 0.3$ and has no bed aggradation, $r(j) = 0$ (Fig. 5.2). Simulations 2-5 modify the boundary shear stress term, $\tau_A(t)$, with a small sinusoidal variation (Eq. 5.6) with an amplitude equal to 5, 10, 15 and 20% of τ_a , respectively (Fig. 5.2a). Similarly, simulations 2-5 also include a sinusoidal variation in aggradation rate, $r(j)$ with an amplitude equal to 25, 50, 75 and 100% of $r_a = 2.5E - 5$, respectively. The allogenic signals used in simulations 2-5 have two full periods (sedimentation cycles, Figs. 5.1, 5.2), given by the frequency, $\varphi = \frac{2\pi}{1E5 \Delta t}$. Simulation 6 is conducted with a constant value of boundary shear stress $\tau_A(j) = \tau_a$, and a constant value of aggradation rate, $r(j) = r_a$.

$$\tau_A(j) = \tau_a(1 - \phi \sin(j\varphi)) \quad (5.6)$$

$$r(j) = r_a\psi \sin(j\varphi) \quad (5.7)$$

Parameter	Value
A	0.1
B	2
m	1
n	1.5
E	20
D	0.2
p	0.4
τ_a	0.3
r_a	$2.5E - 5$
Δt	0.5
Δx	10

Table 5.1: Values of parameters used in all simulations. Units are arbitrary.

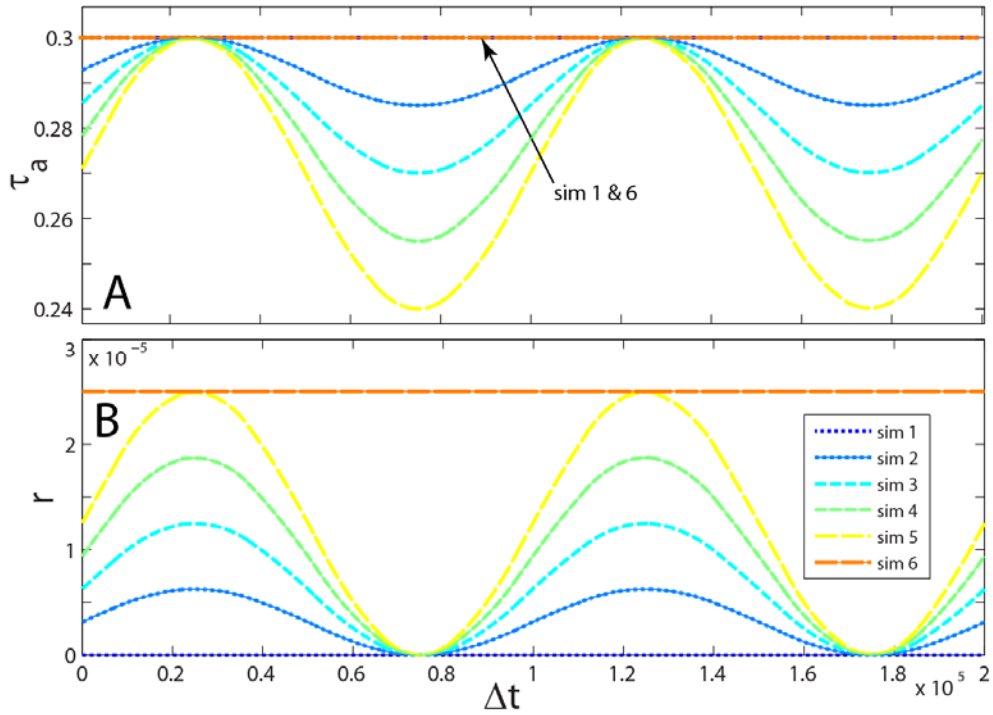


Figure 5.2: Allogenic signals imposed on bedform topography. A) Boundary shear stress $\tau_a(t)$ and B) aggradation rate $r(t)$ shown as a function of model time steps.

5.2.3 Grid and boundary conditions

The 1D model domain is composed of 501 node centered elements with constant width Δx (Fig. 5.3). The first and last nodes communicate with each other through an upwind finite difference stencil (gray nodes, Fig. 5.3), creating a periodic boundary condition. Execution of all simulations begins with an initial condition of uniformly distributed, very low amplitude random topography. Each simulation is run for a total of $2E5 \Delta t$. Each simulation (1-6) is performed 96 times using 96 independently generated initial conditions of low amplitude random topography. These 96 runs were checked to ensure that final results shown here are not dominated by the initial condition.

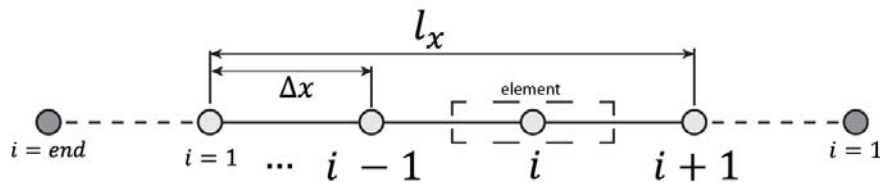


Figure 5.3: Model grid, element and boundary condition construction.

5.2.4 Post processing of model output: synthetic stratigraphy

The cumulative number of bedforms that have passed by each grid node (population = 501) are calculated by finding the peak elevations through the time series of elevation $\eta(x, t)$. Time steps of topography are used to create synthetic stratigraphy, which is color-mapped in Figures 5.5-5.10 by the time of deposition. The transformation from topography to stratigraphy is performed by systematically removing early surfaces that are cut by later ones (e.g., Strong and Paola (2008)). The result is an array of elevations where truncated topographic surfaces can produce bounding surfaces representing erosionally generated hiatuses in the depositional record.

For each pair of bounding surfaces found at each node, successive bounding surface elevations are differenced vertically to calculate a set thickness, l_{st} [L]. Any set with $l_{st} < 1E - 2$ [L] is not considered further as it is unlikely to recognize such a thin unit as an independent set of cross-strata in actual sedimentary deposits. All measurements of synthetic stratigraphy are constrained to events that occur after the creation of the first bounding surface. Interestingly, there is no stratigraphic record of the growth phase of bedforms from a roughened horizontal bed. This record is consistently removed during production of the first preserved bounding surface.

5.3 RESULTS:

5.3.1 Creation of synthetic cross-sections

All simulations show self-organization: early, rapid growth of mean bedform height (Fig. 5.4). Simulation 1 reproduces the anticipated response of exponential growth in bedform height up to the point of saturation (Baas, 1994) (Fig. 5.4a). Due to constant aggradation rate in Simulation 6, crest and trough elevations steadily increase (Fig. 5.4c). However, because of constant boundary shear stress, the mean bedform height in Simulation 6 reaches a steady, saturated value (Fig. 5.4a). Simulations 2 – 5 include sinusoidal variation in τ_A which drives sinusoidal variation in mean bedform height (Fig. 5.4a). The magnitude of the periodic fluctuation in bedform height is proportional to the amplitude of the allogenic driver (Fig. 5.2). Simulations 2 – 5 also include sinusoidal variation in aggradation rate, which appears in crest and trough elevations shown in Figure 5.4c. The values of mean bedform height shown in Figure 5.4a are calculated from mean bedform trough and crest elevations shown in Figure 5.4c. Notice

mean crest elevation fluctuations (upper curves, Fig. 5.4c) are slightly larger than fluctuation in trough elevation (lower curves, Fig. 5.4c). The extrema of bedform topography appear to be sensitive to the sinusoidal variations in the allogenic drivers. In stark contrast, trough-to-trough measured bedform wavelength, λ appears insensitive to the periodic fluctuations in τ_A (Fig. 5.4b) with the caveat that small fluctuations in λ are likely to be aliased, as the resolution of measuring λ is equal to the grid resolution (Fig. 5.3).

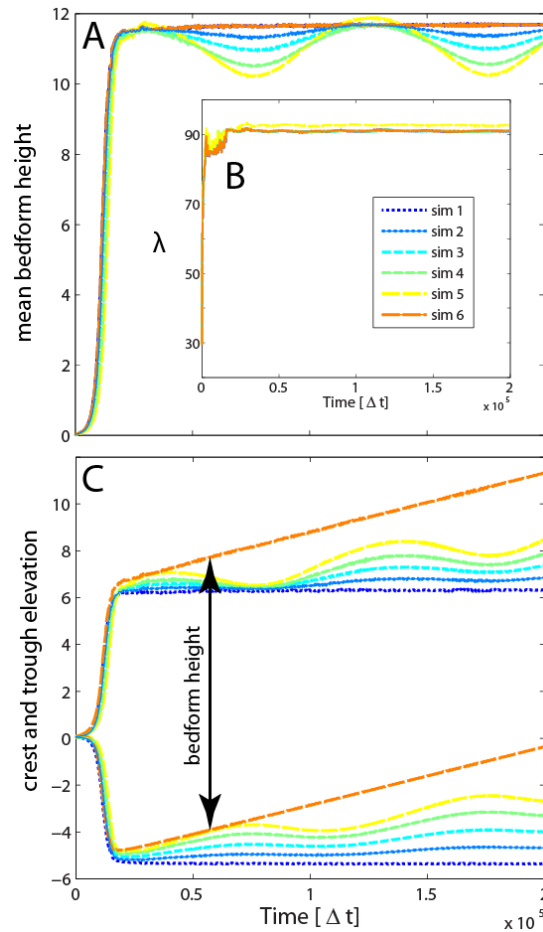


Figure 5.4: Transient bedform shape. A) $\langle h \rangle$ Shown as a function of model time steps. B) $\langle \lambda \rangle$ Shown as function of model time steps. C) Lower curves are mean trough elevations, upper curves are mean crest elevation as a function of model time steps. Bedform height, $\langle h \rangle$ is given by the vertical distance between curves of like color.

Synthetic sections created under the influence of various allogenic drivers (Fig. 5.2) are shown in Figures 5.8a-5.13a. Each section is color-mapped by a relative time of deposition. Cooler colors represent early simulation time and hotter colors indicate later simulation time. Self-organization occurs as coalescing bedforms cover the bed (Fig. 5.5a). They change shape drastically as they begin to climb over each other and merge (Fig. 5.5b,c). At times, the set thicknesses generated by their mergers, deformation and movement (self-organization) can approach and exceed the local bedform height (Fig. 5.5c). As bedform growth rate increases dramatically (Fig. 5.4a, c), bedform troughs scour into bed materials far below the initial bed elevation (Fig. 5.4c). As a result, in all simulations the initially created stratigraphy is quickly eroded, and removed from the synthetic rock record (compare Fig 5.5c where $t=4E3$, and Fig 5.6a where $t=1E4$).

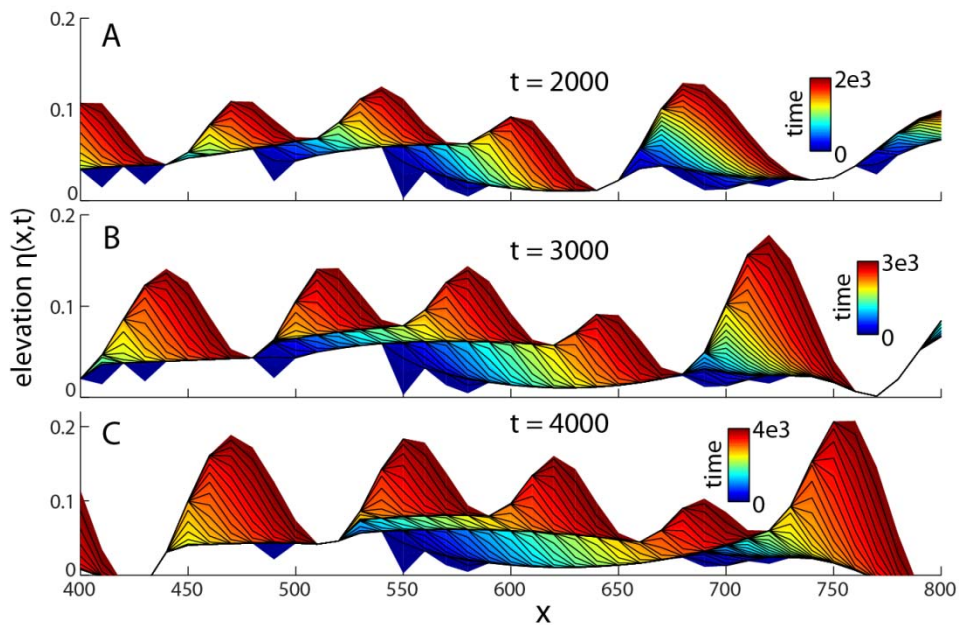


Figure 5.5: Self-organization of bedforms. Truncated sections (nodes 40-80) are generated using time steps of topography from simulation 5. A) Lowest blue triangles are the initial condition. Bedforms scour deeply and create set thicknesses almost equal to their height. B) middle bedforms climb over each other. C) smallest bedform decreases in height and merges with large rightmost bedform. Vertical exaggeration is 118.5x in all sections.

In all simulations, bedform troughs descend in local elevation until self-organization and strong growth has completed (Fig.5.4c). This growth phase of bedforms is associated with the deepest erosional surface found in all sections (Figs. 5.8a-5.13a). Bedforms that grow significantly more quickly than others (arrows in Fig. 5.6a) create the deepest scours. The observed spatial variation in trough elevations during the growth phase (Fig. 5.6b) creates groups of bedforms with higher troughs and groups of bedforms with lower troughs. This long wavelength, low amplitude variation in trough elevation migrates as a group celerity throughout the duration of each simulation. The group celerity is slightly faster than the bedform celerity. The group celerity is achieved by the same dynamics as individual bedform celerity, simply manifesting as a long wavelength ($\sim 1E3\Delta x$) low amplitude 1 [L] variation in topography. When bedform troughs ascend, due to the group motion, they begin to leave a substantial record (arrows, Fig. 5.6c).

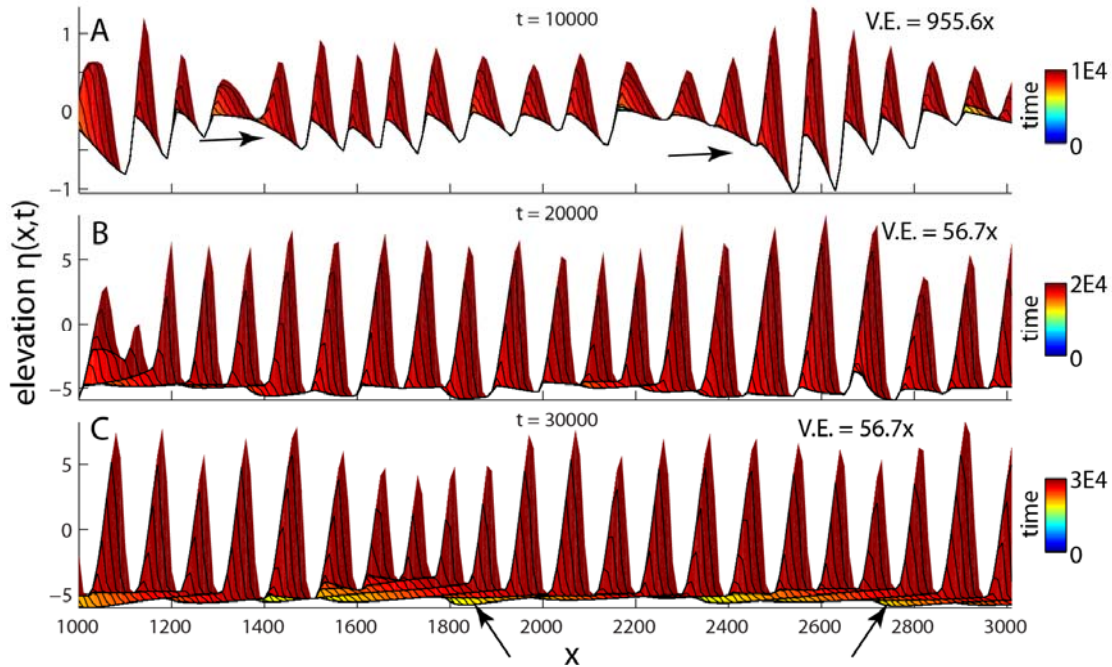


Figure 5.6: Deep scour and group formation. Truncated sections (nodes 100-300) are created using time steps from simulation 5. A) rapid growth of larger bedforms (arrows) creates B) long wavelength low amplitude groups of dune troughs. C) Group celerity is greater than bedform celerity, creating deposition from the long wavelength topography (arrows).

Topography associated with groups of bedforms is viewed as a repeated autogenic process, responsible for repeat phases of enhanced preservation and shredding of stratigraphy as a dune field matures. The passage of these groups of dunes creates the large cosets observed within stratigraphic sections (blue, orange and red regions, Fig. 5.7) and are readily identified in all simulations (Figs. 5.8a through 5.13a). This is accomplished by the group celerity carrying collections of deeper and shallower troughs through the domain. The sequences of lower-elevation troughs truncate previously deposited dune sets, producing a significant bounding surface, while sequences of dunes with increasingly higher-elevation troughs systematically leave behind sediment, at least temporarily aggrading the bed.

Within the high and low elevation clusters of dunes, individual bedforms have their own trough elevations. During early simulation time, the variation of trough elevation associated with

individual dunes is the highest. Slowly, over time, the morphodynamic feedback implemented in the interface equation acts to gather uneven topography, self-organization that leads to the formation of a train of uniform bedforms (Jerolmack and Mohrig, 2005). As trough elevations become more uniform, the stratigraphy internal to the group-created cosets becomes significantly more tabular (compare early cosets (blue) to tabular cosets (red) in Figure 5.7). The slow organization of trough elevations within groups of bedforms is perhaps most clearly demonstrated in Simulation 6 (Fig. 5.13a), where aggradation rate and boundary shear stress are both constant. The pronounced cosets are perceived as a repeated autogenic signal, created by the passage of “groups” as they cycle through the domain due to its periodic boundary conditions. The stratification within these cosets captures the homogenization of bedform trough elevation, a self-organization signal that can also be thought of as a secular autogenic signal. With deposition time, high angle of climb surfaces (blue regions) with large set thicknesses and little lateral continuity transition into stratification exhibiting lower angles of climb, smaller set thicknesses and very high lateral continuity (red regions, Fig. 5.13a). The section created by Simulation 1 (Fig. 5.8a) also contains this self-organization signal of trough elevation homogenization, but is incompletely preserved due to the imposed condition of zero net aggradation.

All simulations record early erosion due to bedform self-organization and growth and later group-derived bedform deposition. However, after bedform growth has largely ceased, allogenic drivers begin to significantly imprint on the resulting stratigraphic sections of simulations 2 – 5. As boundary shear stress increases, sediment transport rates increase, driving an increase in both bedform height, and trough scour depth (Figs. 5.2, 5.4). Due to the behavior driven by Equation 5.1, groups of large bedforms experience more growth than groups of smaller bedforms. Because of this unequal growth, the scouring action of large bedforms groups

outpaces trough elevation gain associated with the overall aggradation of the bed (Fig. 5.4c). This scouring motion creates large concave up truncation surfaces. Later on, as shear stress wains (Fig. 5.2), bedform troughs quickly rise and then slow down as they approach a maximum elevation (Fig. 5.4c). This scouring motion produces concave down truncation surfaces. These lower concave-up and upper concave-down surfaces create a characteristic asymmetric envelope of strata preserving the allogenicly influenced shape of the autogenically group-created coset. The increasing amplitude of both allogenic drivers from simulation 2 to simulation 5 (Fig. 5.2) produces the increasing coset thickness observed in Figures 5.9a through 5.12a. Within these cosets, individual set thicknesses also increase, as does the climb angle of internal truncation surfaces with increasing amplitude of the allogenic driver. Increases in the overall aggradation rate from zero in simulation 1 (Fig. 5.8a) to a constant value simulation 6 (Fig. 5.13a) increases the section thickness by a factor of ten.

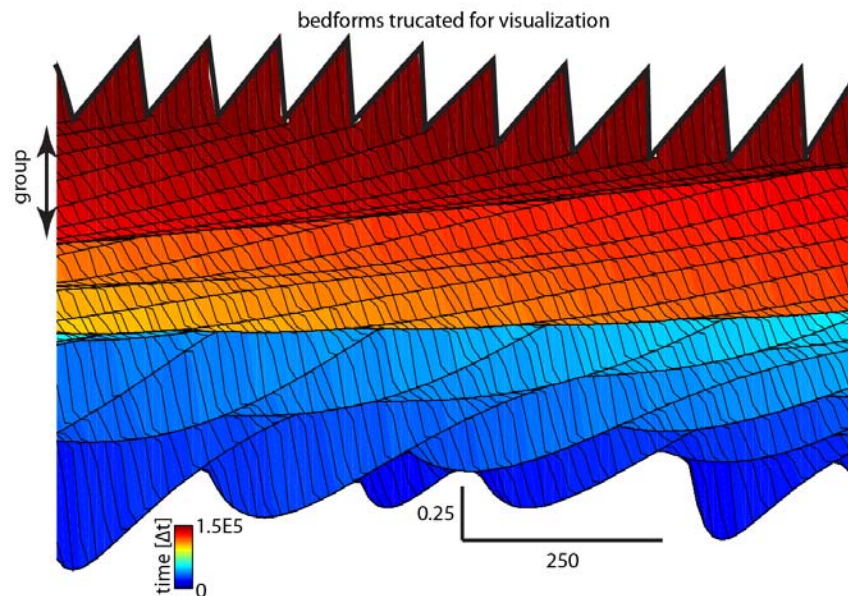


Figure 5.7: “group”-sourced cosets. These cosets are attributed to groups of high and low elevation bedform troughs. The coset created by the most recent group of bedforms is indicated by the side label “group”. Vertical Exaggeration is 3690.5x.

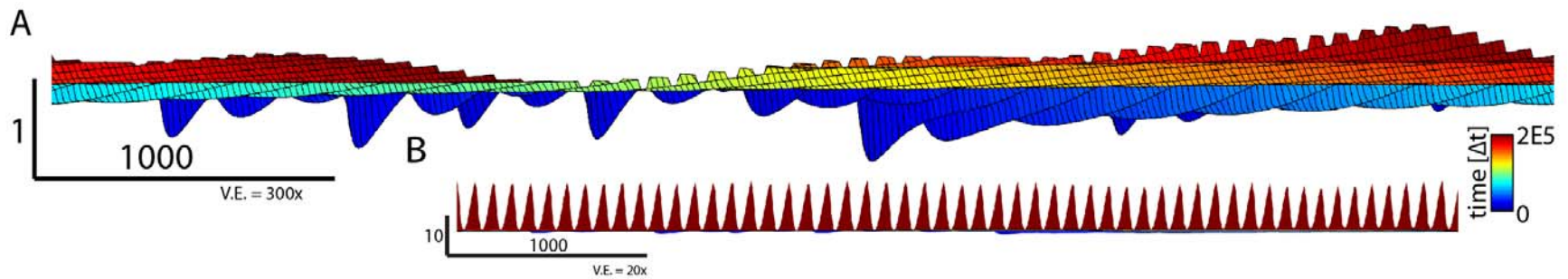


Figure 5.8: Stratigraphic section from simulation 1. A) Stratigraphy internal to bedforms is removed. Synthetic stratigraphy is color-mapped by the time of deposition. Cool colors are the oldest deposits and hot colors are the youngest deposits. V.E. = 300x B) Section with modern topography V.E. = 20x

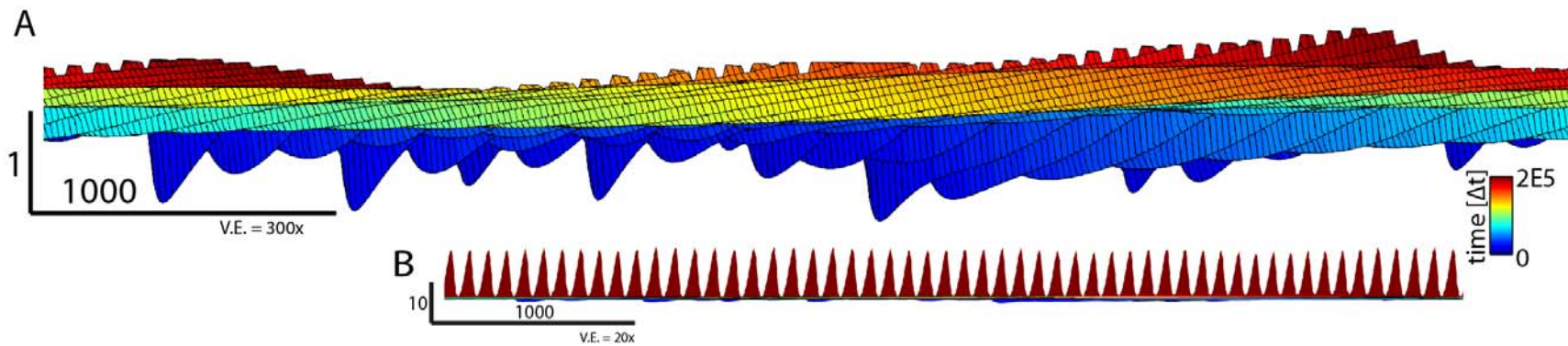


Figure 5.9: Stratigraphic section from simulation 2. A) Stratigraphy internal to bedforms is removed. Synthetic stratigraphy is color-mapped by the time of deposition. Cool colors are the oldest deposits and hot colors are the youngest deposits. V.E. = 300x B) Section with modern topography V.E. = 20x

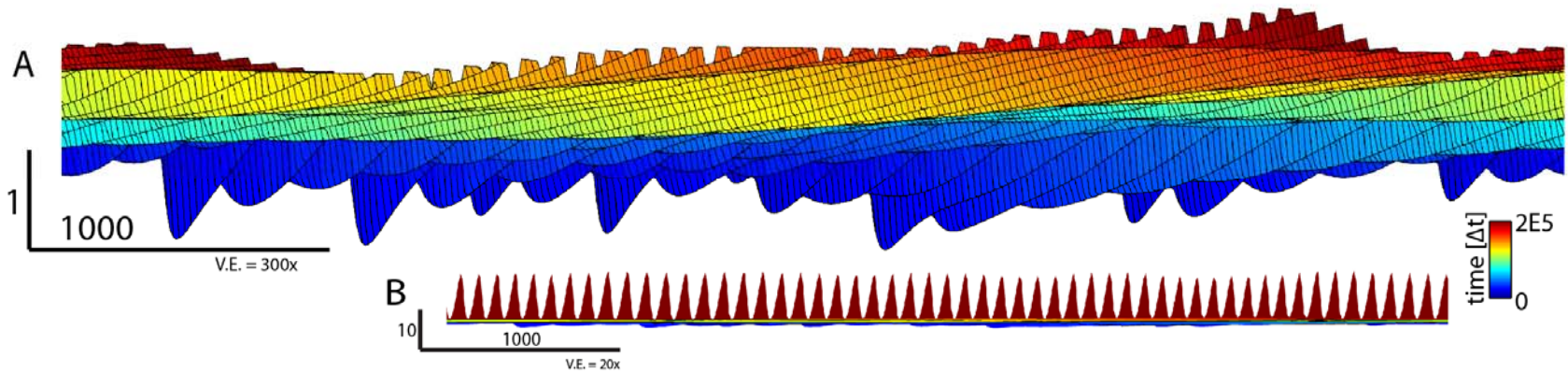


Figure 5.10: Stratigraphic section from simulation 3. A) Stratigraphy internal to bedforms is removed. Synthetic stratigraphy is color-mapped by the time of deposition. Cool colors are the oldest deposits and hot colors are the youngest deposits. V.E. = 300x B) Section with modern topography V.E. = 20x

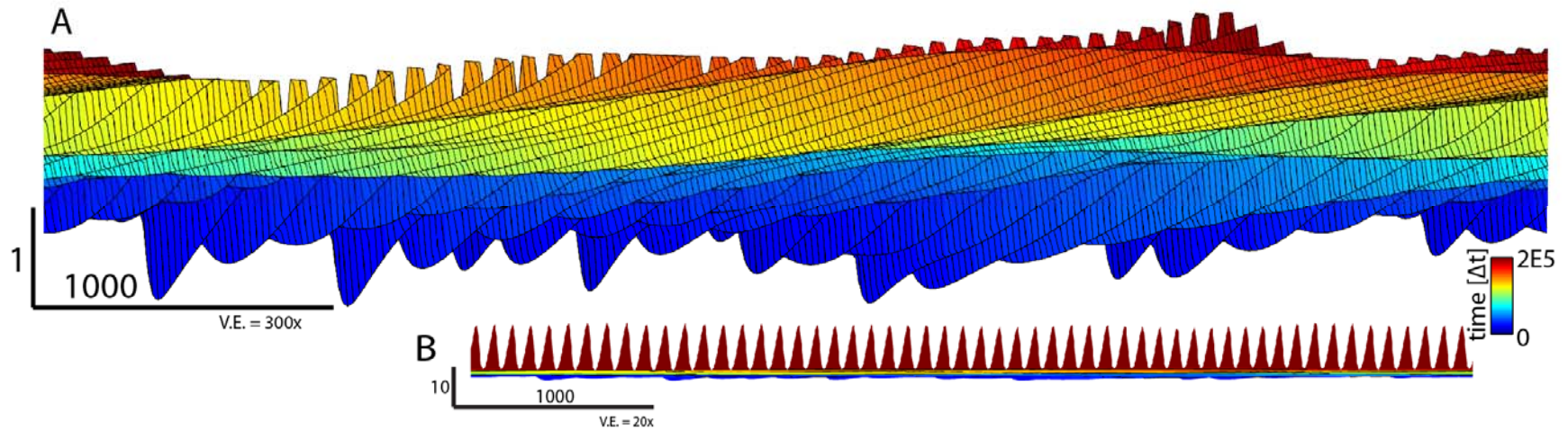


Figure 5.11: Stratigraphic section from simulation 4. A) Stratigraphy internal to bedforms is removed. Synthetic stratigraphy is color-mapped by the time of deposition. Cool colors are the oldest deposits and hot colors are the youngest deposits. V.E. = 300x B) Section with modern topography V.E. = 20x

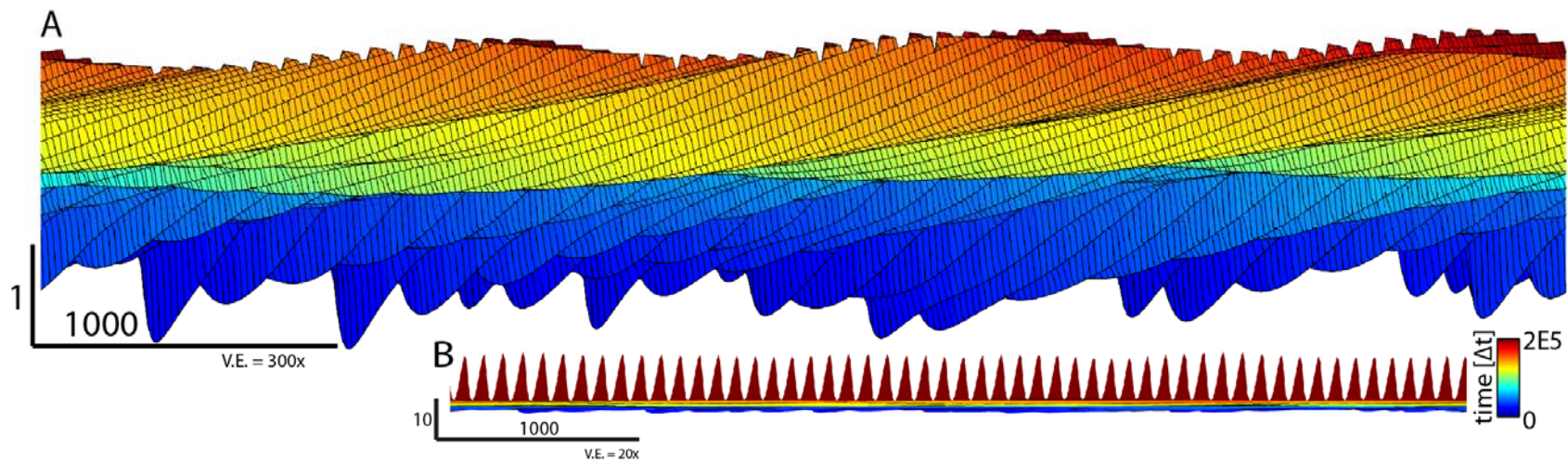


Figure 5.12: Stratigraphic section from simulation 5. A) Stratigraphy internal to bedforms is removed. Synthetic stratigraphy is color-mapped by the time of deposition. Cool colors are the oldest deposits and hot colors are the youngest deposits. V.E. = 300x B) Section with modern topography V.E. = 20x

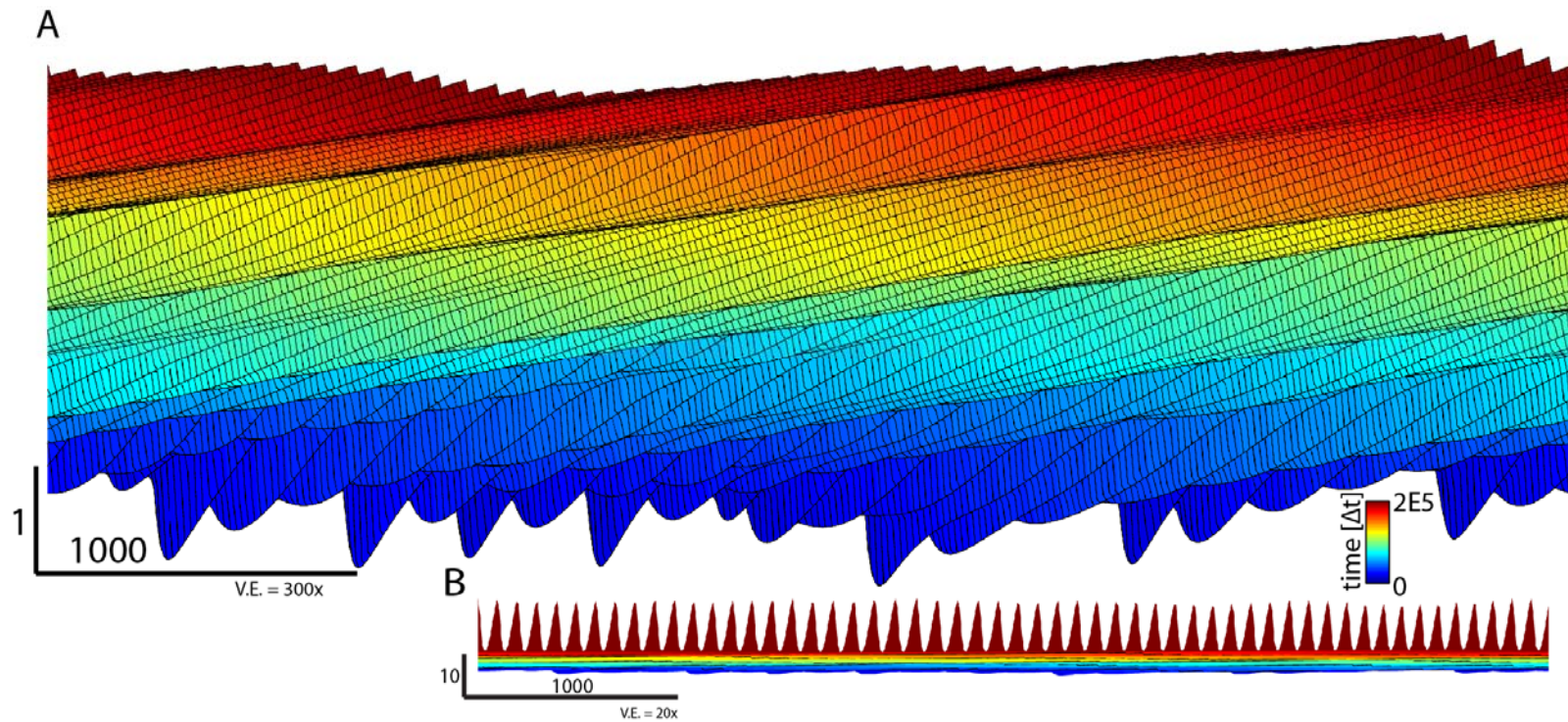


Figure 5.13: Stratigraphic section from simulation 6. A) Stratigraphy internal to bedforms is removed. Synthetic stratigraphy is color-mapped by the time of deposition. Cool colors are the oldest deposits and hot colors are the youngest deposits. V.E. = 300x B) Section with modern topography V.E. = 2

5.3.2 Preservation potential

For any simulation, many bedforms move past each grid node. These bedforms may or may not leave behind a deposit, depending on the local conditions. Comparing the number of bedforms that visit each node to the number of vertically stacked truncation surfaces present within the stratigraphy at each nodes is a way to compare the bedform preservation potential between simulations. If every bedform left behind a deposit there would be as many truncation surfaces in the section as bedforms that passed by that node. The number of bedforms that have visited each node are averaged across the domain (population = 501) and examined as a function of simulation time (Fig. 5.14a). Despite allogenic variability, the number of bedforms that have passed each node occurs at a nearly constant rate. For simulations 2 – 5, the average number of erosional surfaces in the vertical section shows significant variability over a period of approximately $1E5 \Delta t$, the same period prescribed to the allogenic drivers (Fig. 5.2).

Two distinct behaviors emerge when the number of erosional surfaces per vertical section is plotted as a ratio with bedform count (Fig. 5.14c). First, there is a precipitous drop in the number of surfaces per bedform during self-organization and strong growth (Fig. 5.5c, 5.6a) in bedform topography toward the beginning of all simulations (Fig.5.4, 5.14c). Second, at later time, the trains of more uniform bedforms encode stratigraphic surfaces at a fluctuating rate for Simulations 2 – 5 (Fig.5.14c) while Simulation 1 and 6

show a distinct decrease and increase in bedform preservation with time, respectively (Fig 5.14c).

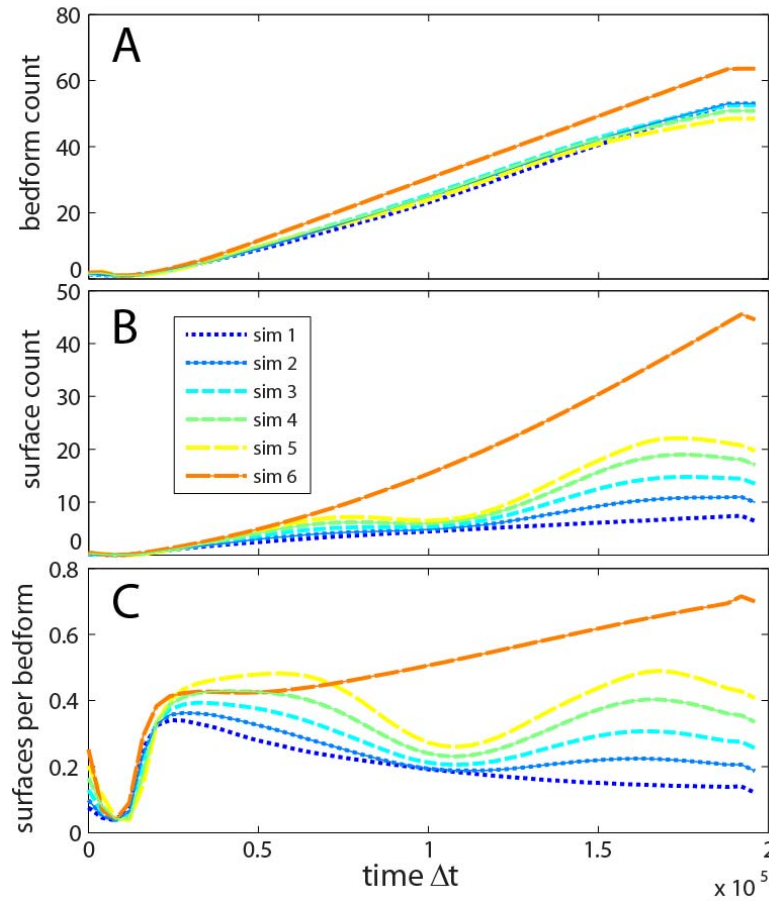


Figure 5.14: Comparison of bedform and surface count. (Each point is calculated using a population of 501). A) Bedform count, B) truncation-surface count and C) surface per bedform as a function of model time step.

5.3.3 Morphometric analysis

Bedform height is computed as the vertical distance between the crest and trough of a bedform. The coefficient of variation (CV) of bedform height is plotted in Figure

5.15b and shows a decrease for all simulations with time. By approximately $5E4 \Delta t$, the coefficient of variation for bedform height asymptotes to a nearly steady value of ~ 0.1 . Intriguingly, the coefficient of variation of bedform height is relatively insensitive to variation in the allogenic drivers $\tau_a(t)$ and $r(t)$ (Fig. 5.15b). Mean set thickness plotted in Figure 5.15a shows a dramatic early time increase in value, followed by a more gradual decrease with simulation time. Beyond the initial rapid decay in mean set thickness ($2.5E4 \Delta t$, Fig. 5.15a), slight increases and decreases appear for simulations 2 - 5. These small increases and decreases in mean set thickness with simulation time are correlated to relative increases and decreases in $r(t)$ and $\tau_a(t)$, the allogenic drivers (Fig. 5.15b). The ratio of mean bedform height to mean set thickness, ω , captures a pronounced decrease in preservation at early simulation time (Fig. 5.15c), then a slow decay in preservation for all simulations. Preservation exhibits small fluctuations which are due to the allogenic signal captured by set thickness (Fig. 5.15a), as the CV of bedform height does not exhibit significant fluctuations.

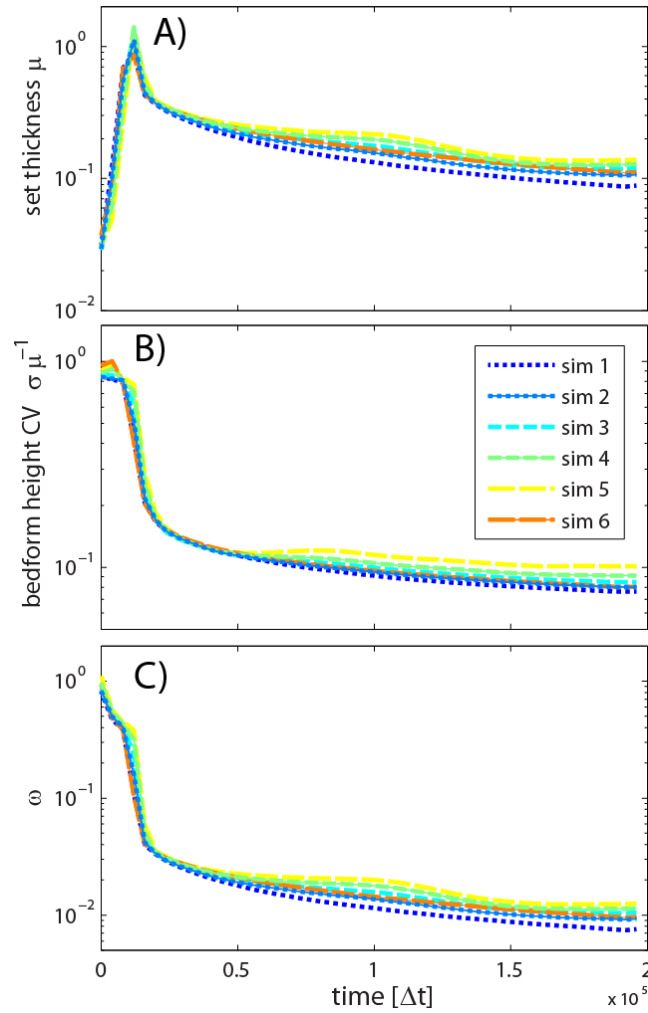


Figure 5.15: Moments of bedform topography through time. Vertical logarithmic axis. A) Mean set thickness as a function and B) Coefficient of variation of bedform height plotted as a function of time steps. C) Preservation ratio, ω , plotted as a function of model time steps.

Paola and Borgman (1991) present a stochastic theory that relates a distribution of set thicknesses to the passage of a distribution of bedform heights. In their theory, they envisioned a train of bedforms with random scour depths working and re-working sediment under the case of zero overall bed aggradation. This system demonstrates that a

gamma distributed population of bedform heights is related to an exponential distribution of set thicknesses. In their work the preservation ratio, ω is given as a function of the CV of bedform height ($\sigma\mu^{-1}$), $\omega = 0.8225(\sigma\mu^{-1})^2$, where, ω is the ratio of mean set thickness to the mean bedform height. While the numerically modeled scenarios here are different from the system assumed by Paola and Borgman (1991) we use their relationship to give much needed context for interpreting the numerical experiments as it provides an end-member expectation for the amount of bedform preservation. This relationship will be referred to as the *Paola curve*.

The preservation ratio versus coefficient of variation in bedform height with are plotted in the style of Paola and Borgman (1991) in Figure 5.16. Despite significant allogenic variability (Fig. 5.14) and its resulting morphological (Fig. 5.4) and stratigraphic variability (Figs. 5.8 through 5.13), simulation results plot neatly on top of each other, subparallel to the original Paola curve (black line, Fig. 5.16). Early simulation results plot in the upper right hand corner of Figure 5.16. Relatively quickly, self-organization and scouring below the initial condition elevation drive the preservation ratio below what is expected by the Paola curve for a given C.V. of bedform height. However, at longer simulation time, all simulations plot slightly above the Paola curve, suggesting that variability not apparent in bedform height elevation enhanced preservation of bedform topography (bottom left corner, Fig. 5.16). The fact that all simulations track subparallel to the Paola curve with time suggests that secular changes in bedform topography and resulting stratigraphy abide by such a stochastic theory.

Bridge and Best (1997) modified the *Paola and Borgman* [1991] relationship to include both aggradation rate, r and bedform celerity, c , $\omega = 0.8225(\sigma/\mu)^2 + r/c$. This modification to the original stochastic theory effectively translates potential scenarios along the ω axis (Fig. 5.16). In the numerical experiments presented here, self-organization, autogenic behavior and allogenic drivers create comingled changes in bedform celerity and aggradation rate. Therefore, the ratio r/c is cast as a single, lumped fitting parameter used to fit all simulation results shown in Figure 5.16. The resulting fitted model does better than the original Paola curve to describe the simulations, and yields $\frac{r}{c} = 0.0048$ with relatively high significance ($R^2 = 0.89$).

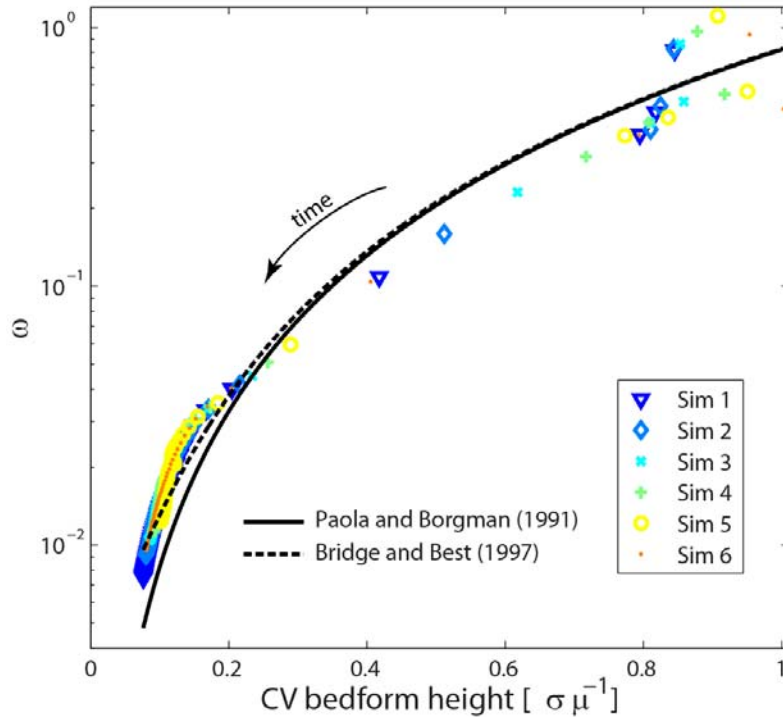


Figure 5.16: Stochastic models of bedform preservation. Coefficient of variation of bedform height as a function of preservation ratio for all simulations plotted in reference to the Paola curve and fitted Bridge and Best (1997) model. Temporal path of every simulation is shown by the time arrow.

5.3.4 Cumulative strata age distributions

The color coded stratal ages shown in stratigraphic sections (Figs. 5.8a through 5.13a) are plotted as cumulative distributions of age in Figure 5.17. All age distributions intercept the horizontal axis at approximately $1.8E5 \Delta t$, as all strata generated by self-organization during earliest time steps are subsequently eroded. Simulations 2 – 5 create cumulative age distributions that show separation into two distinct populations with increased allogenic variation (Figs. 5.2, 5.17). The two modes of these distributions are

correlated with the increases in aggradation rate $r(t)$ and decreases in boundary shear stress $\tau_A(t)$. Simulation 1 is driven using no bed aggradation and constant τ_A still contains two weakly distinct age populations. The older mode of simulation 1 corresponds to enhanced preservation potential in early simulation time ($t = 2.5E4$, Fig 5.14c). The second, younger and less distinct mode of simulation 1 corresponds to group-derived cosets that have yet to be truncated by on-going group motion of bedforms (youngest strata, Fig. 5.8a). Simulation 6, with constant aggradation rate and τ_A shows no curvature or inflection, suggesting that stratal ages are nearly uniformly distributed (Fig. 5.17).

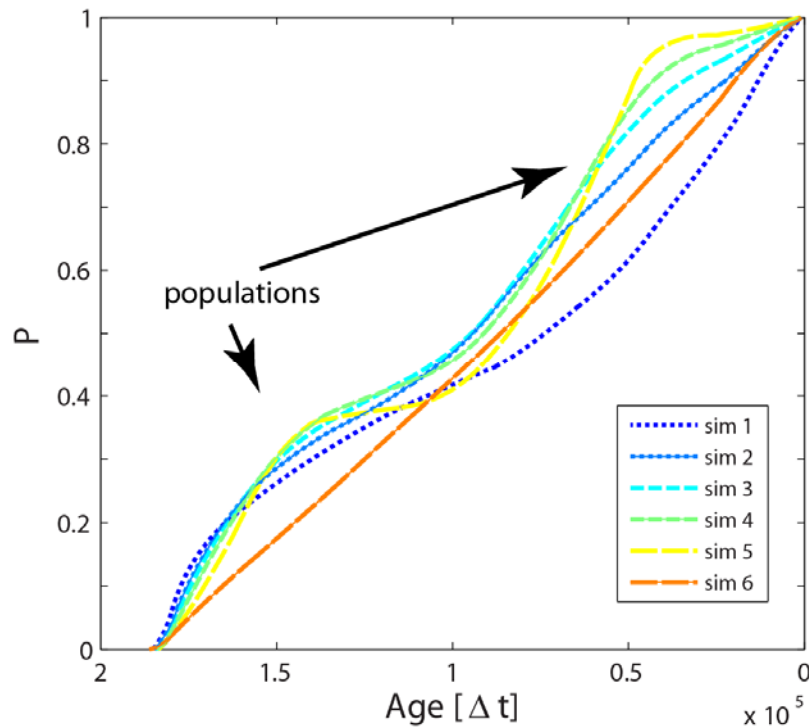


Figure 5.17: Normalized age distribution of preserved strata. The age distributions are calculated for each stratigraphic section shown in Figures 5.8 through 5.13. Inflections in the empirical CDF suggest multiple populations of strata ages.

5.4 DISCUSSION

Both allogenic and autogenic signals are identified and preserved within the synthetic stratigraphic cross-sections. Careful observation of these sections shows that all modeled bedform fields and their resultant stratigraphy are dominated by self-organization processes at early simulation time. Erosion to saturated values of trough elevation (Fig. 5.4) generates the deep scours seen in all sections (Figs. 5.8a - 5.13a). During the self-organization phase, differential growth rates of bedforms from the original horizontal surface creates “groups” of high elevation troughs and “groups” of lower elevation troughs. These groups of bedforms ultimately act as a repetitive autogenic process which selectively preserve and shred stratification. Each group of higher elevation troughs is tied to greater amounts strata being transferred into the static bed, while groups of lower elevation troughs erode the deposits of proceeding bedforms.

While the formation of “groups” is entirely due to internal dynamics and resulting self-organization, the stratification internal to group-derived cosets and the shape of the bounding surfaces enveloping cosets may contain allogenic signals. Periodic fluctuations in allogenic drivers are correlated to increased set thickness (Fig. 5.15a), increased angles of climb defined by truncation surfaces (Figs. 5.9a through 5.12a), increased curvature of the truncation surfaces, enhanced preservation potential (Fig. 5.14) and bimodality in stratal age distributions (Fig. 5.17). However, these allogenic signals are comingled with self-organization signals due to ongoing homogenization of bedform trough elevation with simulation time. The progressive decay of bedform trough elevation variability

drives the observed stratigraphic transition from relatively thick and laterally discontinuous sets with relatively high climb angles to thinner, relatively tabular sets that exhibit lower angles of climb at late simulation time (Figs. 5.8a, 5.13a). Intriguingly, this signal from self-organization causes a decrease in preservation potential for a zero-aggradation case (simulation 1, Fig. 5.14c), and an increase in preservation potential for a constant aggradation rate (simulation 6, Fig. 5.14c). This is because nearly uniform trough elevations do not allow for preservation of bedform topography in the absence of aggradation. Signals of self-organization and autogenic behavior are preserved in every section (Fig. 5.8a-5.13a). Allogenic signals in simulations 2-5, both enhance and reduce the preservation of signals sourced from self-organization and autogenic behavior. Stronger magnitudes of sedimentation cycles (Figs. 5.1, 5.2) result in a more distinct bimodality of stratal ages (Fig. 5.17), as well as higher preservation potential and preservation ratio (Figs. 5.14c, 5.15c).

Preservation due to self-organization (a secular autogenic process), repeated autogenic behavior and allogenic drivers are not considered by traditional length-scale analysis of bedform cross-stratification (Eg: Paola and Borgman (1991)). Surprisingly, all simulation results are found to plot nearly on top of each other, subparallel to the Paola curve. The modification of Paola and Borgman (1991) by Bridge and Best (1997) captures the enhanced preservation of bedform topography at later simulation time (bottom left corner, Fig. 5.16). Because internal dynamics couple changes in bedform celerity, c , with changes in aggradation rate, r , the partitioning enhanced preservation

ratio, ω into the ratio r/c is ambiguous. For our simulation results, we suggest that the fitted parameter describes the enhanced preservation of bedform topography sourced from self-organization, group-derived autogenic behavior and/or allogenic variability.

5.5 CONCLUSIONS

A 1D bedform surface evolution equation is modified to accept changes in mean surface elevation and driven using different allogenic signals. Within the model domain, bedforms of similar size group together (Fig. 5.6). Consecutive bedform trough elevations create long wavelengths of low amplitude topography, called “groups”. “Groups” of bedforms create cosets within the synthetic stratification. Stratification internal to the cosets contains comingled signals from both allogenic and autogenic sources (Fig. 5.7). Signals from allogenic drivers are overwhelmed by autogenic signals during early deposition. However, at later simulation time, allogenic signals are recorded as a separate population of stratal ages (Fig. 5.17). Self-organization and allogenic signals are entered into the rock record through autogenic bedform “group” deposition. Groups with high trough elevations are postulated to act as a buffer to protect aeolian rock records from complete shredding by self-organization or allogenic variability.

The co-evolution of bedform topography and stratification are found to track neatly subparallel to the Paola curve (Fig. 5.16) or the expected relationship between distributions of bedform topography and set thickness. A simple translation of the Paola curve (Bridge and Best, 1997) results in a significantly better description of the model

results (Fig. 5.16). Self-organization of bedform topography homogenizes bedform trough elevation, causing linked changes in the CV of bedform height and preservation ratio, ω , nearly as expected from random topography (time arrow, Fig. 5.16). However, enhanced preservation by autogenic groups of dunes and allogenic variability (bottom corner, Fig. 5.16) is not considered by Paola and Borgman (1991) and is thought to be described by a single lumped parameter, in a somewhat similar fashion to the modification proposed by Bridge and Best (1997).

Bedform patterns rapidly organize with time, which is shown by rapid exponential growth to saturation of bedform height and wavelength (Baas, 1994; Venditti et al., 2005). While aggradation aids the preservation of cross-strata, the preservation of cross-strata does not solely depend on allogenic sediment input. Self-organization and subsequent autogenic changes alone are a mechanism for the preservation of cross-strata, as organization of a roughened bed into coherent bedform topography creates a substantial stratigraphic record (Fig. 5.8a). However, allogenic variability helps increase bedform preservation. Bedform systems with strong allogenic signals may coincidentally create anomalously high preservation potentials (Fig. 5.14c) and ratios (Fig. 5.16). Simply detecting greater than expected preservation (Paola curve) may suggest the influence of naturally occurring allogenic or anthropogenic signals acting on bedform topography. Bedforms rapidly self-organize with distance from boundary conditions, such as a sediment source area or with time, or changes in the annual cycle of sediment transporting winds (Ewing and Kocurek, 2010; Kocurek et al., 2010). Each boundary

condition may uniquely or similarly influence preservation. Future field, flume, and modeling efforts are warranted to understand the preservation of signals sourced from bedform system boundary conditions within cross-stratified rock records.

5.6 ACKNOWLEDGEMENTS

Caroline Hern provided continuous feedback and conceptual steering and support for this project. Funding for this work was provided by the Royal Dutch Shell Oil Company. This work does not reflect the views of the Royal Dutch Shell Oil Company.

Chapter 6: Conclusions

Bedform self-organization occurs due to a hierarchical cascade of interactions between granules, landforms and fluid motions within fields of bedforms. Boundary conditions drive interactions within the bedform system. In this conceptual framework, dynamic bedform topography is an amalgamation of signals from interactions within the system and bedform system boundary conditions. One such boundary condition is a multidirectional wind regime, or annual cycle of sediment transporting winds. Self-organization of dune crests as a trend line is a known response to the wind regime boundary condition (du Pont et al., 2014; Rubin and Hunter, 1987; Rubin and Ikeda, 1990). Yet, seemingly paradoxical, individual dunes deform and move unevenly with each sediment transporting wind event (Eastwood et al., 2012; Pedersen et al., 2015). In chapter 2 dune crests are shown to maintain geometric organization as a trend line due to symmetrically distributed sediment flux with compass direction. Dunes within a study area of White Sands, NM move unevenly over an annual cycle of wind. However, the average values of dune motion and sediment flux become steady when sampled over a sufficiently large area. Although not expected to be general, for White Sands, NM this sampling area represents approximately six average sized dunes. Conceptually, this relationship describes the spatial scale where the multidirectional wind regime boundary condition interacts with bedforms to maintain geometric organization of the dune field.

Bedform self-organization requires that interactions occur in a regular, reproducible fashion, yet do so spontaneously. In chapter 3, bedforms with portions of crest sufficiently oblique to upstream fluid flow are demonstrated to spontaneously generate helical vortices that trail from the lee surface. The along parent bedform crest spacing between sequential vortex filaments scales with parent bedform height and the incidence angle of the bedform crest. The enigmatic occurrence of bedform spurs is explained by a trailing helical vortex scouring bed materials and piling sediment into the linear body of a bedform spur. Trailing helical vortices capture sediment from the lee slope of the parent bedform and the bed area underneath the helical vortex. The trailing helical vortex creates a conduit of augmented sediment transport. Depending on proximity, the trailing helical vortex can scour through the downstream bedform, directly causing an interaction at the bedform scale. Alternatively, the trailing helical vortex can route sediment to the downstream bedform. In either scenario, a structure of fluid motion within the wake of an upstream bedform causes deformation of a downstream bedform. Frequently the deformed downstream bedform forms an oblique incidence angle, and begins to trail its own helical vortices. The newly created trailing helical wake from the deformed bedform creates additional conduits of augmented sediment transport. In this fashion, a bedform-scale interaction is mediated by an interaction between bedform shape and fluid structure. This feedback helps to explain the transition between straight crested (2D) to sinuously crested bedforms (3D), as bedform deformation begets yet more bedform deformation.

Bedform system boundary conditions exert an influence on the dynamic topography within the bedform field. In chapter 4, a surface model of subaqueous bedform topography developed by Jerolmack and Mohrig (2005) is modified to accept sediment transport in multiple directions, and using periodic and fixed sediment elevation boundary conditions. With these modifications, the non-linear interaction between topography and sediment flux of Jerolmack and Mohrig (2005) is demonstrated to generate realistic aeolian bedform topography. The aeolian surface model is applied to study dynamic bedform topography resulting from four different sets of boundary conditions: Unimodal and bimodal transport regimes growing bedform topography with and without the constraint of a fixed elevation “source area” boundary condition. Regardless of spatial boundary conditions, a unimodal transport regime produced transverse bedforms, and the bimodal transport regime produced linear bedforms. Although the results are specific to the given modeling scenario, transverse bedforms were found to grow to equilibrium values of bedform crest height and wavelength faster in time, but slower in distance from the fixed elevation boundary condition when compared to the bimodal transport regime. Therefore, different transport regime boundary conditions are shown to drive bedform growth to equilibrium at different rates and result in different morphologies.

Over long time scales, bedform system boundary conditions are transient. These transient signals propagate into bedform fields, which may create cross-stratified deposits. The preservation of signals originating from bedform system boundary

conditions and autogenic behavior is investigated in chapter 5. A 1D bedform surface evolution equation is gleaned from chapter 4 and adapted to accept changes in mean surface elevation and driven using allogenic signals though. This operation produces synthetic cross stratified deposits. With surprising consistency, every simulation forms autogenic bedform “groups” of similar trough elevation. These bedform “groups” create extensive geobodies within the stratigraphic sections that preserve comingled autogenic and allogenic signals. Time evolution of the bedform topography-stratigraphy system loosely follows the stochastic theory of Paola and Borgman (1991). Under scrutiny, A modification to Paola and Borgman (1991) proposed by Bridge and Best (1997), is interpreted to accommodate the preservation of bedform topography due to autogenic and allogenic signals.

Conceptualizing the deposits of bedform systems as a consequence of a hierarchical system of interactions fueled by boundary conditions provides much needed context and guidance for future work. At the most grand scale, work to model ancient climate, sediment transport and the resulting sedimentary deposit should parallel efforts to reconstruct the transport regime of ancient climates, preserved within aeolian stratigraphy. To accomplish this task, the aeolian bedform surface model should be exploited to forward model many boundary conditions and resulting synthetic stratigraphic volumes as possible, far beyond the few exercises presented in this dissertation. These model results may help to inform new stochastic relationships between dynamic topography and stratigraphy, with specific attention to detecting

variation in topography due to variant and invariant boundary conditions of bedform systems.

Appendix A: Exponential-saturation and two term exponential fits

Fit model:		$h(\xi) = a(1 - e^{-b\xi}) + c$	$\lambda(\xi) = a(1 - e^{-b\xi}) + c$	$\psi(\xi) = ae^{-b\xi} + ce^{-d\xi}$
Unimodal	<i>Periodic</i> $\xi = t$	$a = 7.32$ $b = 0.0009415$ $c = 0.01716$ $R^2 = 0.9914$	$a = 41.01$ $b = 0.001048$ $c = 43.03$ $R^2 = 0.9954$	$a = 3446$ $b = -0.003722$ $c = 278.6$ $d = -2.571 \cdot 10^{-5}$ $R^2 = 0.9921$
	<i>Flux</i> $\xi = x$	$a = 11.71$ $b = 0.004986$ $c = 0.06335$ $R^2 = 0.9816$	$a = 37.93$ $b = 0.004677$ $c = 44.38$ $R^2 = 0.9581$	$a = 1150$ $b = -0.01866$ $c = 65.92$ $d = -0.0006289$ $R^2 = 0.9931$
Bimodal	<i>Periodic</i> $\xi = t$	$a = 24.54$ $b = 0.0001982$ $c = 0.8$ $R^2 = 0.9831$	$a = 97.63$ $b = 0.0001989$ $c = 32.61$ $R^2 = 0.9796$	$a = 3659$ $b = -0.003983$ $c = 128$ $d = -6.428 \cdot 10^{-5}$ $R^2 = 0.9921$
	<i>Flux</i> $\xi = x$	$a = 19.13$ $b = 0.02602$ $c = 1.857$ $R^2 = 0.8638$	$a = 104.3$ $b = 0.02116$ $c = 23.12$ $R^2 = 0.9242$	$a = 403.2$ $b = -0.03328$ $c = 0.008877$ $d = 0.001901$ $R^2 = 0.6706$

Table 4.3: Fit parameters. Non-linear least squares fitting of model equations to dune crest height, wavelength and number of terminations as a function of space and time in model simulations.

Appendix B: Supplemental material

Video files for Chapter 3:

North_Loup_ripple_fan.avi

Single_spur.mov

North_Loup_bedform_interaction.avi

Spur_bearing_bedforms_1.avi

Spur_bearing_bedforms_2.avi

Video files for Chapter 4:

bimodal_periodic_boundary.mp4

bimodal_source_boundary.mp4

unimodal_periodic_boundary.mp4

unimodal_source_boundary.mp4

Video files for Chapter 5:

Simulation_1.mp4

Simulation_2.mp4

Simulation_3.mp4

Simulation_4.mp4

Simulation_5.mp4

Simulation_6.mp4

Bibliography

- Allen, J. R. L., 1968, Current ripples: their relation to patterns of water and sediment motion, North-Holland Pub. Co.
- Allen, J. R. L., 1977, The plan shape of current ripples in relation to flow conditions: *Sedimentology*, v. 24, no. 1, p. 53-62.
- Baas, J. H., 1994, A flume study on the development and equilibrium morphology of current ripples in very fine sand: *Sedimentology*, v. 41, no. 2, p. 185-209.
- Bagnold, R. A., 1941, *The physics of blown sand and desert dunes*, Methuen & co., ltd.
- Baitis, E., Kocurek, G., Smith, V., Mohrig, D., Ewing, R. C., and Peyret, A.-P., 2014, Definition and origin of the dune-field pattern at White Sands, New Mexico: *Aeolian Research*, v. 15, p. 269-287.
- Baitis, E. E., 2011, *Patterns and paleoshorelines of White Sands Dune Field, New Mexico*.
- Barabási, A.-L., 1995, *Fractal concepts in surface growth*, Cambridge university press.
- Bridge, J., and Best, J., 1997, Preservation of planar laminae due to migration of low-relief bed waves over aggrading upper-stage plane beds: comparison of experimental data with theory: *Sedimentology*, v. 44, no. 2, p. 253-262.
- Canny, J., 1986, A computational approach to edge detection: *Pattern Analysis and Machine Intelligence*, IEEE Transactions on, no. 6, p. 679-698.
- Cooper, W. S., 1958, *Coastal sand dunes of Oregon and Washington*: Geological Society of America Memoirs, v. 72, p. 1-162.
- Dietrich, W. E., and Smith, J. D., 1984, Bed load transport in a river meander: *Water Resources Research*, v. 20, no. 10, p. 1355-1380.
- Diniega, S., 2010, *Modeling aeolian dune and dune field evolution*, THE UNIVERSITY OF ARIZONA.
- du Pont, S. C., Narteau, C., and Gao, X., 2014, Two modes for dune orientation: *Geology*, v. 42, no. 9, p. 743-746.
- Durán, O., Parteli, E. J., and Herrmann, H. J., 2010, A continuous model for sand dunes: Review, new developments and application to barchan dunes and barchan dune fields: *Earth Surface Processes and Landforms*, v. 35, no. 13, p. 1591-1600.
- Eastwood, E., Nield, J., Baas, A., and Kocurek, G., 2011, Modelling controls on aeolian dune-field pattern evolution: *Sedimentology*, v. 58, no. 6, p. 1391-1406.
- Eastwood, E. N., Kocurek, G., Mohrig, D., and Swanson, T., 2012, Methodology for reconstructing wind direction, wind speed and duration of wind events from aeolian cross-strata: *Journal of Geophysical Research-Earth Surface*, v. 117, no. F3, p. F03035.
- Elliott, T., and Gardiner, A. R., 2009, Ripple, Megaripple and Sandwave Bedforms in the Macrotidal Loughor Estuary, South Wales, U.K, *Holocene Marine Sedimentation in the North Sea Basin*, Blackwell Publishing Ltd., p. 51-64.

- Ewing, R., and Kocurek, G., 2010, Aeolian dune-field pattern boundary conditions: *Geomorphology*, v. 114, no. 3, p. 175-187.
- Ewing, R. C., Kocurek, G., and Lake, L. W., 2006a, Pattern analysis of dune-field parameters: *Earth Surface Processes and Landforms*, v. 31, no. 9, p. 1176-1191.
- Ewing, R. C., Kocurek, G., and Lake, L. W., 2006b, Pattern analysis of dune-field parameters: *Earth Surface Processes and Landforms*, v. 31, no. 9, p. 1176-1191.
- Exner, F. M., 1925, Über die Wechselwirkung zwischen Wasser und Geschiebe in Flüssen (in German): *Sitz. Acad. Wiss. Wien Math. Naturwiss. Abt. 2a*, v. 134, p. 165-203.
- Guala, M., Singh, A., BadHeartBull, N., and Foufoula-Georgiou, E., 2014, Spectral description of migrating bed forms and sediment transport: *Journal of Geophysical Research: Earth Surface*, v. 119, no. 2, p. 123-137.
- Guy, H. P., Simons, D. B., and Richardson, E. V., 1966, Summary of alluvial channel data from flume experiments, 1956-61, US Government Printing Office.
- Hersen, P., 2004, On the crescentic shape of barchan dunes: *The European Physical Journal B-Condensed Matter and Complex Systems*, v. 37, no. 4, p. 507-514.
- Howard, A. D., Morton, J. B., Gad-El-Hak, M., and Pierce, D. B., 1978, Sand transport model of barchan dune equilibrium: *Sedimentology*, v. 25, no. 3, p. 307-338.
- Jackson, J. A., Mehl, J. P., and Neuendorf, K. K., 2005, *Glossary of geology*, Springer Science & Business Media.
- Jackson, P., and Hunt, J., 1975, Turbulent wind flow over a low hill: *Quarterly Journal of the Royal Meteorological Society*, v. 101, no. 430, p. 929-955.
- Jerolmack, D. J., Ewing, R. C., Falcini, F., Martin, R. L., Masteller, C., Phillips, C., Reitz, M. D., and Buynevich, I., 2012, Internal boundary layer model for the evolution of desert dune fields: *Nature Geosci*, v. 5, no. 3, p. 206-209.
- Jerolmack, D. J., and Mohrig, D., 2005, A unified model for subaqueous bed form dynamics: *Water Resources Research*, v. 41, no. 12, p. W12421.
- Khosronejad, A., and Sotiropoulos, F., 2014, Numerical simulation of sand waves in a turbulent open channel flow: *Journal of Fluid Mechanics*, v. 753, p. 150-216.
- Kocurek, G., 1999, The aeolian rock record (Yes, Virginia, it exists, but it really is rather special to create one): *Aeolian environments, sediments and landforms*, v. 239, p. 259.
- Kocurek, G., Carr, M., Ewing, R., Havholm, K. G., Nagar, Y., and Singhvi, A., 2007, White Sands Dune Field, New Mexico: age, dune dynamics and recent accumulations: *Sedimentary Geology*, v. 197, no. 3, p. 313-331.
- Kocurek, G., and Ewing, R. C., 2005, Aeolian dune field self-organization—implications for the formation of simple versus complex dune-field patterns: *Geomorphology*, v. 72, no. 1, p. 94-105.
- Kocurek, G., Ewing, R. C., and Mohrig, D., 2010, How do bedform patterns arise? New views on the role of bedform interactions within a set of boundary conditions: *Earth Surface Processes and Landforms*, v. 35, no. 1, p. 51-63.

- Kocurek, G., Townsley, M., Yeh, E., Havholm, K., and Sweet, M., 1992, Dune and dune-field development on Padre Island, Texas, with implications for interdune deposition and water-table-controlled accumulation: *Journal of Sedimentary Research*, v. 62, no. 4.
- Kroy, K., Sauermann, G., and Herrmann, H. J., 2002, Minimal model for aeolian sand dunes: *Physical Review E*, v. 66, no. 3, p. 031302.
- Lancaster, N., Kocurek, G., Singhvi, A., Pandey, V., Deynoux, M., Ghienne, J.-F., and Lô, K., 2002, Late Pleistocene and Holocene dune activity and wind regimes in the western Sahara Desert of Mauritania: *Geology*, v. 30, no. 11, p. 991-994.
- Lancaster, N., Nickling, W., Neuman, C. M., and Wyatt, V., 1996, Sediment flux and airflow on the stoss slope of a barchan dune: *Geomorphology*, v. 17, no. 1, p. 55-62.
- Leclair, S. F., 2002, Preservation of cross-strata due to the migration of subaqueous dunes: an experimental investigation: *Sedimentology*, v. 49, no. 6, p. 1157-1180.
- Levi, E., 1983, A universal Strouhal law: *Journal of Engineering Mechanics*, v. 109, no. 3, p. 718-727.
- McElroy, B., and Mohrig, D., 2009, Nature of deformation of sandy bed forms: *Journal of Geophysical Research: Earth Surface*, v. 114, no. F3, p. F00A04.
- Meyer-Peter, E., and Müller, R., Formulas for bed-load transport 1948, IAHR.
- Mohrig, D., and Smith, J. D., 1996, Predicting the migration rates of subaqueous dunes: *Water Resources Research*, v. 32, no. 10, p. 3207-3217.
- Narteau, C., Zhang, D., Rozier, O., and Claudin, P., 2009, Setting the length and time scales of a cellular automaton dune model from the analysis of superimposed bed forms: *Journal of Geophysical Research: Earth Surface* (2003–2012), v. 114, no. F3.
- Norberg, C., 2003, Fluctuating lift on a circular cylinder: review and new measurements: *Journal of Fluids and Structures*, v. 17, no. 1, p. 57-96.
- Paola, C., and Borgman, L., 1991, Reconstructing random topography from preserved stratification: *Sedimentology*, v. 38, no. 4, p. 553-565.
- Pedersen, A., Kocurek, G., Mohrig, D., and Smith, V., 2015, Dune deformation in a multidirectional wind regime: White Sands Dune Field, New Mexico: *Earth Surface Processes and Landforms*.
- Perillo, G. M. E., 1995, *Geomorphology and Sedimentology of Estuaries*, Elsevier Science.
- Perillo, M. M., Best, J. L., and Garcia, M. H., 2014a, A new phase diagram for combined-flow bedforms: *Journal of Sedimentary Research*, v. 84, no. 4, p. 301-313.
- Perillo, M. M., Best, J. L., Yokokawa, M., Sekiguchi, T., Takagawa, T., and Garcia, M. H., 2014b, A unified model for bedform development and equilibrium under unidirectional, oscillatory and combined-flows: *Sedimentology*, v. 61, no. 7, p. 2063-2085.

- Ping, L., Narteau, C., Dong, Z., Zhang, Z., and Courrech du Pont, S., 2014, Emergence of oblique dunes in a landscape-scale experiment: *Nature Geosci*, v. 7, no. 2, p. 99-103.
- Press, W. H., Teukolsky, S., Vetterling, W., and Flannery, B., 1988, *Numerical recipes in C*: Cambridge University Press, v. 1, p. 3.
- Rubin, D. M., 1987, Cross-bedding, bedforms, and paleocurrents, *SEPM*.
- Rubin, D. M., and Hunter, R. E., 1985, Why deposits of longitudinal dunes are rarely recognized in the geologic record: *Sedimentology*, v. 32, no. 1, p. 147-157.
- , 1987, Bedform alignment in directionally varying flows: *Science*, v. 237, no. 4812, p. 276-278.
- Rubin, D. M., and Ikeda, H., 1990, Flume experiments on the alignment of transverse, oblique, and longitudinal dunes in directionally varying flows: *Sedimentology*, v. 37, no. 4, p. 673-684.
- Snarski, S. R., 2004, Flow over yawed circular cylinders: Wall pressure spectra and flow regimes: *Physics of Fluids (1994-present)*, v. 16, no. 2, p. 344-359.
- Soo, S. L., 2013, *Instrumentation for fluid particle flow*, Univ. Press of Mississippi.
- Sorby, H. C., 1859, On the structures produced by the currents present during the deposition of stratified rocks: *Geologist*, v. 2, p. 137-147.
- Southard, J. B., and Boguchwal, L. A., 1990, Bed configuration in steady unidirectional water flows; Part 2, Synthesis of flume data: *Journal of Sedimentary Research*, v. 60, no. 5, p. 658-679.
- Strong, N., and Paola, C., 2008, Valleys that never were: time surfaces versus stratigraphic surfaces: *Journal of Sedimentary Research*, v. 78, no. 8, p. 579-593.
- Strouhal, V., 1878, Ueber eine besondere Art der Tonerregung: *Annalen der Physik*, v. 241, no. 10, p. 216-251.
- Sweet, M., and Kocurek, G., 1990, An empirical model of aeolian dune lee-face airflow: *Sedimentology*, v. 37, no. 6, p. 1023-1038.
- Sweet, M., Nielson, J., Havholm, K., and Farrelley, J., 1988, Algodones dune field of southeastern California: case history of a migrating modern dune field: *Sedimentology*, v. 35, no. 6, p. 939-952.
- Thomson, K., and Morrison, D., 1971, The spacing, position and strength of vortices in the wake of slender cylindrical bodies at large incidence: *Journal of Fluid Mechanics*, v. 50, no. 04, p. 751-783.
- Venditti, J. G., 2003, *Initiation and development of sand dunes in river channels*[Dissertation]: University of British Columbia.
- Venditti, J. G., and Bennett, S. J., 2000, Spectral analysis of turbulent flow and suspended sediment transport over fixed dunes: *Journal of Geophysical Research: Oceans*, v. 105, no. C9, p. 22035-22047.
- Venditti, J. G., Church, M., and Bennett, S. J., 2005, On the transition between 2D and 3D dunes: *Sedimentology*, v. 52, no. 6, p. 1343-1359.

- Wei, T., Willmarth, W. W., and ENGINEERING., M. U. A. A. D. O. A., 1983, Static Pressure Distribution on Long Cylinders as Function of Angle of Yaw and Reynolds Number, Defense Technical Information Center.
- Werner, B., 1995, Eolian dunes: computer simulations and attractor interpretation: *Geology*, v. 23, no. 12, p. 1107-1110.
- Werner, B. T., 2003, Modeling Landforms as Self-Organized, Hierarchical Dynamical Systems, *Prediction in geomorphology*, American Geophysical Union, p. 133-150.
- Werner, B. T., and Kocurek, G., 1997, Bed-form dynamics: Does the tail wag the dog?: *Geology*, v. 25, no. 9, p. 771-774.
- , 1999, Bedform spacing from defect dynamics: *Geology*, v. 27, no. 8, p. 727-730.

Vita

Travis Eric Swanson was born in central Texas. After graduating from high school in San Antonio he attended UT Austin and earned a bachelor of science in geology in August of 2007. His interest in hydrogeology was sparked and he returned for a master of science in geology. Upon graduating in 2010, he continued studies at UT Austin toward a PhD in geology. This dissertation is the result of the past five years of curiosity, imagination and scientific inquiry.

Permanent email: travis.swanson@utexas.edu

This dissertation was typed by Travis Eric Swanson.